ADVANCING IMAGING TECHNIQUES FOR ASSESSING PULMONARY MUCUS MACROSTRUCTURE AND MICROSTRUCTURE

Kelsey Jane Oeler

A dissertation submitted to the faculty at the University of North Carolina at Chapel Hill / North Carolina State University in partial fulfillment of the requirements for the degree of Doctor of Philosophy in the Department of Biomedical Engineering in the School of Medicine.

Chapel Hill
2023

Approved by:

Amy L. Oldenburg

David B. Hill

Richard L. Blackmon

Joseph Tracy

Kennita Johnson

ABSTRACT

Kelsey Jane Oeler: Advancing Imaging Techniques for Assessing Pulmonary Mucus Macrostructure and Microstructure
(Under the direction of Amy L. Oldenburg)

In pulmonary diseases, such as cystic fibrosis and chronic obstructive pulmonary disorder, we observe changes in pulmonary mucus behavior. However, our current understanding of how mucus properties may relate to the observed breakdown of the mucociliary clearance (MCC) system in diseased states is limited, both in terms of macroscopic mechanical properties and microscopic structure. Existing imaging techniques for assessing the viscoelasticity by directly measuring cilia-driven fluid flow in mucus samples lack controlled strain application, hindering their effectiveness. Also, commonly used techniques for sensing biomaterial nanostructure often require sample dehydrating or staining, which restricts their applicability. Optical coherence tomography (OCT) offers distinct advantages in performing depth-resolved tracking of fluid flow and dynamic light scattering of nanoparticles diffusing within the meshes of biomaterials which hinder their diffusion. The increased depth penetration and capability to assess small samples make OCT particularly advantageous.

In this dissertation, we present work aimed at observing mucus flow under physiologically relevant strains and simultaneously quantifying shear-induced anisotropy of mucus meshwork. First, we developed a micro-parallel plate strain induction chamber combined with OCT which was applied to track Newtonian fluid motion and mucus under physiologically relevant shear. Then, using polarization-sensitive OCT, we quantified translational (D_T) and rotational (D_R) diffusion coefficients of plasmonic gold nanorods as diffusive probes introduced into in polyethylene oxide solutions, hyaluronic acid solutions, agarose gels, and bronchial mucus. For all samples, D_T and D_R monotonically decrease with increasing solids concentration, which is attributed to increasingly constrained diffusion by the meshwork. Importantly, D_R

exhibits higher sensitivity and lower intra-sample variability than in D_T dehydrated mucus, which is particularly amenable to studying disease-like mucus. D_T and D_R measurements of gold nanorods in hypertonic saline-treated human bronchial epithelial cell cultures revealed cilia-induced dynamic mixing effects and the presence of hard-packed mucus. Lastly, diffusion tensor OCT (DT-OCT) hardware is designed to rapidly query angle-dependent D_T and D_R and is assessed in isotropic agarose and collagen gel samples. Overall, these experiments enhance our understanding of biofluid flow and nanostructure in mucus under physiologically relevant conditions, shedding light on mucus properties and their significance in respiratory health and therapy.

ACKNOWLEDGEMENTS

First and foremost, I would like to thank Dr. Amy Oldenburg for the opportunity to pursue a Ph.D. in her lab and for providing me with valuable discussions, resources, and mentorship over the past six years. I thank my committee members David Hill, Richard Blackmon, Kennita Johnson, and Joseph Tracy for providing valuable resources and support towards the completion of my Ph.D. I would also like to thank my past and present group members. Thank you, Lin Yang, for your mentorship, guidance, and willingness to share, teach, and work closely with me over the years. Thank you to Jessie Barrick, Ben Levy, and Ruofei Bu for always being available for questions and support, especially during the early years. Thank you, Taylor Robinson, for bringing your excitement to every task, and for being a fantastic soundboard for bouncing ideas. I would like to thank Pan Ji, Hillel Price, Santosh Balakrishnan, Yinghan Xu, and Srikamal Soundararajan for making our work environment a supportive one.

I deeply thank my mother and father, Jane and Dieter Oeler, for their endless support and love over the many years of my academic journey. Thank you for supporting and encouraging my love for learning and puzzles and for instilling a drive for knowledge from an early age. This all would not have been possible without you. I would also like to thank my Aunt Pam and Uncle Bob for their amazing support, giving me ample opportunity to come recharge with family, always being up to discussing my projects, and for reminding me there is nothing a good walk can't fix.

My years of learning and growing were encouraged by many professors and teachers over the years. Thank you Dr. Bjorg Larson for introducing me to the world of biomedical optics as an undergraduate and for providing me with years of mentorship. Thank you Dr. Supple and Dr. Murawski for believing in me when I said I wanted to pursue a Ph.D. I would also like to thank my high school teachers for inspirating

me: I'd like to thank Jon Stelman for sharing his love of physics and encouraging my own and Mr. Streicher for his devotion to seeing his students succeed and for always being in my corner.

Last but not least, I would like to thank the people without whom I would have lost my sanity over these many years. Thank you to my friends for bringing me endless laughter, joy, and motivation. To Emily Kubin, I am so beyond thankful for your friendship. You have been my rock these past eight years and I would not be here without you. We did it! To Emily Fawcett (Simpson), thank you for always bringing me into a fit of laughter, listening to all my rants, and for letting me live with you during the final months. To Morgan Clark, Michele Kelley, Ramses Gonzalez, and Zack Hall: I love you all. I am incredibly lucky to have met such pure and true friends through this program and there are not enough words in the world to express my gratitude for each of you. To my partner Sean Sabol, thank you for your kindness, patience, and support throughout the tail end of this process, and for always knowing how to bring a smile to my face every day.

I would like to express my final heartfelt gratitude to all those who unwaveringly maintained their confidence in me. Thank you.

TABLE OF CONTENTS

LIST OF FIGURES

LIST OF TABLES

LIST OF ABBREVIATIONS

AG	Agarose
ALI	Air-liquid interface
CA	Clear aperture
CAD	Computer aided design
CF	Cystic fibrosis
CFTR	Cystic fibrosis transmembrane conductance regulator
CI	Confidence interval
COPD	Chronic obstructive pulmonary disorder
DLS	Dynamic light scattering
DPBS	Diluted phosphate buffered saline
DR	Rotational diffusion
DS-OCT	Diffusion sensitive optical coherence tomography
DT	Translational diffusion
ECM	Extracellular matrix
EFL	Effective focal length
GNP	Gold nanoparticle
GNR	Gold nanorod
HA	Hyaluronic Acid
hBE	Human bronchial epithelial
hBEC	Human bronchial epithelial cell
HTS	Hypertonic saline
LAOS	Large amplitude oscillation shears
LF-OCT	Line field optical coherence tomography

LoA	Limits of Agreement
LSPR	Longitudinal surface plasmon resonance
MCC	Mucociliary clearance
MPPSIC	Microparallel plate strain induction chamber
NA	Numerical aperture
NIR	Near infrared
OCT	Optical coherence tomography
PCL	Periciliary layer
PIV	Particle imaging velocimetry
PEG	Polyethylene glycol
PEO	Polyethylene oxide
PS-OCT	Polarization sensitive optical coherence tomography
ROI	Region of Interest
SAOS	Short amplitude oscillation shears
SEM	Scanning electron microscopy
SPR	Surface plasmon resonance
TEM	Transmission electron microscopy

CHAPTER ONE
INTRODUCTION

Pulmonary mucus is a functional component of the respiratory system's main defense mechanism against infections. Respiratory diseases can alter the mucus' viscoelastic and barrier properties of the biopolymeric meshwork. Understanding the mechanical and structural properties in both hydrated and dehydrated mucus is essential for monitoring treatment and informing drug delivery designs. However, there are limited imaging techniques for assessing the properties of pulmonary mucus, most of which are destructive to the sample or require large sample volumes. To address these limitations, we use optical coherence tomography (OCT) to investigate the properties of mucus. In this dissertation, work will be presented towards the goal of developing new OCT techniques and advancing current ones for investigating pulmonary mucus macrostructure and microstructure.

1.1 The mucociliary clearance system and pulmonary disease

Pulmonary mucus plays a vital role in maintaining a healthy respiratory system. The primary function of pulmonary mucus is to entrap inhaled pathogens to protect the respiratory system against infections. A protective airway surface layer of secreted mucus is comprised of 0.3 % mucin polymers, 0.8% globular proteins, 0.9% salts, and 98% water [1]. The muco-ciliary clearance (MCC) system is the airway's main defense mechanism [2]. While multiple types of cells and glands make up the upper airways, the MCC is comprised of three main components: ciliated epithelial cells, the periciliary layer (PCL), and mucus layer. The epithelial cell's cilia are hair like appendages that utilize a beating motion to transport mucus along the respiratory track. The periciliary layer was classically believed to be made mostly of water, however more recent findings suggest the periciliary layer is a dense brush [3]. The mucus layer is mostly made of two major high molecular weight mucin polymers, MUC5B and MUC 5AC [4]. It resides on top of the periciliary layer and has an air-liquid surface interface. Inhaled pathogens are trapped by mucus and

are expelled by the cilia to prevent infection in the respiratory system. However, the MCC can only efficiently propel mucus if there is a proper osmotic balance between the mucin layer and PCL. In a healthy respiratory system the osmotic pressure in the mucus layer is ~100Pa and in the PCL is ~500 Pa [1]. In pulmonary diseases, the osmotic pressure of PCL is greater than or equal to the osmotic pressure in the mucus layer [5]. This leads to mucus dehydration, altering the viscoelastic properties of mucus and changing the way a biofluid moves, which potentially exacerbates the effects of the disease [5, 6]. The movement of mucus depends on the strain induced by cilia and the rheological response of the fluid is largely dictated by its polymeric mucin meshwork [7, 8]. The breakdown of disease-state MCC causes accumulation of an increasingly hyperviscous mucus layer which weighs down the cilia and further hinders MCC in a vicious cycle [10, 11].

Small changes to mucus concentration can greatly change them mechanical and transport properties of mucus [3, 6]. Pulmonary diseases such as cystic fibrosis (CF) and chronic obstructive pulmonary disease (COPD) are characterized by dehydrated mucus that cilia are unable to propel out of the respiratory system, leaving individuals susceptible to infection. Cystic fibrosis is an autosomal recessive disease that affects approximately 105,000 children and adults globally [13]. It can affect the respiratory system, digestive system, and the reproductive system of an individual.CF is caused by a mutation of the cystic fibrosis transmembrane conductance regulator (CFTR) gene [14]. The mutation causes the CTFR protein, which is partially responsible for maintaining a proper osmotic balance via chloride secretion, to be dysfunctional. Individuals living with CF are more likely to develop infections in both the upper and lower respiratory tract, which can lead to chronic coughing.

In 2018, COPD was the fourth leading cause of death in the United States [15]. COPD is a progressive disease that is mainly characterized by airflow obstruction due to chronic inflammation of the lungs. There is currently no cure for COPD, however common treatments included the use of bronchodilators, inhaled steroids, and oxygen therapy. The term COPD encompasses two major subset conditions called emphysema and chronic bronchitis [16]. Emphysema develops when there is damage to the alveoli that reduces the surface area of the lungs, limiting the amount of oxygen that can reach the

bloodstream. Chronic bronchitis is characterized by chronic inflammation of the bronchial tubes during which chronic hyperconcentration of mucus can occur. This results in a chronic cough and heavy production of phlegm.

1.2 Pulmonary mucus macro- and micro- structure assessments

There have been many advances towards visualizing and quantifying mucus macrostructure and microstructure with imaging modalities such as scanning electron microscopy [3, 16 – 22] and optical coherence tomography. OCT is emerging as a modality particularly amenable to characterizing fluid flow, cellular structure on the epithelium, and rheological properties because it offers high-speed, depth-resolved imaging with microscopic resolution [16, 17]. Oldenburg et al. [24] used OCT to investigate mucus flow, ciliary beat frequency, and the microanatomy of the PCL in both an *in vitro* human airway model and *ex* vivo mouse model. Micro-OCT (μOCT), with a lateral resolution of 2 μm and axial resolution of 1 μm, has recently been utilized to assess the macrostructure of the MCC. Using a custom μOCT system, Liu et al. [25] investigated the cilia beat frequency and ciliary stroke pattern. Birket et al. [26] furthered used the same μOCT system to investigate the functional microanatomy of human bronchial epithelial cultures and compared it to the microanatomy of swine tissue cultures that were afflicted with CFTR dysfunction. Their results established a relationship between the hydration of the PCL and the rate of mucus transportation. Furthermore, Chu et al. [27] extended the μOCT system to be a fiber-optic endoscopic instrument for *in vivo* imaging of the trachea to assess the functional airway microanatomy. Particle tracking velocimetry (PTV) can be a useful tool for quantifying fluid velocity in small volumes and there have been promising results employing OCT for PIV-based studies. For example, Buchsbaum et al. [28] employed PIV on a glass-fibre polymer compound to assess the fluid behavior of the polymer melt, while Jonas at el. seeded *Xenopus tropicalis* cultures with tracer microparticles to visualize cilia-driven flow profiles.

Past these investigations, questions still remain on how mucus transport is affected by the viscoelastic properties of mucus. Although mucus is known to be shear thinning, we do not have a clear answer for under what specific conditions (in terms of beat frequency, mucus thickness and concentration) there is an onset of shear thinning. On a microstructure scale, when it comes to treatment options for

respiratory diseases, the barrier properties of the biopolymeric meshwork of mucus informs the design of drug delivery systems for the lung epithelium [8, 12, 13]. The barrier properties of the meshwork relates to the permeability of inhaled drugs. To counteract the dehydrated mucus' impairment of the MCC, mucus-thinning therapies, such as aerosolized hypertonic saline (HTS), are commonly administered [14, 15]. While HTS is a low-cost and easily administered treatment [15, 16], its effectiveness in improving MCC remains uncertain due to patient-to-patient variability and conflicting therapeutic outcomes [15, 17, 18]. The question remains how increase in mucus solids concentration, (wt%) as it becomes severely dehydrated during pulmonary disease (> 3 wt%), is directly associated with decrease in nanopore size within the mucus macromolecular meshwork. Additionally, towards the goal of informing drug delivery design, it would be useful to understand how the nanostructure pore anisotropy is altered during mucus transport and its dependence on concentration.

1.3 Basics of Spectral Domain Optical Coherence Tomography

Optical coherence tomography is a low coherence imaging technique that is analogous to ultrasound. Like ultrasound, OCT is an advantageous imaging technique due to its depth-dependent imaging capabilities and non-destructive nature. In contrast to ultrasound, OCT utilizes the time-delay of optical signals instead of acoustic signals to capture cross-sectional images beneath tissue, allowing for micro-meter axial resolutions. Optical coherence tomography uses interferometry, a technique that splits light into two paths to later recombine and constructively or destructively interfere. How light will interfere depends on the optical path delay (OPD) between the two paths [13, 14]. For the interference signal to store information, the optical path delay must be within the coherence length (l_c) of the light source, such that $\mathrm{OPD} \leq l_c$. The coherence length depends on the light source's center wavelength, λ_0, and the power spectrum's full width half maximum (FWHM), $\Delta\lambda$, according to:

$$l_c = \frac{\lambda_0^2}{\pi\Delta\lambda} \tag{3.1}$$

From the coherence length dependence on FWHM, it is clear the light source must be broadband.

The earliest OCT systems were time domain (TD-OCT), in which a reference arm must be mechanically moved for imaging, greatly limiting the image collection speed. To improve imaging speeds, OCT systems were developed to perform measurements in the Fourier domain, appropriately named Fourier domain OCT (FD-OCT). FD-OCT does not require movement of the reference arm making it faster than TD-OCT imaging. There are two very common variations of FD-OCT: swept source OCT (SS-OCT) and spectral domain OCT (SD-OCT). In this dissertation, we will use the latter. Spectral domain OCT (SD-OCT) systems use a Michelson interferometer comprised of a 50:50 beam splitter that splits the light towards a sample arm and a reference arm, which is comprised of a fixed position mirror (Figure 1.1). The refractive index distribution of a biological sample will cause light to be backscattered from the sample. As stated above, the light from the two arms will interfere and an interference signal will be dispersed spatially by a spectrometer and collected by a line scan camera. A reflectivity profile is encoded on the interference signal if the OPD is an appropriate length.

We can then obtain the reflectivity profile by performing a Fourier transformation of the interference spectrum. The aim of OCT is to produce a structural image that is a reconstruction of the reflectivity profile as a function of depth. An A-Line is defined as a one-dimensional reconstruction. By transversely scanning the surface of a sample we can acquire consecutive A-Lines. These spatially consecutive A-Lines can be constructed together into a two-dimensional, where dimensions are depth and lateral scan distance, image called a B-Mode image. If no scanning occurs (such that we image the same spatial location over time) the two-dimensional reconstruction, where dimensions are depth and time, of A-Lines is called an M-Mode image.

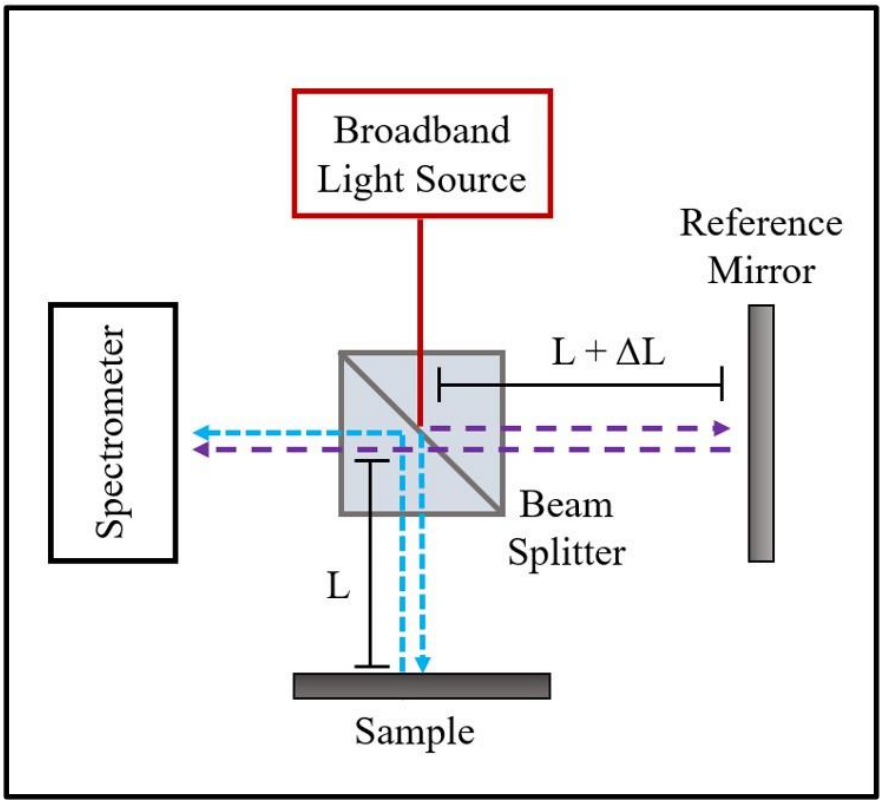

Figure 1.1: Schematic diagram of SD-OCT comprised of a broadband light source, a Michelson interferometer, and a spectrometer. An optical path delay between the reference arm and the sample arm is shown by labeling length L in the sample arm and length $L + \Delta L$ in the reference arm

1.4 Outline of the Dissertation

This Ph.D. dissertation is organized as follows: Each chapter begins with a detailed motivation for investigating a specific aspect related to the research topic. Chapter 2 focuses on the investigation of biopolymer bulk flow and includes the introduction of the hardware design for an OCT-amenable micro-parallel plate strain induction chamber (MPPSIC) and the development of a custom particle tracking velocimetry MATLAB code for analysis. The MPPSIC is utilized to induce shear on Newtonian fluids for validating the design and custom analysis code. Additionally, it is used to explore the bulk flow response of pulmonary mucus to physiologically relevant shear rates.

In Chapter 3, the research shifts to the investigation of the use of gold nanorods (GNRs) and their translational and rotational diffusion dependence on concentration for studying the nanotopology of biopolymers. This chapter presents GNR diffusion experiments conducted across a wide range of sample concentrations, including hyaluronic acid, agarose gels, polyethylene oxide solutions, and human Bronchial

Epithelial (hBE) mucus. The results of the hBE mucus experiments are used to map translational and rotational diffusion rates to concentration, which is used to develop a pulmonary mucus hydration assay. This mapping is then applied to available data from a hypertonic saline (HTS) treated hBEC air-liquid interface (ALI) culture dataset to demonstrate the usefulness of this assay.

Chapter 4 is dedicated to the hardware design and validation of the Diffusion Tensor OCT (DT-OCT) system for investigating the anisotropy of biopolymer pores. A novel sample arm design is introduced, which incorporates an automated compact periscope to redirect the beam path to the outer edge of the focal lens. This chapter provides a detailed description of the compact periscope design, its implementation into the hardware, and the measures taken to mitigate the elliptical polarization-producing effects of the two silver rotating mirrors. The hardware validation includes the measurement of diffusion in two separate isotropic samples, agarose gels and collagen gels, revealing a dependence of the diffusion coefficient on sample concentration. Chapter 5 serves as a comprehensive conclusion, summarizing the research conducted in this dissertation.

CHAPTER TWO

OCT PARTICLE TRACKING VELOCIMETRY OF BIOFLUIDS IN A MICROPARALLEL PLATE STRAIN INDUCTION CHAMBER

In this chapter, we propose a new platform for visualizing biofluid motion under physiologic shear with OCT, which is capable of tracking microscale fluid motions over millimeter fields of view, in combination with a micro-parallel plate strain induction chamber (MPPSIC) amenable to real-time OCT imaging. By designing a strain induction chamber amenable to OCT imaging, for the first time, we demonstrate depth-resolved visualization of fluid motion induced by controlled, dynamic shearing. Our hardware design and custom particle tracking velocimetry code are first validated using Newtonian fluids comprised of glycerol-water mixtures at low Reynolds numbers such that the observed motion has a simple theoretical analytical solution for validation. We then demonstrate the MPPSIC with a bronchial mucus sample at 1.5 wt%, a concentration consistent with a healthy airway epithelium. Our demonstrations show that the MPPSIC can successfully track biofluid flow in conditions that recapitulate the airway surface liquid on the lung epithelium.

2.1 Why study pulmonary mucus response to shear?

For a proper understanding of how disease states modify biofluid flow, it is necessary to quantify fluid flow *in situ* under physiological conditions over a wide field-of-view, allowing one to characterize the system over its full span (such as the thickness of the airway surface layer) and to detect heterogeneity in the fluid flow arising from intrinsic viscoelastic heterogeneity or from heterogeneous applied strain. However, the ability to investigate fluid flow under these conditions is technically challenging. There is no current protocol for experiments that clearly defines at what cilia beat frequency, mucus layer height, and mucus concentration we can see the onset of heterogeneity in fluid flow. It would be ideal to assess the effects of multiple different parameter combinations while minimizing sample volume required for the

multiple iterations. Here, we present a suitable approach using OCT to track particle probes in a controlled MCC-mimicking environment, giving way for investigative studies over a wide range of strain rates with sub-milliliter sample volumes.

2.2 Parallel Plate Fluid Flow Models

To validate the MPPSIC we first write the analytical solutions for the depth-dependent fluid velocity under the conditions used in our experiments. Our validation experiments are performed with Newtonian fluids between parallel plates, while the bottom plate is displaced laterally with a periodic waveform, either triangular (to impart constant shear rate) or sinusoidal (to impart an oscillatory shear rate). In all experiments, the plates were measured to have an angle difference less than 1° (Appendix B), thus we treat them as parallel here. Using OCT, we quantify the velocity of polystyrene microspheres added to the fluids for particle tracking. The microspheres are presumed to have no-slip and negligible Brownian motion such that their motion represents that of the surrounding fluid. The plates are much wider than the OCT lateral field of view so that we can neglect edge effects, and the bottom plate is driven along the x axis, so that we may assume that fluid velocity is purely along the x axis, $V=V_x$, and only depends on the depth from the top plate, z, and time, t. The fluid is assumed to follow a no-slip condition with both plates, and the plate separation is given as H. When the velocity of fluid flow is not constant over time, it is referred to as transient flow, and its behavior is influenced by the kinematic viscosity (v). The transient time of the Newtonian fluids used in our experiments were calculated to be negligible at less than 1 ms [38]. The Reynolds numbers of the Newtonian fluids were considered low at a maximum value of 1.3×10^{-4}.

For experiments employing a constant shear rate, a triangle waveform drives the bottom plate of the MPPSIC at a constant velocity, $\pm V_{x_0}$ in upswing and downswing, respectively; for simplicity we treat each direction of motion equally and ignore the sign of the velocity. This situation is equivalent to Navier-Stokes' first problem for a finite depth field, in which a Newtonian fluid is induced with a constant shear rate at one boundary. The steady-state solution when the Reynolds condition is low exhibits a constant velocity gradient in depth, such that [39]:

$$V_x = V_x(z) = \frac{V_{x_0} z}{H}. \tag{1.2}$$

In the steady state, the fluid velocity will decrease with direct proportionality to the distance from the plate moving at velocity V_{x_0}. In this case, fluid velocity can be tracked at various known depths and the shear rate, $\dot{\gamma}$, is constant and given by the velocity gradient:

$$\dot{\gamma} = \frac{dV_x(z)}{dz} = \frac{V_{x_0}}{H}. \tag{1.3}$$

To mimic physiological conditions of the MCC more closely we then performed experiments under sinusoidal shear by driving the bottom plate with a sinusoidal waveform of angular frequency ω and velocity amplitude U_{x_0}. For a Newtonian fluid, the solution of the Navier-Stokes' second problem for a finite depth field holds for sinusoidal conditions in the steady state. In this solution, a fluid induced with a sinusoidal shear with under low Reynolds conditions will again exhibit a velocity gradient constant in depth and follow the time-dependence of the driving waveform, such that [39]:

$$U_x = \frac{U_{x_0} z}{H} \cos(\omega t + \phi) = U_{x_{\max}}(z) \cos(\omega t + \phi) \tag{1.4}$$

and the phase, denoted as ϕ, is equal to that of the driving waveform (no phase lag under low Reynolds conditions). In this solution, the fluid velocity amplitude $U_{x_{\max}}(z)$ has the same form as the constant velocity vs. depth in Eq. 2.1, which decreases with direct proportionality to the distance from the plate. By tracking $U_{x_{\max}}(z)$ at various known depths, the maximum shear rate (equivalent to the shear rate amplitude) in time is constant in depth, and is extracted by the gradient of the velocity amplitude:

$$\dot{\gamma}_{\max} = \frac{dU_{x_{\max}}(z)}{dz} = \frac{U_{x_0}}{H}. \tag{1.5}$$

2.3 Materials and Methods

2.3.1 Microparallel Plate Strain Induction Chamber

To create the microparallel plate strain induction chamber (MPPSIC), we updated a previous design of a micro-parallel plate rheometer amenable to confocal microscopy imaging [40]. The MPPSIC consists of two removable and parallel flat plates, one of which remains stationary while the other is driven laterally with a desired waveform. To make this design amenable to OCT, the top plate is comprised of optical quality 1 mm thick microscope glass, and the upward facing surface of the bottom plate is coated with a light-absorbing paint to avoid specular reflection. A three-axis nano-positioner (LP100 Mad City Labs, Inc.) is employed to control the bottom plate lateral oscillations and to set the distance of separation between plates. The top plate is stabilized by a cage system, uncoupled to the nano-positioner, which allows for tilt of the full strain induction chamber to reduce specular reflection from the top plate (Figure 2.1).

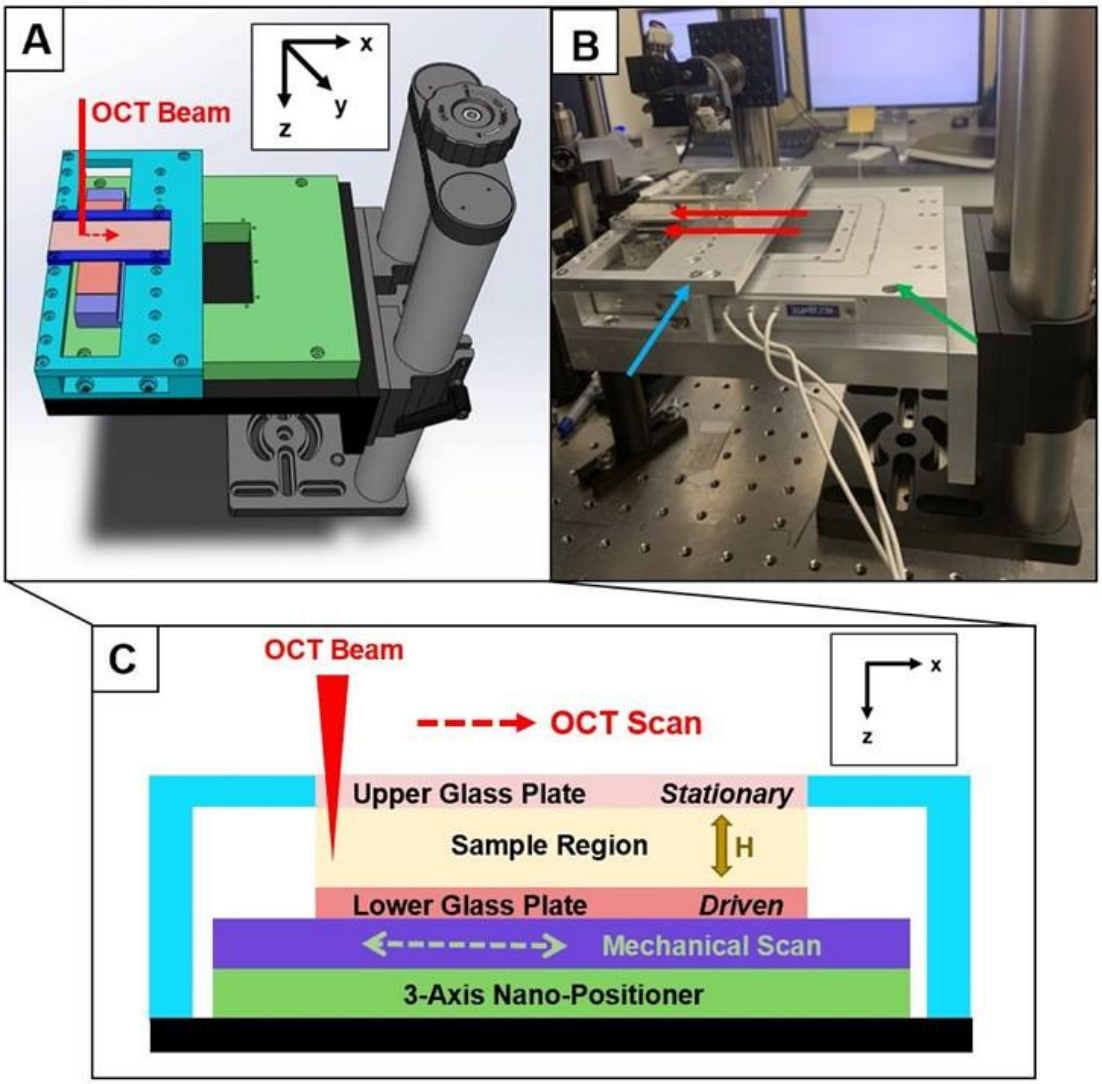

Figure 2.1: (a) Solidworks CAD (computer aided design) of MPPSIC on a large axial translational stage. The cage system (blue) holds the top plate stationary relative to the stage without coupling to the nano-positioner. The incoming OCT beam and scan path are indicated in red. (b) Photograph of the MPPSIC stage under the OCT sample arm. The red arrows point to the glass plates, the blue arrow points to the stationary cage system, and the green arrow points to the 3-axis nano-positioner. (c) Diagram of an *x*-*z* cross-section within the MPPSIC. The yellow arrow indicates plate separation distance, H, controlled through an external power supply. The mechanical scan and OCT scan are along the *x* axis as shown.

The MPPSIC is designed to induce shear on liquid samples deposited between the plates. A waveform generator produces either a triangle waveform to drive the bottom plate at a constant velocity or a sinusoidal waveform to drive the bottom plate with sinusoidal velocity. The OCT data acquisition system synchronizes the start of OCT image acquisition with the start of the MPPSIC waveform, with a measured 9 ms mechanical delay accounted for in image processing. The nano-driver can induce lateral displacements

up to 100 μm, and for waveforms driven at up to 10 Hz, this allows us to induce maximum shear rate amplitudes of 6 – 39 s^{-1} on the sample while controlling the plate separations between 80 – 500 μm.

Importantly, this design can mimic the shear strain and strain rate applied to mucus by cilia at the bronchial epithelium. Mucus layer thickness is typically 20 – 100 μm and the average length of cilia is between 9 – 12 μm with beat frequencies between 10 – 20 Hz. As such, it is estimated that mucus undergoes 1 – 10 s^{-1} shear strain rates at bulk flow speeds of 60 – 100 μm/s [4]. Mucociliary clearance velocities are well described by oscillations about constant velocities. Since the oscillations alone contribute to the strain within the fluid, we choose to drive our system with a sinusoidal waveform for mucus samples to mimic the shear strains and strain rates associated with MCC [41].

2.3.2 Sample Preparation

For experiments on Newtonian fluids, three aqueous glycerol (Sigma Aldrich 99% pure glycerol) solutions were prepared (two for triangle, and one for sinusoidal actuation) with 2.07 μm diameter polystyrene microspheres (Bangs Laboratories, IN) added as tracer particles. Desired volumes of water, glycerol, and microspheres solutions were calculated to target samples with a dynamic viscosity of ~400 mPa·s using equations found in Ref. [42] and final microsphere density of 1 – 3% solids by volume. Each pipetted volume was weighed to determine the actual ratio of water to glycerol to calculate each sample's dynamic viscosity, which were all between 294 – 462 mPa·s. The refractive indices of the aqueous glycerol solutions, needed for calibration of depth in the OCT images collected at 800 nm wavelength, were calculated with the Arago-Biot formula [43] as the summation of the weight fractions of water and glycerol multiplied by their respective refractive indices, 1.340 for water and 1.465 for glycerol [44]. Sample refractive indices ranged between 1.45 – 1.46. For experiments in mucus, which is non-Newtonian, mucus is harvested from human bronchial epithelium cell cultures (provided by the Cystic Fibrosis/Pulmonary Research Treatment Center at the University of North Carolina at Chapel Hill) and prepared to a defined concentration following established protocols [45]. These samples were diluted with 1XDPBS (Distilled Phosphate Buffered Saline) and microspheres were added such that the final concentration of mucus was

1.5 wt% solids, with microsphere solids making up 1 – 3% of the sample's total volume. Mucus samples were assumed to have a refractive index of 1.34, the same as that of water.

2.3.3 MPPSIC Constant Velocity Newtonian Sample Procedure

To test the functionality of the MPPSIC, we began with constant velocity experiments via triangular waveforms. Samples were loaded into the MPPSIC and the plate separation set to ~300 μm. The MPPSIC was driven in the lateral direction (x) with a triangle waveform where the speeds of the forward and backward sweeps were equal. Experiments were performed on two separate samples: sample 1 with viscosity of 462 mPa·s, and sample 2 with a viscosity of 294 mPa·s. Each sample was driven at 0.5 Hz with bottom plate speeds from 5 – 60 μm/s in increments of 5 μm/s. This range of experimental conditions corresponds to peak-to-peak shear strains between 1.7 – 20% and shear rates between 0.017 – 0.20 s^{-1}. OCT imaging was triggered at the beginning of MPPSIC oscillations, where B-mode images (1.5 mm × 1.5 mm in $x \times z$ in the sample) comprised of 250 A-lines were collected sequentially at a line rate of 10 kHz with 2 ms of dead time between frames, the frame rate was 37 Hz. A total of 3 waveform cycles were collected in each experiment.

2.3.4 MPPSIC Sinusoidal Velocity Newtonian Sample Procedure

To test the MPPSIC with a waveform that more closely recapitulates the shear dynamics of bronchial mucus, we performed experiments where the shear was sinusoidally varying. A Newtonian fluid sample of 347 mPa·s was loaded into the MPPSIC and the plate separation set to ~150 μm. The MPPSIC was driven in the lateral direction (x) with a sinusoidal waveform, and data was collected at driving frequencies in increments of 1 Hz from 1 – 10 Hz with a maximum bottom plate peak-to-peak displacement of 24 μm, resulting in peak speeds from 75 – 750 μm/s and shear rate amplitudes between 0.5 – 5.0 s^{-1}. OCT imaging was triggered at the beginning of MPPSIC oscillations, where B-mode images (1.2 mm × 1.5 mm in $x \times z$ in the sample) comprised of 208 A-lines were collected sequentially at a line rate of 69 kHz; with 2 ms of dead time between frames, the frame rate was 199 Hz. A total of 6 waveform cycles were collected in each experiment.

2.3.5 MPPSIC Sinusoidal Velocity Mucus Sample Procedure

To observe motion tracking capabilities in mucus, experiments were performed on a bronchial mucus sample. Mucus prepared as above was loaded into the MPPSIC and the plate separation set to ~240 μm. The MPPSIC was driven in the lateral direction (x) with a sinusoidal waveform. Eight experiments were performed on the sample using driving frequencies in increments of 1 Hz from 3 – 10 Hz. Each sample was driven with a maximum bottom plate peak-to-peak displacement of 18 μm and then repeated at 24 μm, resulting in peak speeds from 170 – 750 μm/s and shear rate amplitudes between 0.7 – 3.2 s^{-1}. OCT imaging was triggered at the beginning of MPPSIC oscillations, where B-mode images (1.2 mm × 1.5 mm in $x \times z$) comprised of 208 A-lines were collected sequentially at a line rate of 69 kHz; with 2 ms of dead time between frames, the frame rate was 199 Hz. A total of 6 waveform cycles were collected in each experiment.

2.4 Image Analysis

After collecting OCT images of fluids within the MPPSIC, the goal is to accurately extract the microsphere displacements (and corresponding velocities) in depth and time, for subsequent comparison against existing models of fluid dynamics. A flow chart of the image analysis procedure to extract $V_x(z,t)$ using a normalized cross-correlation method is shown in Fig. 2.2.

2.4.1 Region of Interest (ROI) Selection

The frames corresponding to the first 30 ms are discarded to avoid tracking transient motions induced by the system as well as the MPPSIC's mechanical lag. To mitigate digitization noise, all images are upsampled in the lateral direction (x) by a factor of 4. Then, the tilt of the plates from horizontal, which is necessary in OCT to avoid strong specular reflections that saturate the detection hardware, is corrected by a semi-automated method. The top plate's angle is used to vertically shift each column of the image to form a horizontal surface, and the difference between the top and bottom plate's angle is checked to ensure that the plates are parallel within 1°. Throughout the image analysis procedure, OCT pixel sizes calibrated in free-space are multiplied by an axial distortion factor, $D_{axial} = \frac{\sqrt{n^2 - \sin^2(\alpha)}}{n^2}$, and transverse distortion

factor, $D_{transverse} = \frac{1}{\cos(\alpha)}$, to account for the effects of the sample refractive index, *n*, determined as above, and tilt angle, α. After this correction, the separation distance *H* between the top and bottom surfaces is measured at the center of the image.

The sample region is divided into a grid of ROIs of $i = 1{:}N$ rows by $j = 1{:}M$ columns for each frame $k = 1{:}Q$, denoted as $\mathrm{ROI}(k)_{i,j}$. ROI dimensions were chosen to provide sufficient resolution in the axial direction (15 – 18 μm) for shear analysis, while extending further in the lateral (*x*) direction (150 μm) to capture ~1 – 4 microspheres per ROI to facilitate cross correlation measurements. ROIs were 12×100 or 18×100 pixels, corresponding to 25 × 150 μm and 38 × 150 μm, respectively, for experiments with large (> 200 μm) or small (< 200 μm) plate separations, respectively.

Displacements are obtained within each non-empty ROI by normalized cross-correlation, with the determination of non-empty being based on an average intensity threshold. Correlation coefficients are computed between pairs of thresholded ROIs within the time series, $I_1(x,z) = \mathrm{ROI}(k_1)_{i,j}$ and $I_2(x,z) = \mathrm{ROI}(k_2)_{i,j}$, according to:

$$\rho(u,v) = \frac{\sum_{x,z}[I_1(x,z) - \overline{I_1}][I_2(x-u,z-v) - \overline{I_2}]}{\left\{\sum_{x,z}\left[I_1(x,z) - \overline{I_1}\right]^2 \sum_{x,z}\left[I_2(x,z) - \overline{I_2}\right]^2\right\}^{\left(\frac{1}{2}\right)}} \tag{1.6}$$

where I_2 (and hence the range of (u,v) computed) is extended by the theoretical lateral (in *x*) and axial maximum displacement of a particle. The (u,v) corresponding to the maximum correlation ρ is taken as the lateral and axial particle displacement (x_{shift}, z_{shift}), respectively. The z_{shift} values were found to be consistently close to zero pixels and were considered negligible.

2.4.2 Constant Velocity Image Analysis

For constant velocity experiments, a triangle waveform drives the bottom plate. To avoid transient effects in the stage or fluid at the turnaround points of the waveform, we omit ("pad") all OCT images within two frames of the waveform peaks and valleys. As depicted in Fig. 2.2, each half-cycle of the

waveform is analyzed by computing displacements between pairs of frames. Pairs were chosen by employing a depth-dependent frame decimation value, Δk_i, based upon an initial estimate of the velocity within that row. Details of the decimation technique may be found in Appendix B. The purpose of the decimation is to exaggerate motion in regions of low velocity, such as near the top plate, where displacements between successive frames can be less than a single pixel. Initial velocities are estimated by linear extrapolation of the velocity obtained at the bottom, in $\mathrm{ROI}_{N,j}$, to the top plate where we expect a velocity of zero.

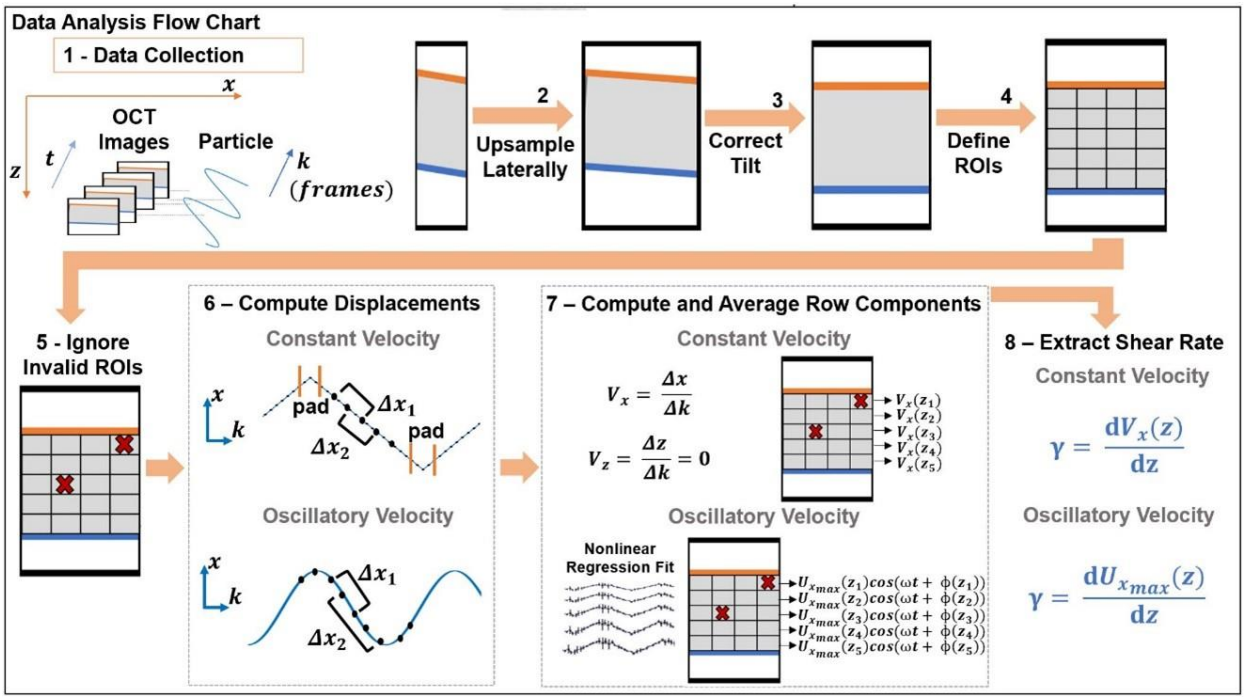

Figure 2.2: Image analysis flow chart. Step 1 is performed with LabView and all other steps were performed in Matlab 2019b. To omit ROIs that contain no particles to track, we employ two steps: intensity thresholding then a cluster check. A threshold is calculated for each row, *i*, of ROIs to account for system sensitivity roll-off. The threshold is the mean pixel intensity (averaged over *j*,*k*) plus 1.5× the standard deviation. Thresholded ROIs that contain more than one non-zero pixel are then tested to determine if the intensity is spatially clustered, suggesting the presence of a particle. This is performed by auto-correlating each thresholded ROI with a 1-pixel diagonal displacement and keeping only ROIs for which the result is non-zero. Each $\mathrm{ROI}_{i,j}$ must pass the cluster test across all frames (*k*) to be considered non-empty. Also, each row of ROIs must contain at least one non-empty ROI for the image stack to be considered valid for analysis.

Finally, lateral displacements, $x_{shift}(k)_{i,j}$ are computed within each sweep by cross-correlating $I_1 = \mathrm{ROI}(k)_{i,j}$ with $I_2 = \mathrm{ROI}(k+\Delta k)_{i,j}$ for $k = 1 \ldots F - \Delta k_i$ according to Eq. (2.5), where F is the number of frames in one sweep. We then compute the velocity, V_x, in pixels per frame, according to:

$$V_x(k)_{i,j} = \frac{x_{shift}(k)_{i,j}}{\Delta k_i} \tag{1.7}$$

In each $\mathrm{ROI}_{i,j}$, the velocity in each half-cycle q is computed by averaging $V_x(k)_{i,j}$ over all k, resulting in $V_x(q)_{i,j}$. The average and standard deviation of the speed in each row, i, is then computed from the absolute value (to account for forward and backward motion) of $V_x(q)_{i,j}$ over all j and q, providing $V_x(z) = V_{x_i} \pm \sigma_{V_{x_i}}$.

2.4.3 Sinusoidal Velocity Image Analysis

For sinusoidally varying velocity experiments the driving velocity is no longer constant, so the approach above is extended to account for variable frame decimation in time, $\Delta k(k)_i$. The details of the decimation technique may be found in Appendix B. The frame decimation value for each frame and depth, $\Delta k(k)_i$ is then used to define each pair of images, $I_1 = \mathrm{ROI}(k)_{i,j}$ and $I_2 = \mathrm{ROI}(k + \Delta k(k)_i)_{i,j}$, where k is now extended over all frames in the scan (unlike triangle data analyzed within each half-sweep). Analogous to Eq. (2.6), velocities $U_x\left(k + \frac{\Delta k(k)_i}{2}\right)_{i,j}$ are computed by dividing $x_{shift}(k)_{i,j}$ by $\Delta k(k)_i$; note that since the velocity is now varying in time, each velocity is assigned to a frame in the middle of the interval, located at $k + \frac{\Delta k(k)_i}{2}$. Finally, velocity in each row of ROIs is averaged, while preserving the time-dependence (k), to obtain an average velocity waveform at each depth:

$$U_x(k)_i = \frac{\sum_{j=1}^{M} U_x(k)_{i.j}}{M}, \tag{1.8}$$

and velocities are converted from units of pixels per frame to microns per second according to the distortion factors above.

To extract velocity amplitude, frequency, and phase, velocity waveforms were fit by nonlinear least-squares to a sinusoidal waveform. For rows with only one valid ROI, an unweighted fit was used; for rows with multiple valid ROIs, a weighted fit was used, where the standard deviations of the $U_x(k)_{i,j}$ were used as the weights.

2.5 Experimental Results

2.5.1 MPPSIC Constant Velocity Performance on Newtonian Fluid

In Figure 2.3(a), an example OCT B-Mode image frame shows the distribution of the microsphere tracer particles within a glycerol-water sample between the glass plates. To showcase the motion tracking capabilities of our method, in Figure 2.3(b) the average particle displacement versus time is plotted for a handful of depths for one of the experiments. The pattern of the particle displacement clearly follows the triangle waveform driving the bottom plate, and the amplitude of displacement gradually increases proportionally to distance from the stationary plate, consistent with theory. To extract a shear rate, the particle velocity versus depth (Fig. 2.3(c)) is plotted for this same experiment. The theoretical trend line for the shear rate is displayed and a weighted linear regression is set to the data. The slope of the weighted fit is extracted as the shear rate (Eq. (2.2)) to be 0.22 ± 0.004 s^{-1}, compared to the theoretical shear rate of 0.21 s^{-1}, and the r-squared value of the weighted least squares regression is 0.996. In Figure 2.3(d), the results of all 22 experimental shear rates, obtained by varying the velocity while keeping all other parameters constant, are compared to the theoretical shear rates via a Bland-Altmann plot. Different values are expressed as percentages to better represent the relationship between experimental and theoretical results. Results of the Bland-Altmann plot are summarized in Table 2.1. The bias is -8.4% (95% CI, -18 – 1.2 %) within the limits of agreement (LoA) range of -51% to 34% that is principally caused by the lower shear rate measurements. Above 0.05 s^{-1}, the agreement range is less than 20%.

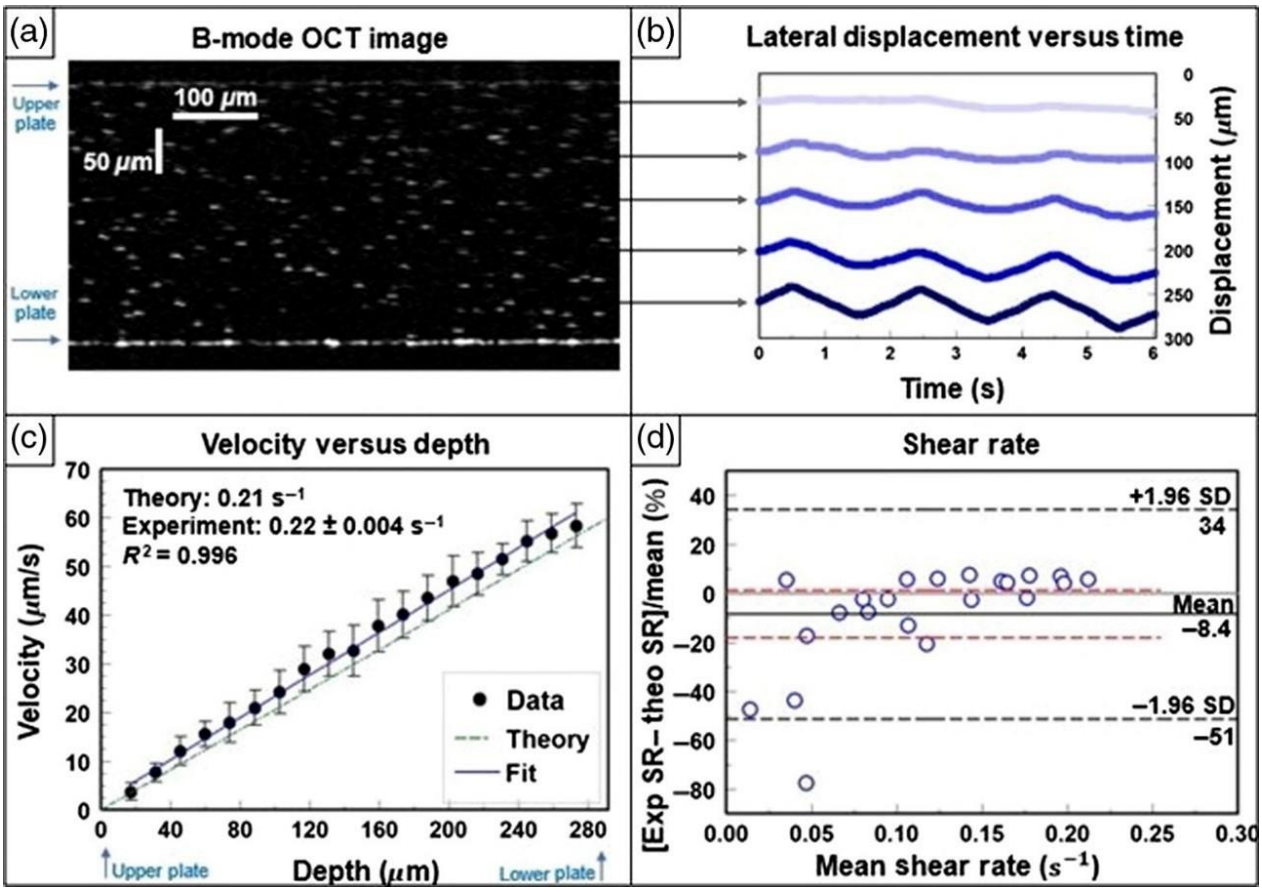

Figure 2.3: Newtonian fluid under constant shear rate in the MPPSIC. (a) OCT image of Sample 2, a glycerol:water solution of 294 mPa·s viscosity containing polystyrene microspheres as tracer particles between the glass plates of the MPPSIC separated by 292 μm. Image is cropped to 0.65 mm in the lateral direction (x) for clarity. (b) Corresponding traces of lateral particle displacements in Sample 2 when driven by a triangle waveform at the bottom plate with peak velocity of 60 μm/s and frequency of 0.5 Hz. Traces are shown at multiple depths in the sample, offset by their depth position for clarity. Corresponding movie of B-Mode OCT images (1.4 mm × 0.4 mm in $x \times z$) displayed at 2× real-time (Video 1, MP4, 2.9MB). (c) Corresponding waveform-averaged tracked particle velocity vs. depth; the best-fit line is used to extract the shear rate, which is compared to theory. (d) Bland-Altmann plot comparing results of measured shear rates over all experiments (n = 22) compared to theoretical shear rates. The difference is expressed as a percentage on the y-axis. The limits of agreement are marked by (black dashed lines), the bias (solid line), and 95% confidence interval of the bias (red lines). Velocity was varied while all other parameters were held constant for each sample's data collection.

2.5.2 MPPSIC Sinusoidal Velocity Performance on Newtonian Fluid

In Figure 2.4(a), an example OCT B-Mode image frame again shows the distribution of the microsphere tracer particles between the plates, now with a smaller separation distance. Taking a representative experiment, we see the sinusoidal pattern of the average particle displacement versus time in Figure 2.4(b) and note that the amplitude of displacement increases proportionally to distance from the stationary plate. In Figure 2.4(c) the fitted velocity amplitude for this experiment is plotted versus depth.

The theoretical trend line for the shear rate amplitude is displayed and a weighted linear regression is set to the data. The slope of the weighted fit is extracted as the shear rate amplitude (Eq 2.4) to be $4.84 \pm 0.11\ s^{-1}$, compared to the theoretical shear rate amplitude of $4.92\ s^{-1}$, and the weighted fit has an r-squared of 0.997. In Figure 2.4(d), the results of all 10 experimental shear rate amplitudes, obtained by varying the frequency while keeping all other parameters constant, are compared to the theoretical shear rate amplitudes (bias = 1.6 %; 95% CI, -0.28 – 3.4 %; LoA, -3.5 – 6.7 %). Similarly, the experimentally extracted frequencies are compared to corresponding theoretical values for all ten experiments Figure 2.4(e), and the phase lag of each experiment, calculated by a weighted average, is shown in Figure 2.4(f).

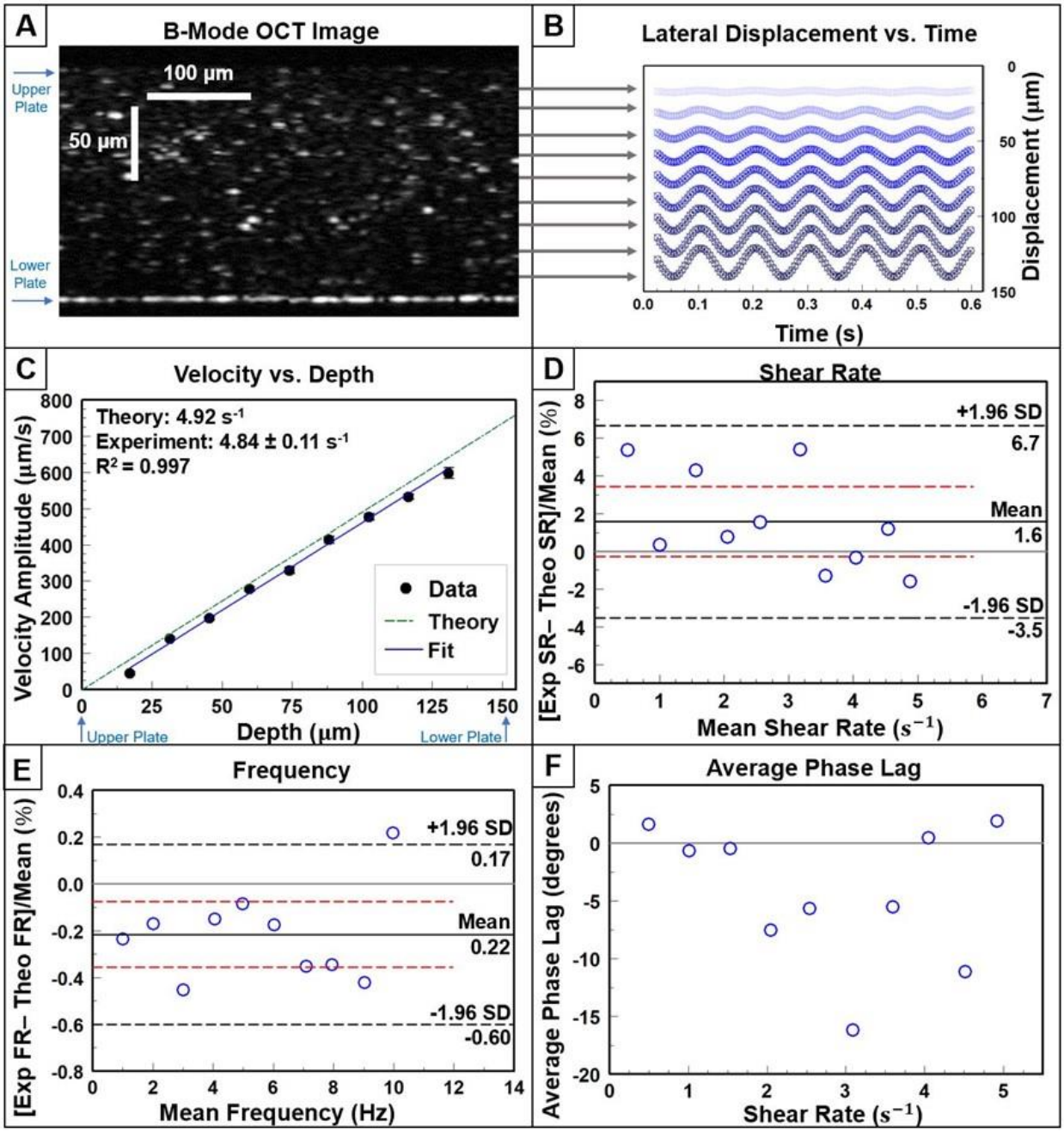

Figure 2.4: Newtonian fluid under sinusoidal shear in the MPPSIC. (a) OCT image of a glycerol:water solution of 347 mPa·s viscosity containing tracer particles in the MPPSIC with a glass plate separation of 154 µm. Image is cropped to 0.45 mm in the lateral direction (x) for clarity. (b) Corresponding traces of lateral particle displacements when driven by a sinusoidal waveform at the bottom plate with peak-to-peak displacement of 24 µm and frequency of 10 Hz. Traces are shown at multiple depths in the sample, offset by their depth position for clarity (5 of 6 waveforms shown). Corresponding movie of B-Mode OCT images (1.06 mm × 0.23 mm in $x \times z$) displayed at 0.33× real-time (Video 2, MP4, 1 MB). Error bars are not visible due to their small size. (c) Example waveform-averaged tracked particle velocity amplitude vs. depth; the best-fit line is used to extract the shear rate amplitude, which is compared to theory. Error bars are not visible due to their small size. (d) Bland-Altmann plot comparing results of measured shear rate amplitudes over all experiments (n = 10) compared to theoretical shear rate amplitude. The difference is expressed as

a percentage on the y-axis. The limits of agreement are marked by (black dashed lines), the bias (solid line), and 95% confidence interval of the bias (red lines). Frequency was varied while all other parameters were held constant for each sample's data collection. (e) Bland-Altmann plot comparing results of measured frequency over all experiments (n = 10) compared to theoretical frequency. The difference is expressed as a percentage on the y-axis. (f) Corresponding results of measured weighted average phase lag compared to theory ($\phi = 0$).

2.5.3 MPPSIC Sinusoidal Velocity Performance on Mucus

In Figure 2.5(a), an example OCT B-Mode image frame shows the dispersion of the polystyrene microspheres within the 1.5 wt% mucus sample, where additional scatterers endogenous to the mucus are also evident in the image. For one experiment, we see the sinusoidal pattern of the average particle displacement versus time in Figure 2.5(b) and similar to the results for the glycerol-water solutions, we find that the amplitude of displacement increases proportionally to distance from the stationary plate. In Figure 2.5(c) the fitted velocity amplitude for this experiment is plotted versus depth. To assess if there is a difference from Newtonian behavior, the Newtonian theoretical trend line for the shear rate amplitude is displayed and a weighted linear regression is set to the data. The slope of the weighted fit is extracted as the shear rate amplitude (Eq. (2.4)) to be $3.00 \pm 0.08\ s^{-1}$, compared to a theoretical shear rate amplitude (if Newtonian) of $3.16\ s^{-1}$, and the weighted fit has a r-squared of 0.991. Finally, the experimentally extracted shear rate amplitudes are compared to (Newtonian) theoretical shear rate amplitudes (bias = -4.9 %; 95% CI, -7.2 – -2.6 %; LoA, -13 – 3.6 %), as well as the experimental derived frequencies compared to corresponding theoretical values, for all 16 experiments Figure 2.5(d – e). The phase lag of each experiment was also calculated and shown in Figure 2.5(f). The phase lag of each row was minimal (less than 20 degrees) and considered negligible.

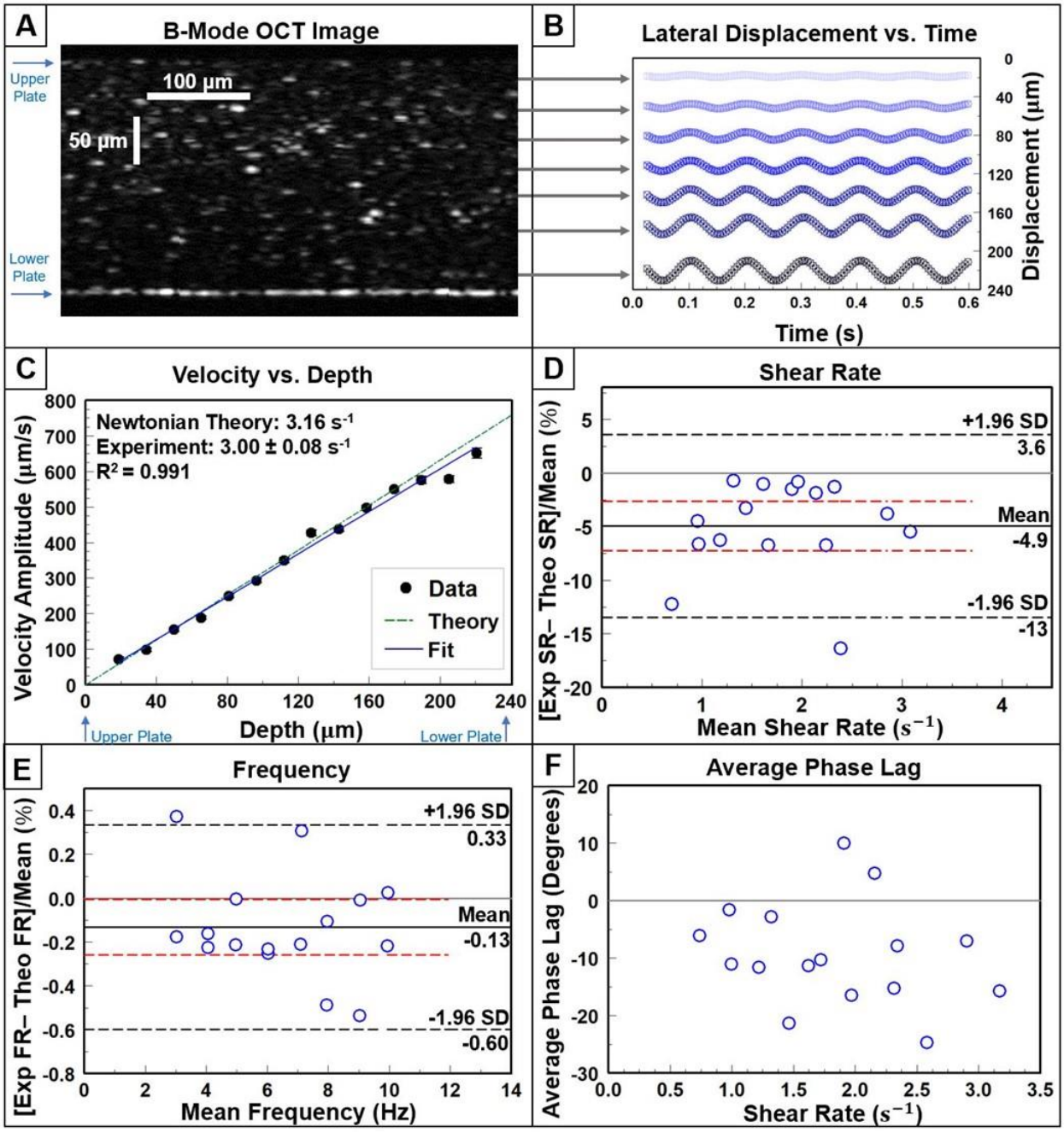

Figure 2.5: 1.5 wt% mucus under sinusoidal shear in the MPPSIC. (a) OCT image of a mucus sample containing polystyrene tracer particles in the MPPSIC with a glass plate separation of 242 µm. Image is cropped to 0.45 mm in the lateral direction (x) for clarity. (b) Corresponding traces of lateral particle displacements when driven by a sinusoidal waveform at the bottom plate with peak-to-peak displacement of 24 µm and frequency of 10 Hz. Traces are shown at multiple depths in the sample, offset by their depth position for clarity (5 of 6 waveforms shown). Corresponding movie of B-Mode OCT images (1.06 mm × 0.32 mm in $x \times z$) displayed at 0.33× real-time (Video 3, MP4, 1 MB). (c) Example waveform-averaged tracked particle velocity amplitude vs. depth; the best-fit line is used to extract the shear rate amplitude, which is compared to Newtonian theory (noting that mucus is, in general, non-Newtonian). Error bars are not visible due to small size. (d) Bland-Altmann plot comparing results of measured shear rate amplitudes over all experiments (n = 16) compared to Newtonian theoretical shear rate amplitudes. The difference is

expressed as a percentage on the y-axis. The limits of agreement are marked by (black dashed lines), the bias (solid line), and 95% confidence interval of the bias (red lines). Bland-Altmann plot comparing results of measured frequency over all experiments (n = 16) compared to theoretical frequency. The difference is expressed as a percentage on the y-axis. (f) Corresponding results of measured weighted average phase lag compared to theory ($\phi = 0$).

Table 2.1: Summary of key imaging parameters and results for all experiments.

Constant Velocity Experiment		**Sinusoidal Velocity Experiments**	
Frame Rate [Hz]	37.04	Frame Rate [Hz]	199
Line Rate [kHz]	10	Line Rate [kHz]	69.252
Number of A-Lines	250	A-Lines	208
Lateral scan distance [mm]	1.5	Lateral scan distance [mm]	1.2
Dead Time [ms]	2	Dead Time [ms]	2
Driving Frequency [Hz]	0.5	Peak-to-Peak Bottom Plate Displacement [μm]	18; 24

Aqueous Glycerol Sample		**Aqueous Glycerol Sample**		**Mucus Sample**
Bottom Plate Speed [μm/s]	Number of B-Mode Images	Driving Frequency [Hz]	Number of B-Mode Images	Number of B-Mode Images
5	800	3	396	396
10	800	4	294	294
15	600	5	240	240
20	600	6	198	198
25	400	7	168	168
30	300	8	150	150
35	300	9	132	132
40	200	10	120	120
45	200			
50	200			
55	200			
60	200			

		Bias [%]	**Lower Confidence Interval [%]**	**Upper Confidence Interval [%]**	**Lower Limit of Agreement [%]**	**Upper Limit of Agreement [%]**
Constant Velocity	Aqueous Glycerol Sample	-8.4	-18	1.2	-51	34
Sinusoidal Velocity	Aqueous Glycerol Sample	1.6	-0.28	3.4	-3.5	6.7
	Mucus Sample	-4.9	-7.2	-2.6	-13	3.6

2.6 Discussion

In this study, two sets of experiments were conducted with Newtonian fluids to test the functionality of the MPPSIC and develop motion tracking methods. A third set of experiments was conducted to observe the motion tracking capabilities of our method in a biofluid consisting of 1.5 wt% bronchial mucus. As shown in Figure 2.3, our method can track particle displacement, allowing us to extract the velocity of particles at various known depths when under constant velocity conditions. The depth-resolved velocities are consistent with a linear trend line (Fig. 2.3(c), $R^2 = 0.996$) as expected for a homogeneous, Newtonian fluid at low Reynolds number. The slope of the linear fitting for each depth-resolved experiment was used to experimentally determine the shear rate, which showed good correspondence (Fig. 2.3(d)) with the theoretical shear rate. However, the large limits of agreements range in Fig. 2.3 may be explained by the larger error our algorithm had in tracking shear rates lower than 0.05 s^{-1}. Error in trials considered "valid" by the algorithm may be the result of autocorrelation artifacts in the OCT image that appear near the top plate resulting in false tracking, or a lack of significant motion with lower waveform velocities. In the case of a slow-moving bottom plate, even with up-sampling and frame decimation techniques there may not have been enough frame-to-frame motion for adequate tracking. Trials in the experiment were unreported if considered invalid by the algorithm, such as when the analysis method was unable to proceed due to either the presence of large autocorrelation artifacts, which fails to pass the cluster check, or when the microspheres migrated towards the top plate, which fails to have a valid ROI in each depth.

As shown in Figure 2.4, the motion tracking algorithm performs well at quantifying shear rate amplitudes under sinusoidal shear in conditions close to those found in MCC (~1 – 10 s^{-1}), which are obtained when using a small plate separation and high frequencies. The tracked motion of particles within the fluid follows an expected sinusoidal displacement in time and constant gradient in depth as expected for a homogeneous Newtonian fluid at low Reynolds number. Our analysis method extracts velocity amplitude, frequency, and phase by fitting the average velocity waveform at each ROI depth. Figure 2.4(c) provides an example of results of one experiment, in which we can see the experimentally captured shear rate amplitude of 4.84 ± 0.11 s^{-1} is consistent with the theoretical shear rate amplitude of 4.92 s^{-1}. In Figure

2.4(d), we show that the MPPSIC algorithm can accurately extract shear rate amplitudes at up to 5 s^{-1}, which is within the range typically induced by cilia in the MCC. The line of equality falls within the 95% confidence interval of the bias and the limits of agreements are a narrow range of less than 10%. However, the same potential for analysis errors exists in the oscillating velocity experiment under constant velocity conditions. In addition to the above-mentioned contributions to error, we also become limited by the available frame rate of our OCT system, which is ~200 Hz when capturing ~200 A-lines as in these experiments. This contributed to error in the higher frequency experiments (~8 Hz and above), as the number of frames per waveform cycle became too low for adequate particle tracking. A potential future solution to this frame rate limitation would be to employ line field optical coherence tomography (LF-OCT) to image at kilohertz frame rates [26 – 28], with the added benefit of avoiding lateral beam scanning that can confound the analysis of image frames of moving particles.

Mucus samples were used for initial observations of MPPSIC particle tracking within a biofluid. Mucus concentrations are considered to be in a normal hydrated state at concentrations ~1.5 – 2 wt%. At a 1.5 wt% concentration, our mucus can be considered a sample representing the mucus in a well hydrated state.[15] Similar to the Newtonian fluid sinusoidal experiments, these experiments were conducted using shear rate amplitudes (up to 3 s^{-1}) extending into the range expected in the respiratory epithelium. However, the plate separation was somewhat higher (~240 μm) than the typical height of the mucus layer in the respiratory epithelium (~20 – 100 μm). The experiment shown in Fig. 2.5(a – c) was selected for display as it was performed at the highest velocity amplitude and thus most challenging to the motion-tracking algorithm. It was found that the time-course of the mucus motion appears to be sinusoidal at the fundamental frequency of actuation as well as in-phase with the actuation, suggestive of a linear elastic response of the mucus. A non-zero phase lag, particularly near the central depths of the sample, would be expected in the case of a non-linear depth profile, however the phase lag was negligible across all experiments. Furthermore, the mucus follows a linear velocity amplitude profile in depth (R^2 = 0.991 for the experiment shown in Fig. 2.5(b)), similar to Newtonian samples. Using the sinusoidal analysis method, we again extracted velocity amplitude, frequency, and phase from the average velocity waveform at each ROI depth.

The example experimental data in Figure 2.5(c) indicates that the experimentally captured shear rate amplitude of 3.00 ± 0.08 s^{-1} is similar, but not entirely consistent, with the Newtonian theoretical shear rate amplitude of 3.16 s^{-1}. Altogether, the data across all shear rate amplitudes (Fig. 2.5(d)) is consistently underestimated in comparison to Newtonian theory, with the line of equality falling outside of the bias 95% confidence interval (-7.2 – -2.6 %).

Our observations of the mucus velocity waveforms suggest that the shear strain amplitude applied to the mucus was not large enough to induce a nonlinear viscoelastic response, such as shear-thinning that might be expected for mucus. At a peak-to-peak displacement amplitude of 24 μm and plate separation of ~240 μm, there is ~10% shear strain on the sample, which is on the boundary between small amplitude oscillation shears (SAOS) and large amplitude oscillation shears (LAOS) [41], which may be required to measure non-linear responses in mucus. In addition, our observations of linear velocity amplitude profiles of mucus in depth are consistent with that expected for non-Newtonian fluids within the gap-loading limit, *i.e.*, when the plate separation is too small to support bidirectional shear waves. The maximum plate separation that lies within the gap-loading limit increases with the bulk shear modulus of the fluid and decreases with the frequency of actuation. Thus, even though mucus is generally a non-Newtonian fluid, the velocity amplitude depth profiles would be identical to that of a Newtonian fluid if experiments were conducted within the gap-loading limit [41].

These first observations in biofluids indicate we can track the depth dependence of flow in mucus samples under conditions that mimic the frequency and shear amplitude of the airway epithelium. With the capability to tune each of these parameters individually, the MPPSIC is ideal for exploration of fluid flow in physiologic conditions. Here we have shown our algorithm can track mucus flow across a relatively large dynamic range of flow velocities (5 – 700 μm/s) and over hundreds of microns in depth. In future experiments we can employ plate separations as low as 80 μm and deformation amplitudes as high as 100 μm, potentially quantifying how the viscoelastic and shear-thinning properties of mucus alter flow patterns in regimes that have not yet been observed. Another potential future application of the MPPSIC is to perform quantitative rheology on biofluids, which may be possible via the methods described in Mitran et

al. [49]. In the case of bronchial mucus as studied here, quantitative rheology may be feasible using larger plate separations and/or larger frequencies than those used in this study in order to move outside of the gap-loading limit. The ability to use OCT with the MPPSIC to actuate and depth-resolve biofluid flow, and subsequently to analyze the flow patterns with an extension of the Ferry shear wave model at a finite depth [49], presents a new opportunity to quantify the viscoelastic properties of fluids. Ultimately this can provide a new platform to investigate how changes in mucus concentration, layer height, and ciliary activity in the respiratory epithelium led to changes in fluid flow and the loss of MCC.

2.7 Conclusions

In summary, we propose a micro-parallel plate strain induction chamber for conducting particle tracking experiments in Newtonian and non-Newtonian fluid under dynamic shear while imaging with OCT. Our sinusoidal shear experiments in Newtonian fluid provide a depth-dependent velocity amplitude profile that is consistent with theory, demonstrating the functionality of the MPPSIC and motion tracking method. Furthermore, our results in mucus indicate the MPPSIC provides a new capability to study biofluids, such as mucus, to assess shear-dependent properties in a regime that is relevant to the mucus layer in lung epithelium.

CHAPTER THREE

IN SITU PULMONARY MUCUS HYDRATION ASSAY USING ROTATIONAL AND TRANSLATIONAL DIFFUSION OF GOLD NANORODS WITH PS-OCT

Mucus can be an expensive and time-consuming resource to harvest. To test new techniques for assessing mucus concentration, researchers can turn to our biopolymeric substances as mucus mimetic substitutes. This chapter presents experiments conducted in hyaluronic acid solutions (HA), agarose gels (AG), polyethylene oxide solutions (PEO) due to their usefulness in mimicking various pulmonary mucus properties [42 – 45]. We first quantify translational (D_T) and rotational (D_R) diffusion coefficients of plasmonic gold nanorods (GNRs) in HA, AG, and PEO solutions. We then extend our experiments to human bronchial epithelium (hBE) mucus, measuring D_T and D_R over a dynamic range of concentrations from hydrated and deemed 'healthy' state (< 2 wt%) to very dehydrated 'diseased-like' states (2 – 6.4 wt%). Importantly, as we demonstrate, the additional computation of D_R allows one to extend the dynamic range of available mucus concentrations to 6.4 wt%. Finally, using a model developed from the hBE experiment results, we estimate the concentration change over depth and time in air-liquid interface (ALI) hBEC cultures treated with hypertonic saline.

3.1 Why do we need both translational and rotational diffusion quantification in biomaterials?

Scanning electron microscopy (SEM), transmission electron microscopy (TEM), and confocal microscopy are commonly used to assess nanopore size due to their high resolution [30 – 34]. However, these techniques require segmentation for pore size measurements, generally require staining and, for electron microscopy, additional sample preparation. In comparison, an emerging technique involves measuring the diffusion rate of nanoparticles added to an aqueous macromolecular medium where they are weakly constrained due to intermittent and non-adherent collisions with the macromolecules [59]. This technique offers a promising alternative to traditional imaging methods, as it allows for minimally-invasive

measurement of the nanopore size distribution and subsequent estimation of the concentration of solids without the need for staining or segmentation. Plasmonic gold nanorods are particularly amenable to this technique because their optical resonance provides a large optical signal from particles that are sufficiently small (<100 nm) to access pores within a macromolecular medium that is well above the overlap concentration, as relevant to biomaterials.

The diffusion of GNRs have been assessed via using dynamic light scattering (DLS) and found to have predictable rotational and translational diffusion rates in water and aqueous glycerol solutions [36, 37], and diffusion of GNRs or related rod-like particles have been proposed for material characterization of polymer solutions [38, 39]. However, none of these studies have exploited the plasmonic resonance of GNRs to increase detectability within optically dense materials. Furthermore, an imaging platform such as optical coherence tomography (OCT) is particularly advantageous for performing depth-resolved DLS in biomaterials due to its increased depth penetration and small sample volume requirement [40, 41]. Chhetri et al.'s prior efforts have combined these two concepts, demonstrating DLS-OCT at the longitudinal surface plasmon resonance of GNRs to spatially resolve rotational [66] and translational [59] diffusion rates. In addition, the rapid speckle fluctuation rates exhibited by GNRs (with autocorrelation decay times typically < 10 ms) enable real-time imaging of GNR diffusion via DLS-OCT. This method is dubbed diffusion sensitive optical coherence tomography (DS-OCT) and has been shown to reveal temporally- and spatially-resolved changes in the nanostructure of polymer solutions, collagen, extracellular matrices, and well-hydrated *ex vivo* pulmonary mucus [35, 43, 44].

DS-OCT requires the collection of both co- (HH) and cross- (HV) polarized light scattering from the sample in order to compute both translational (D_T) and rotational (D_R) diffusion rates of GNRs. Chhetri et al. and Blackmon et al.'s previous work in pulmonary mucus focused only on computation of D_T as an indirect measure of mucus solids concentration (wt%) [58, 66]. By collecting D_T in stationary mucus samples, an interpolation curve relating D_T to wt% was exploited to depth- and time-resolve wt% within the mucus layer of an *in vitro* hBEC model during treatment by hypertonic and isotonic salines [67]. However, their methods were unable to extend to severely dehydrated, disease-like mucus concentrations

(> 3.5 wt%). In this chapter, we address this limitation by monitoring both D_T and D_R together, showing the interplay of how these two types of diffusion change as a function of sample concentration.

3.2 Diffusion Sensitive Optical Coherence Tomography Background

3.2.1 Polarization Sensitive OCT System

To track both translational and rotational diffusion, a key component of the experimental setup is the polarization sensitive signal collection of the OCT system. A detailed description of our custom polarization sensitive spectral domain OCT (PS-OCT) system can be found in previous literature [66], but here we provide a brief overview. The system utilizes an 800 nm center wavelength Ti:Sapphire laser (Griffin; KM Labs) with a 120 nm bandwidth as its light source, as shown in Figure 3.1.

A single mode fiber with polarization control directs the beam to a polarizing beam splitter, which ensures the polarization into the Michelson interferometer is horizontally (with respect to the optical table) polarized. A 50:50 beam splitter splits the beam into two paths: the reference arm and the sample arm. The stationary reference arm consists of a quarter wave plate and a retroreflector and the sample arm consists of two galvanometer scanning mirrors, typically with a 30 mm focal length lens is positioned below. The incident beam on the sample is horizontally polarized, while the returning reference beam as it returns from the retroreflector is linearly polarized at 45° (equal parts horizontal and vertical components). Light scattered from the sample interferes with the reference beam and the resulting co-polarized (HH – horizontal in and horizontal out) and cross-polarized (HV – horizontal in and vertical out) components are separated by a polarizing beam splitter and directed to a custom spectrometer. The spectral components of both polarization channels are dispersed by a diffraction grating and simultaneously imaged onto each half of a 4096-pixel line scan camera. The OCT system has an axial resolution of 3 μm and a transverse resolution of 12 μm in air, and the power directed on the samples was approximately 3.0 mW. Aline rates were either 25 kHz or 62.5 kHz as indicated in each experiment below.

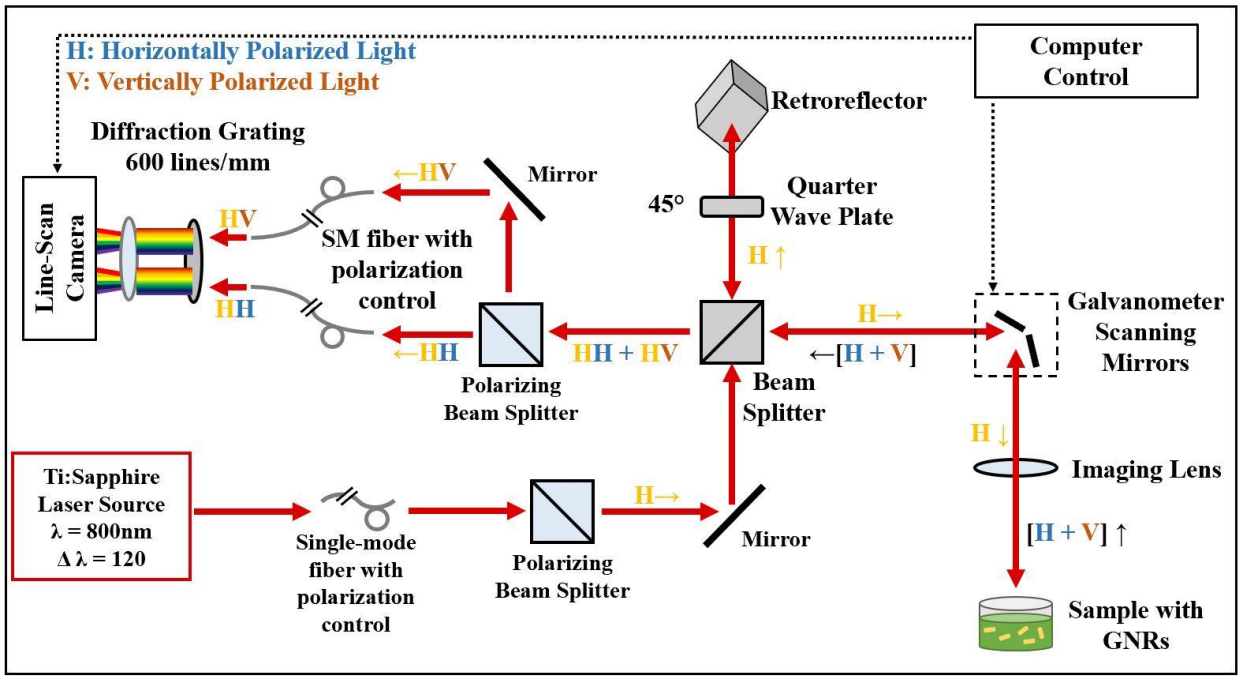

Figure 3.1: PS-OCT system schematic. A Ti:Sapphire laser source with a center wavelength of 800nm and a bandwidth of 120 nm is used. A 50:50 beam splitter splits the linearly and horizontally polarized beam between the reference arm and sample arm. The reference arm has a quarter wave plate fixed at 45 degrees. The interference signal is split by a polarizing beam splitter splits the co-polarized (*HH*) and cross-polarized (*HV*) signals to be recorded by the line-scan camera.

3.2.2 Gold Nanorods

Gold nanoparticles (GNPs) exhibit a significant enhancement of the electromagnetic field near their surface when illuminated with an oscillating magnetic field [69]. This enhancement arises from the collective coherent oscillation of free electrons within the positive metallic lattice where the frequency of the oscillation matches that of the electromagnetic field, forming a resonance known as localized surface plasmon resonance (SPR) [70]. Among the noble metals, gold is particularly advantageous due to its stable chemical properties [71], excellent biocompatibility [72], and strong SPR responses. GNPs possess strong optical scattering and absorption cross sections [73], making them ideal contrast agents for biomedical optical imaging. However, the limited adjustability of GNPs' SPR has led researchers to explore anisotropic gold particles to increase the SPR response in the near-infrared (NIR) range [74].

By adjusting the aspect ratio of gold nanorods (GNRs) [75], it is possible to achieve a robust localized surface plasmon resonance (SPR) response at near-infrared (NIR) wavelength, which is significant as the "biological window" for enhanced light transport in tissue also lies in the NIR [52, 53]. GNRs possess two distinct localized SPR modes: the transverse mode along the two short axes and the longitudinal mode along the long axis [78]. The longitudinal mode is particularly crucial for tuning the SPR into the NIR range. Additionally, it has been observed that light scattering from GNRs at the longitudinal SPR exhibits strong polarization parallel to the orientation of their long axis [79]. The scattering intensity of the localized longitudinal surface plasmon resonance (LSPR) is maximized when the incident polarization of the light beam aligns with the long axis of the GNR. Conversely, the LSPR becomes negligible when the incident polarization aligns with the short axis of the GNR.

There has been wide success with using GNPs and GNRs for contrast enhancement in OCT imaging [73 – 80]. Our OCT system's polarization sensitivity makes it a particularly advantageous imaging technique for quantifying nanoparticle diffusion in biofluids and biomaterials, alongside its depth-dependent imaging capabilities and small sample volume requirement [52, 81]. The small size of gold nanorods renders them highly permeable to biopolymer meshwork and tissues [89]. In this Chapter, four batches of GNRs were used in the experiments reported. The mean core sizes of each batch were: 68 × 19 nm for batch 1, 70 × 22 nm for batch 2, 80 × 22 nm for batch 3, and 84 × 24 nm for batch 4. Gold nanorods are synthesized by stabilizing cetyltrimethylammonium bromide according to a protocol defined in reference [90]. The gold nanorods are coated with a 1 k-Da molecular weight polyethylene glycol (PEG) methyl ether thiol (Sigma Aldrich) to keep the rods from adhering to polymer and mucin macromolecules. Transmission electron microscopy (TEM) was performed on all batches to measure their gold core size distributions and PEG coating thicknesses. The PEG coating thickness was ~0.48 nm for all batches. Our GNR sizes are chosen to be on the same scale as the nanopore size of mucus (~0.2 – 1 μm [91]), therefore their Brownian motion is expected to be hindered by the mucus macromolecules and corresponding diffusion rates are expected to depend on the mucus concentration.

The reason for this behavior is that a particle typically exhibits diffusion if it is smaller than the correlation length of the polymer, while it experiences hindered movement if it exceeds the correlation length [92]. The hydrodynamic radius of GNRs refers to their effective size within a fluid environment. The correlation length (ξ) of a polymer relies on factors such as the polymer's concentration, overlap concentration (c*), and radius of gyration [92]. The radius of gyration is dependent on the molecular weight of the polymer, whereas the overlap concentration depends on both the molecular weight and the radius of gyration of the sample. The hydrodynamic radius (R_H) of GNRs in each of the batches, ~19 nm, 22 nm, 24 nm, and 24 nm, respectively, are calculated using GNR length (L) and width (W) according to [59]:

$$R_H = \frac{L}{2(\ln(\frac{L}{W}) + 0.312 + 0.565(\frac{W}{L}) - 0.1(\frac{W}{L})^2)} \tag{3.1}$$

3.2.3 DS-OCT and Diffusion Coefficients Calculations

As a brief review of DS-OCT analysis methods, as previously described by Chettri et al. [59], DS-OCT consists of collecting M-mode OCT images of a GNR-laden sample to depth-resolve (z) translational (D_T) and rotational (D_R) diffusion coefficients. M-mode OCT images can then be collected at varying lateral positions (x) or at successive times (t) to construct a cross-sectional (x-z) or dynamic (t-z) image of D_T and D_R; in this study we perform cross-sectional imaging on stationary samples (PEO, mucus) and dynamic imaging on the mucus layer of *in vitro* ALI hBEC cultures.

For each M-mode OCT image, comprised of A-lines sampled at times t_s, the co- (HH) and cross- (HV) polarized complex analytic OCT signals, $\tilde{S}_{HH}(t_s; z)$ and $\tilde{S}_{HV}(t_s; z)$ respectively, are computed from raw OCT data by standard methods. At each z position the time averages are subtracted, then the normalized temporal autocorrelations $\left(g_{HH}(\tau; z), g_{HV}(\tau; z)\right)$ are computed. To suppress noise, the autocorrelations are then averaged in depth windows of 20 pixels or less; each window is considered an ROI (region of interest). By the Siegert relation these second-order autocorrelations are equated to first-order

autocorrelations $g^{(1)}(\tau;z)$ which, for GNRs at their longitudinal resonance, are related to D_T and D_R as follows (33):

$$g^{(1)}{}_{HH}(\tau;z)=\frac{5}{9}\exp\left(-q^2D_T(z)\tau\right)+\frac{4}{9}\exp\left(-6q^2D_R(z)\tau\right) \tag{3.2}$$

$$g^{(1)}{}_{HV}(\tau;z)=\exp\left(-6D_R(z)\tau-q^2D_T(z)\right), \tag{3.3}$$

where $q=4\pi n/\lambda_0$, n is the refractive index of the medium, and λ_0 is the central wavelength of the PS-OCT system. From a linear combination of Eq. 3.2 and Eq. 3.3, we calculate the isotropic autocorrelation, $g_{ISO}(\tau;z)$, which isolates the D_T term as follows:

$$g^{(1)}{}_{ISO}(\tau;z)=\frac{9}{5}g^{(1)}{}_{HH}(\tau;z)-\frac{4}{5}g^{(1)}{}_{HV}(\tau;z)=\exp\left(-q^2D_T(z)\tau\right) \tag{3.4}$$

Under our experimental conditions, the 1/e decay time associated with D_T is much longer than that associated with D_R, which simplifies Eq. 3 to isolate the D_R term as:

$$g^{(1)}{}_{HV}(\tau;z)\approx\exp\left(-6D_R(z)\tau\right) \tag{3.5}$$

Decay times τ_{ISO} and τ_{HV} are extracted by fitting Eq. 3.4 for $\tau\le\tau_{1/e}$ and Eq. 3.5 for $\tau\le\tau_{1/e^2}$, where $\tau_{1/e}$ and $\tau\le\tau_{1/e^2}$ are the delay times at which $g^{(1)}$ falls below $1/e$ and $1/e^2$, respectively; this excludes noisy tails in the autocorrelations from the analysis. One exception to this rule was PEO solutions with concentrations > 1.5%, for which a fit range for Eq. 3.5 only up to $\tau_{1/e}$ was used. For *in vitro* hBEC cultures, a dynamic τ_{ISO} threshold was applied such that a fit range of $\tau\le\tau_{1/e^2}$ was used if fittings had fewer than 4 data points. For all fittings, if fewer than 4 data points were available, the ROI was excluded from further analysis. Also, the zero-delay point $g(\tau=0)$ was excluded from all fittings to avoid the contribution of shot noise.

Several criteria were used to determine which ROIs were valid for analysis. First, we use a top surface detection method to exclude ROIs above the sample or too close to the top surface which exhibits a strong specular reflection. For PEO and stationary mucus samples, valid ROIs start 15 pixels below the top surface detected, and 5 pixels below for the hBEC cultures. ROIs are 20 pixels in depth for stationary mucus and 3 pixels in depth for hBEC cultures. Second, we exclude ROIs that are below an average co-polarization (*HH*) signal threshold above the background noise. Third, we excluded ROIs that do not meet our criteria for valid decay times discussed in [68]. Briefly, we reject ROIs where the decay anisotropy $\tau_{ISO} / \tau_{HV} < 1.5$, because dynamic scattering from GNRs exhibits higher decay anisotropy. Additionally, τ_{ISO} and τ_{HV} must lie within the dynamic range of the OCT system (significantly longer than the sampling time and shorter than the total acquisition time). Fourth, we applied a threshold for autocorrelation fits based on the coefficient of determination (R^2). For PEO solutions $R^2 > 0.88$, and for stationary mucus $R^2 > 0.90$. Fifth, for PEO and stationary mucus samples, all diffusion coefficients more than five standard deviations from the mean were assessed visually for air bubbles and other imaging artifacts and manually excluded if appropriate. The fourth and fifth methods were not applied to *in vitro* hBEC culture studies because mucus hydration was expected to be heterogeneous and dynamically changing.

The same data collection protocol was used for all HA, AG, PEO, and stationary mucus samples. cross-sectional (*x*-*z*) B+M-mode images (3 mm × 1.5 mm in *x* × *z* in the sample) comprised of 30 M-mode images with 30,000 A-lines each were collected sequentially at a line rate of 62.5 kHz. Samples were imaged sequentially under the same room temperature conditions. Each sample was imaged in two elevationally displaced (*y*) locations for greater spatial averaging.

3.3 Diffusion of Gold Nanorods in Hyaluronic Acid

Hyaluronic acid (Sigma Aldrich) solutions were prepared from a 4.5 wt% stock solution. To prepare the stock solution, HA was stirred in room temperature distilled water. From the stock solution, samples were serially diluted to achieve a range of concentrations, with imaging performed at each 0.5 wt% increment until reaching a final concentration of 1 wt%. Gold nanorods from batch 4 (84 × 24 nm) were

added to each sample at 1% solids by volume. HA samples were imaged in polystyrene microwells with the PS-OCT system.

The translational diffusion of GNRs in solvent (distilled water) is approximately 6.5 μm^2/sec and decreases rapidly with increasing concentration. When HA is initially diluted to a concentration of 1 wt%, D_T decreases further to less than 1 μm^2/sec. Figure 3.2(B) illustrates the rotational diffusion rate of GNRs measured within the same samples as the translational diffusion. In the lower concentration samples, D_R shows a similar dependence on concentration as D_T, indicating hindered diffusion with increasing concentration. However, contrary to our findings for D_T, D_R continues to decrease across all concentrations. The initial D_R in solvent exceeds 3500 rad^2/sec and slows down by a factor of 10 at the highest reported sample concentration (4.5 wt%).

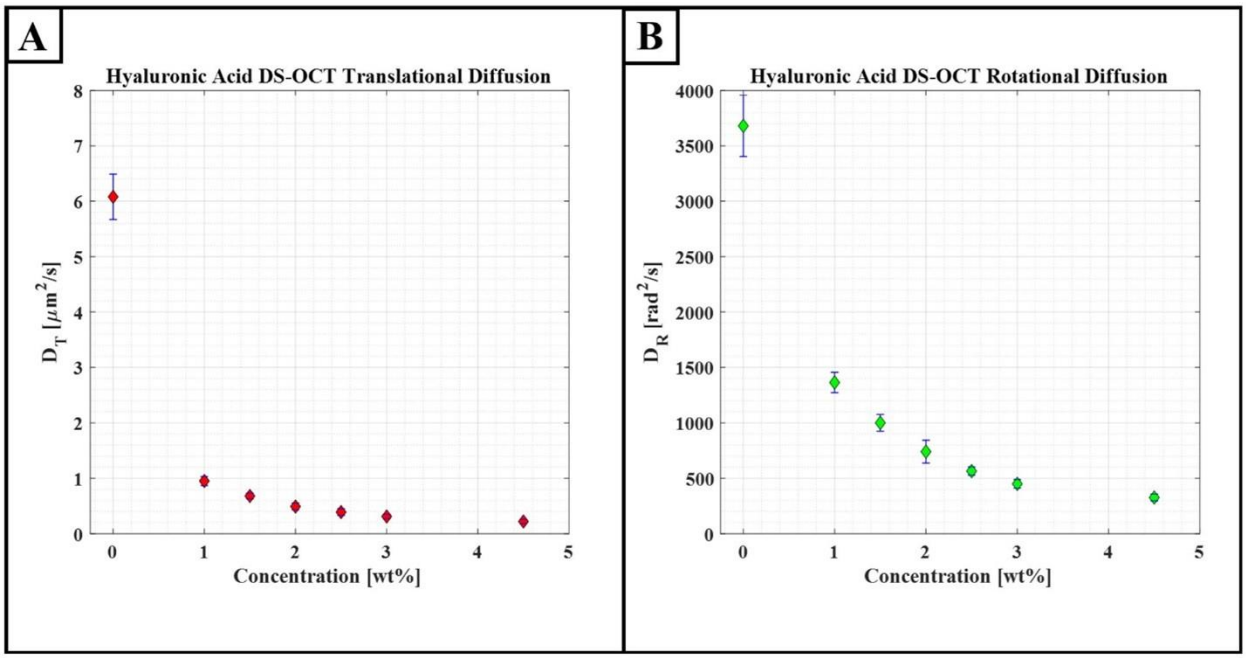

Figure 3.2: Gold nanorod diffusion in hyaluronic acid solutions. D_T and D_R are plotted as a function of HA concentration. In many cases error bars are not visible due to small standard deviation size. Zero concentration represents GNR diffusion in solvent (distilled water). A Kruskal Wallis test confirmed all values all have statistically significantly difference from each other.

3.4 Diffusion of Gold Nanorods in Agarose Gels

Agarose gels (Sigma Aldrich) were prepared from a 3 wt% stock solution, which was subsequently diluted to obtain individual samples with solids ranging from 0 to 2.77 wt%. To prepare the stock solution,

distilled water and low gelling temperature agarose powder were mixed and stirred at room temperature. The mixture was then heated in a microwave to warm it up, and any evaporated water was replenished. For DS-OCT imaging, we need to add gold nanorods (batch 1: 68 × 19 nm) to each sample at a concentration of 1% by volume. To effectively disperse GNRs into agarose, the agarose must be warmed up to 30°C to be in a liquid state. Having to warm up the sample to disperse GNRs raises three primary concerns: the maximum duration for which the GNRs can be heated without any alterations to their properties, the rate at which the sample transitions to a gel state (i.e., the cooling time required before imaging), and how long the gels stay hydrated. We must determine the appropriate cooling duration for the sample and the feasibility of reheating previous samples for additional experiments.

Regarding the impact of temperature on the durability of GNRs, we investigated the absorption spectrum of GNRs using transmission spectroscopy. We heated the sample, comprised of 1% total volume GNRs in distilled water, in a 90°C water bath for two specific time intervals. Four separate samples were prepared for analysis: one without any GNR heating, one heated for 15 minutes in the water bath, one heated for 30 minutes, and one heated for 60 minutes. Transmission spectroscopy measurements were immediately performed on each sample after removal from the water bath. The optical depth versus wavelength was plotted for all four samples in Figure 3.3(A). There is a noticeable difference in the peak wavelengths between the heated GNRs and those that were not heated, pointing to a potential change in the aspect ratio of the GNRs due to their degradation. Based on this experiment, we can conclude the shortest possible heating duration should be used to minimize degradation of the GNRs.

To address the remaining concerns regarding cooling time and sample hydration, we imaged the same sample at three specific time points. The first DS-OCT images were collected approximately 3 minutes after sample creation which was the amount of time it took to set up the sample for imaging with the PS-OCT system. Subsequent imaging took place at the 30-minute and 60-minute marks post-creation. To prepare the sample, we initially warmed a 3% stock solution in an 80°C water bath. An aliquot of the sample was then transferred into a centrifuge tube to be mixed with distilled water and GNRs to achieve the desired concentration. To ensure thorough mixing, the sample was further warmed for 15 minutes in

the water bath, followed by rigorous agitation. Finally, the sample was transferred to a polystyrene well for imaging with the PS-OCT system. To ensure repeatability, this experimental procedure was replicated at multiple concentrations across a concentration range of 0-2.77 wt%. The sample was left exposed in the microwell without any additional measures being taken to maintain its hydration.

The objective of this second experiment was twofold: to measure D_T and D_R of GNRs across various concentrations of agarose gels, and to investigate the impact of sample cooldown time and handling time on the obtained results. Figure 3.3(C) illustrates D_T in distilled water, which is approximately 6.5 μm^2/sec, decreasing rapidly as the agarose gel concentration increases. Across all timestamps, D_T slows down to less than 1.5 μm^2/sec at concentrations higher than 1 wt%. Figure 3.3(D) displays D_R measured within the same samples used for the translational diffusion analysis. In lower concentration samples, D_R exhibits a similar dependence on concentration as D_T, indicating hindered diffusion with increasing agarose concentration. The results from the 3-minute timestamp demonstrate faster diffusion compared to those given time to cool and gel. Furthermore, for the 30-minute and 60-minute timestamps, D_R reaches a plateau at 1.75 wt% concentration. The disparity in diffusion rates between the lowest and highest concentration samples is more pronounced in the 3-minute timestamp experiments than in the 30-minute and 60-minute timestamps. Although the samples may appear gel-like to the naked eye, the agarose gels require sufficient time to fully gel and should not be imaged too quickly after removal from the water bath. Moreover, for all concentrations, D_T and D_R results obtained in the 30-minute and 60-minute timeframe show minimal changes, indicating that our gels are usable for at least an hour.

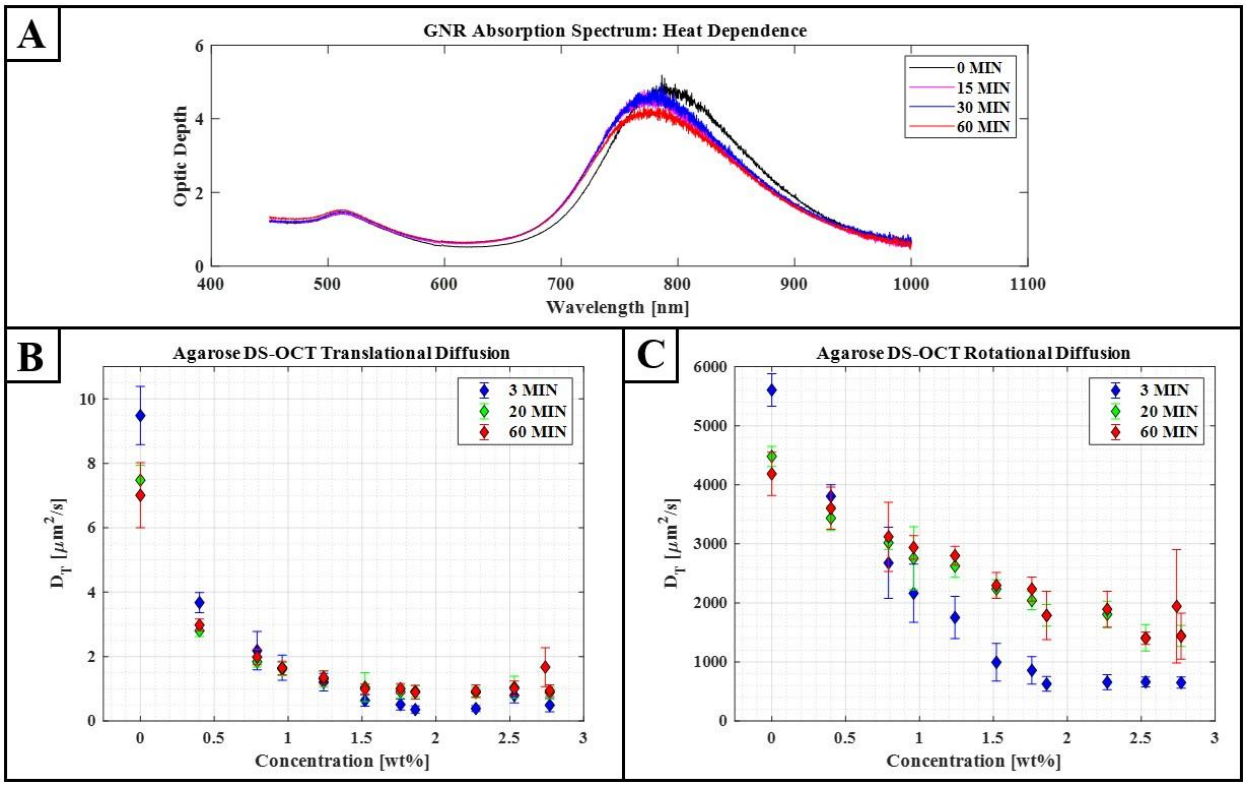

Figure 3.3: Gold nanorod diffusion in agarose gels. In panel A, the absorption spectra of GNRs heated at four different time intervals are shown. In panels (B) and (C), D_T and D_R are plotted as a function of agarose solids concentration. Zero concentration represents GNR diffusion in solvent (distilled water).

3.5 Diffusion of Gold Nanorods in Polyethylene Oxide Solution Samples

Polyethylene oxide (PEO) of molecular weight (M_W) 4 MDa was prepared into 5 wt% stock solutions. To prepare a stock solution, PEO powder was stirred constantly in 80°C distilled water for one week. From the stock solution, samples ranging from 0 – 3 wt% solids were prepared. GNRs (batch 1: 68 × 19 nm) were added to each sample to a final concentration of 1% solids by volume, which is low enough to avoid significant contributions from particle-particle collisions. Polymer solutions were imaged in polystyrene microwells with the PS-OCT system.

The following experiments involved measuring GNR diffusion rates in PEO solutions because they are easily accessible, and at Megadalton molecular weights their nanostructure can closely resemble that of mucus [53]. Figure 3.4 summarizes these measurements, which were spatially resolved within x-z cross-sections of PEO solutions of varying concentrations, then averaged as described above to provide a single value of D_T and D_R for each concentration. The top panel of Figure 3.4(A) illustrates the concentration-

dependence of the D_T of GNRs in 1 MDa and 4 MDa PEO, which exhibits a similar trend as in , Chhetri et al.'s previous report using 1 MDa PEO samples with differently sized GNRs [59]: D_T in solvent (distilled water) is ~8.5 μm^2/sec and decreases rapidly as concentration increases. At concentrations higher than 1 wt%, D_T slows down to less than 1 μm^2/sec. The middle panel of Figure 3.4(A) shows the rotational diffusion rate of GNRs measured within the same samples as translational diffusion. The concentration dependence of D_R in 4 MDa PEO exhibits the same trend observed in D_T such that diffusion is hindered by increasing concentration. However, in contrast with the D_T results, the decay of D_R with concentration is less rapid, and D_R continues to decrease across all higher concentrations. D_R is greater than 5000 rad^2/sec in solvent and is reduced by a factor of 10 at our highest sample concentration reported (3 wt%). As shown in the lower panel of Figure 3.4(A), in lower concentration samples (< 1 wt%), the variability (or precision) of D_T and D_R is < 10%. At higher concentrations the variability of the D_T measurements increases well over 10%, while D_R measurements maintain low variability across all samples. Figures 3.4(B) and 3.4(C) display examples of spatially-resolved diffusion measurements at low and high concentrations of PEO. Both D_T and D_R diffusion maps appear to be homogeneous with no spatially-varying noise, which is consistent with PEO samples being well-mixed. However, in the higher concentration sample of Figure 3.4(C), D_R is defined in nearly twice the number of ROIs defined by D_T.

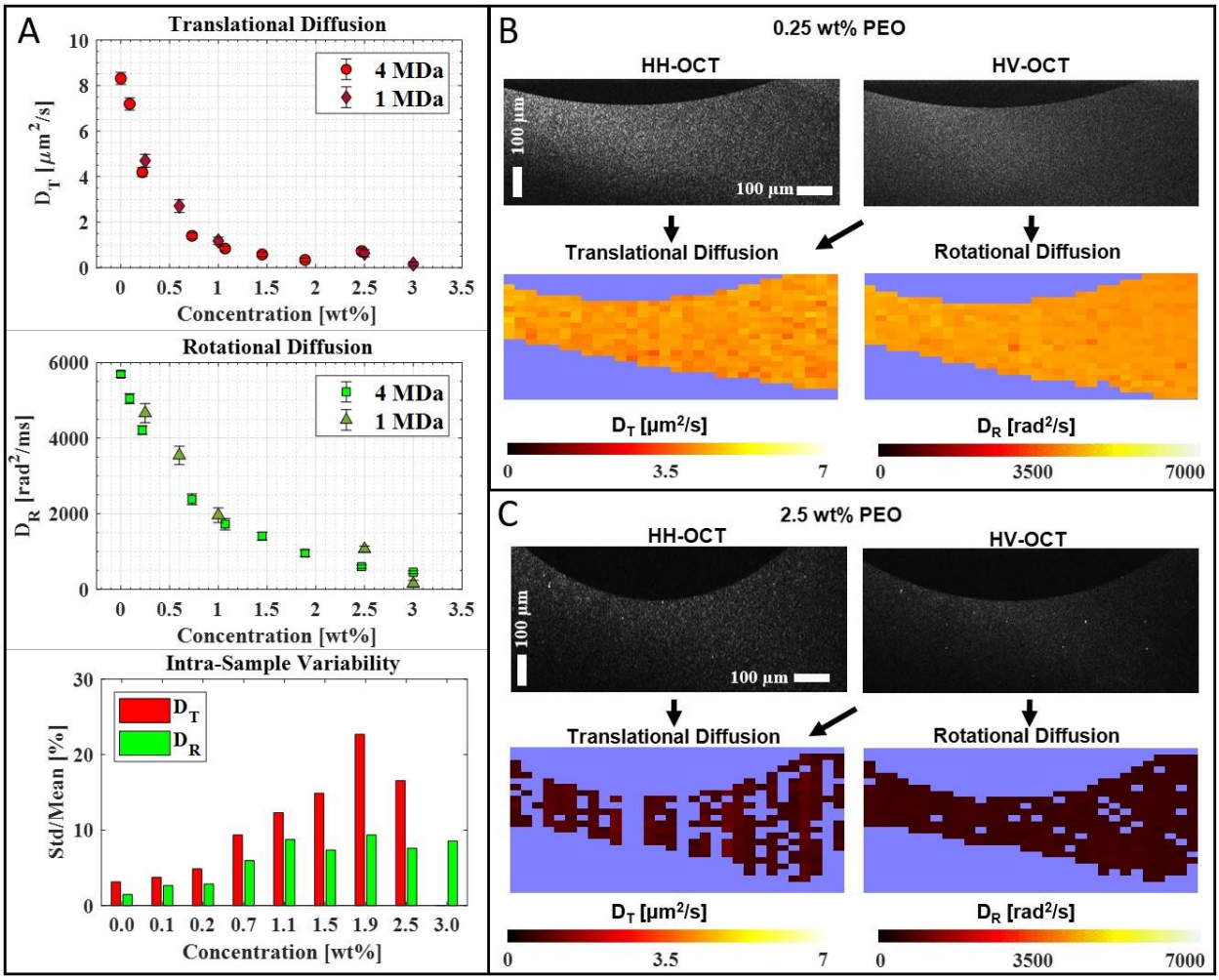

Figure 3.4: GNR diffusion in aqueous 1MDa and 4 MDa PEO solutions. In the top panels of A, D_T and D_R are plotted as a function of PEO solids concentration. In many cases error bars are not visible due to small standard deviation size. Zero concentration represents GNR diffusion in solvent (distilled water). In the bottom panel, intra-sample variability is presented as the percent ratio of the standard deviation to the mean for both D_T and D_R. In panels B and C, co-polarized (*HH*) and cross-polarized (*HV*) B-mode images of the 0.25 wt% and 2.5 wt% PEO solutions are displayed along with corresponding D_T and D_R values within each ROI derived from B+M-mode images; excluded ROIs based on thresholding criteria described in the methods are displayed as the background color.

The magnitude of the reduction in GNR diffusion in PEO solutions compared to solvent depends on the degree to which the GNRs are confined by the PEO meshwork. The relative degree of confinement may be thought of in terms the size of the hydrodynamic radius of the GNRs, R_H, compared to the correlation length of the polymer solution, ξ. In prior work, , Chhetri et al. defined a weakly-constrained regime as one where D_T was reduced by less than a factor of 10 from that of solvent, and found that this occurred when $R_H / \xi < 2.2$ in 1 MDa PEO [59]. In these experiments in 4 MDa PEO, we observe a reduction in D_T by a

factor of 10 at PEO concentrations ≥ 1.1 wt%, which, given an R_H of 19 nm for this nanorods batch, and ξ of 14 nm for 4 MDa PEO at 1.1. wt%, corresponds to a weakly constrained regime defined by $R_H/\xi < 1.4$. For concentrations above 1.1 wt%, which we will consider to be strongly constrained, D_T was no longer monotonically decreasing, and could not be extracted at the highest concentration of 3.0 wt%. In comparison, D_R continued to monotonically decrease for increasing concentration in the strongly constrained regime, which effectively extends the dynamic range of measurable PEO concentrations to 3.0 wt% and possibly further. Added support for the ability to extend the dynamic range is seen by assessing the intra-sample variability, where fine D_T and D_R precision is evident in the weakly constrained regime, while only D_R precision is fine in the strongly constrained regime.

There are several potential explanations for the varying responses of D_T and D_R versus PEO concentration. First, D_T measurements tended to exhibit lower R^2 values from autocorrelation fittings; this caused many ROIs to be rejected via criterion 4 above where the R^2 threshold was applied, as observed in Fig. 3.4(C) at 2.5 wt%; it is also the reason D_T could not be extracted at the highest concentration measured (3.0 wt%). We believe the lower R^2 for D_T is either due to the longer τ_{ISO} values at high concentrations which become a significant fraction of the measurement time, causing noise artifacts in the autocorrelation traces, or possibly because the strongly constrained GNR motion no longer fits a model that can be described by simple diffusion. In comparison, D_R depends only upon τ_{HV}, which is always shorter than τ_{ISO} for the GNRs in our experiments due to decay anisotropy [68]; as GNR confinement increases and decay times increase, the smaller τ_{HV} better remains within the dynamic range of the measurement compared to τ_{ISO}. The fact that D_R is more easily measurable may also suggest a fundamental difference in how diffusive prolate particles rotate versus translate during strong confinement in polymeric solutions, an area of active research [93].

3.6 Diffusion of Gold Nanorods in Human Bronchial Epithelial Mucus Samples

The stock mucus samples were harvested from hBEC cultures and diluted to concentrations ranging from 1 – 6.5 wt% with 1X DPBS (Distilled Phosphate Buffered Saline). GNRs were mixed into individual

mucus samples to a final concentration of 1% volume fraction. GNR batch 2 (70 × 22 nm) was used in both Trials 1 and 2. Samples were imaged in polystyrene microwells with the PS-OCT system.

In previous publications [35, 43], Chhetri et al. and Blackmon et al. reported that D_T is sensitive to hBE mucus concentrations ≤ 2.5 wt%, both stationary and *in vitro*. Mucus ≤ 2 wt% is considered well-hydrated and would be expected during a state of 'healthy' pulmonary mucus production. To extend the capability of DS-OCT to measure the lower mucus hydration levels associated with pulmonary disease-like states, we must perform diffusion experiments on more heavily dehydrated mucus samples (> 2 wt%). Here, we expand our investigation of GNR diffusion to a broader range of mucus concentration, up to 6.4 wt%, and report values of D_R in hBE mucus for the first time.

As shown in Fig. 3.5(A), while Trial 2 tended to exhibit higher D_T and D_R values at all mucus concentrations relative to Trial 1, similar concentration-dependent trends were observed overall. In mucus samples below 2 wt%, D_T quickly decreases with respect to concentration while remaining above 2 μm^2/sec. For GNRs in dehydrated mucus (> 2 wt%) we observe a general trend that D_T slows at smaller increments with increasing concentration and plateaus at ~0.5 μm^2/sec (Fig. 3.5(A)). In well-hydrated samples, D_R retains a significant fraction of its value in solvent, above ~3000 rad^2/s, then gradually decreases with further increases in mucus sample concentration. At the highest reported wt%, D_R is calculated to be ~ 1000 and ~1500 rad^2/s in Trials 1 and 2 respectively. Across all reported sample concentrations, outside of the solvent data, the variance in D_R is less than half of that observed in D_T. D_T intra-sample variability is over 10% in all reported concentrations over 1 wt%, while D_R variability remains under 10%.

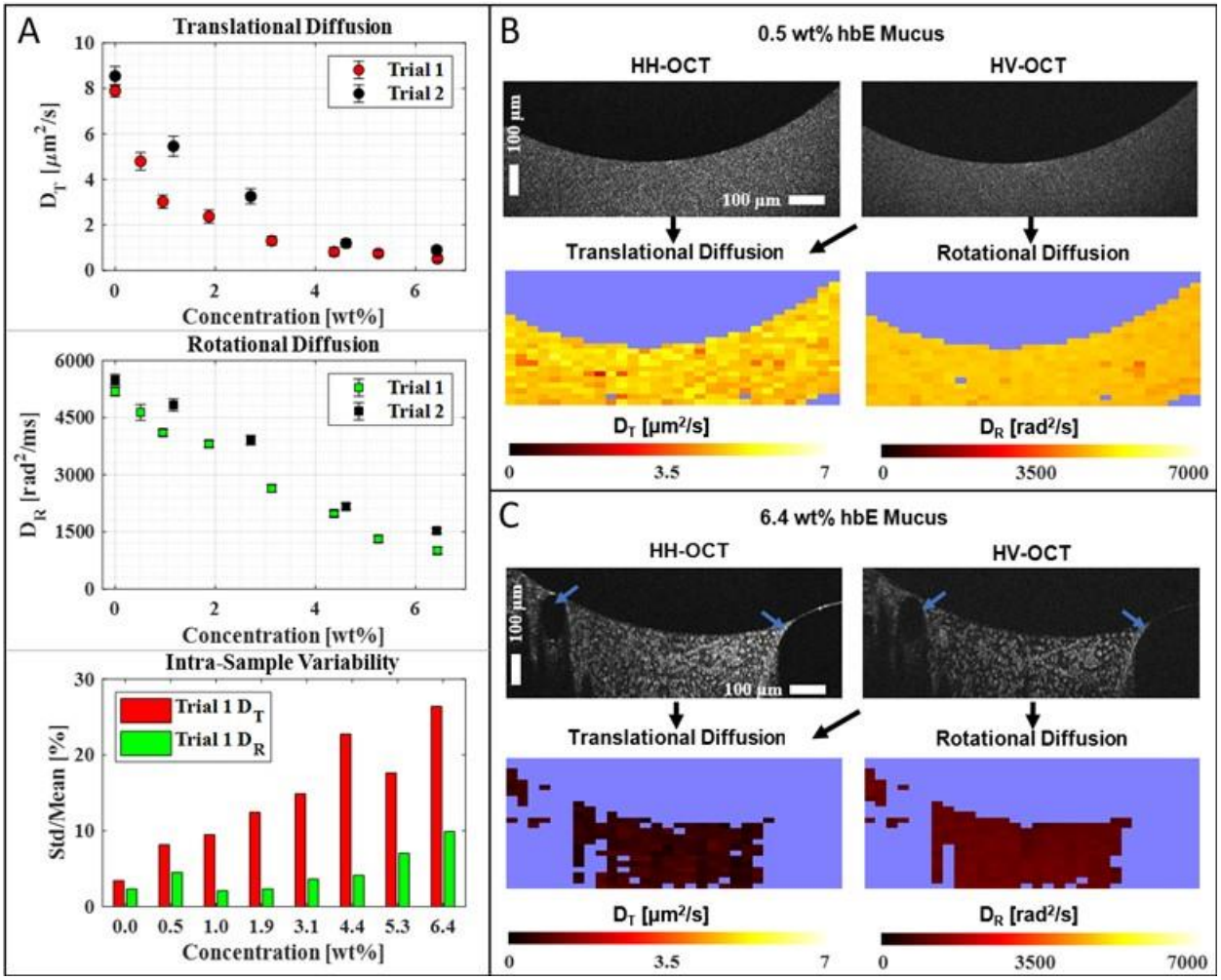

Figure 3.6: GNR diffusion in hBE mucus sample. In the top panels of A, D_T and D_R are plotted as a function of mucus solids concentration. In many cases error bars are not visible due to small standard deviation size. Zero concentration represents GNR diffusion in solvent (distilled water). In the bottom panel, intra-sample variability is presented as the percent ratio of the standard deviation to the mean for both D_T and D_R. In panels B and C, co-polarized (*HH*) and cross-polarized (*HV*) B-mode images of the 0.5 wt% and 6.4 wt% hBE samples are displayed along with corresponding D_T and D_R values within each ROI derived from B+M-mode images; excluded ROIs based on thresholding criteria described in the methods are displayed as the background color. In panel C, multiple ROIs are rejected due to air bubbles (indicated by blue arrows) in the 6.4 wt% sample.

Overall, the trends in D_T and D_R versus mucus concentration closely mirror those observed in PEO solutions. If we define, as for the PEO experiments above, a weakly constrained regime of GNR diffusion as that when D_T is ≥ 1/10 the value in solvent, GNRs transition to being strongly constrained when mucus concentration exceeds ~4.5 wt%. However, D_R continues to be sensitive to mucus concentration in this strongly constrained regime. Also, similar to results in PEO, diffusion colormaps of the highest wt% sample in Fig. 3.5(C) show that there are multiple ROIs where D_R is defined while D_T is not (criterion 4). We

note that samples in trials 1 and 2 were mixed under slightly different temperatures, potentially contributing to the observed differences in D_T and D_R. The higher wt% samples are prone to air bubbles during the mixing process, an example of which can be seen in Fig 3.5(C). Large areas of rejected ROIs are due to air bubbles.

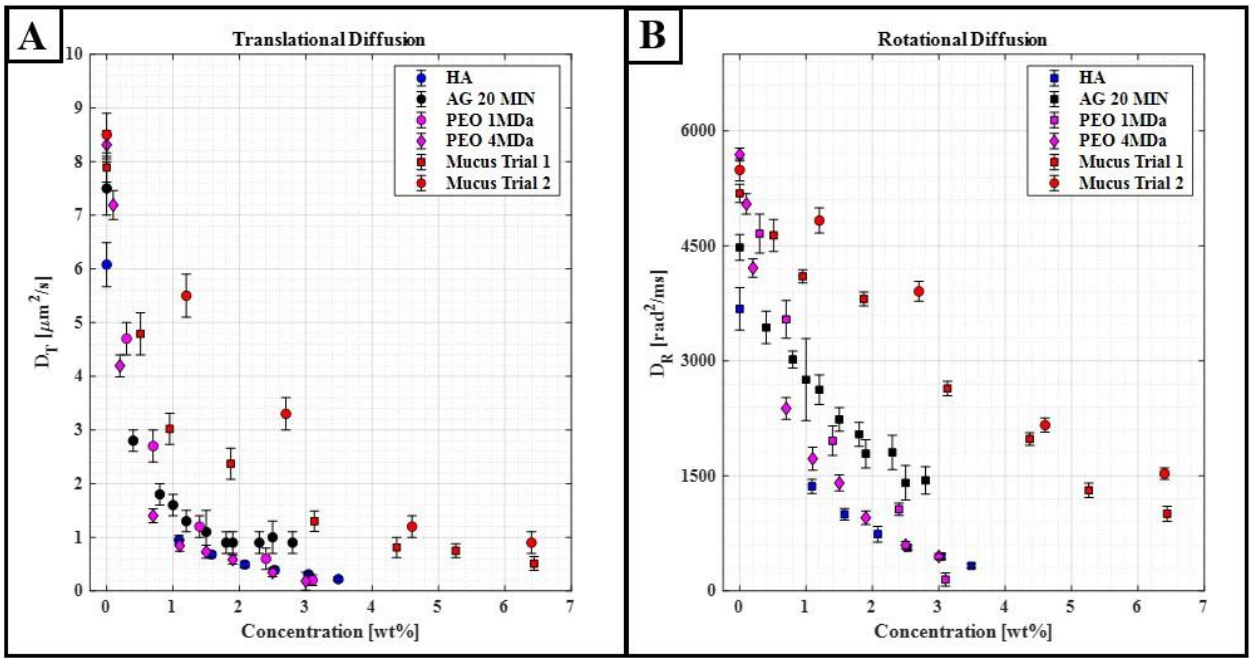

Figure 3.6: Gold nanorod translational and rotational diffusion in HA, AG, PEO, and mucus.

In Figure 3.6, we compare GNR diffusion in pulmonary mucus to three previously discussed samples (HA, AG, 1 and 4 MDa PEO) and find that mucus exhibits a similar concentration-dependence. As the concentration increases, both translational and rotational diffusion decrease. Notably, the translational diffusion of a dehydrated mucus sample (6.4 wt%) closely resembles the diffusion observed in HA, AG, and PEO samples ranging from approximately 1.5-2.75 wt%. Similarly, for rotational diffusion, a 6.4 wt% mucus sample demonstrates a comparable rotational diffusion rate to other concentrations between 1.5-2 wt%. The observation that the diffusion rates of HA, AG, and PEO samples in the 1.5-2.75 wt% range are comparable to mucus diffusions holds significant practical implications. This finding suggests that when designing experiments involving similar nanostructures to those found in pulmonary mucus, we can utilize these materials as viable alternatives.

3.7 Implementation of Diffusion to Concentration Mapping as a Pulmonary Mucus Hydration Assay

3.7.1 Mapping Diffusion Coefficients to Mucus Concentration

While D_T measurements are a valid tool for assessing the nanostructure of well-hydrated mucus samples, these results with mucus point to D_R being more sensitive to the concentration of dehydrated mucus samples. Incorporating our previously published translational diffusion in hBE mucus results in [59] and the above reported hBE experiments, we can define an assay for estimating the concentration of mucus given diffusion coefficient measurements. We first normalized all diffusion coefficients with respect to the diffusion coefficient in solvent measured on the same day, $D_{norm} = D / D_{solvent}$. A linear regression was then taken of $D_{T,norm}$ vs wt% over a well-hydrated range (0 – 2 wt%), resulting in:

$$wt\% = -2.75 D_{T_{norm}} + 2.53 \tag{3.6}$$

with $R^2 = 0.86$. Similarly, a linear regression of $D_{R,norm}$ over all concentrations (0 – 6.4 wt%) was found to be:

$$wt\% = -8.62 D_{R_{norm}} + 8.14 \tag{3.7}$$

with $R^2 = 0.95$.

To apply this assay, we collect D_T and D_R measurements in a mucus sample and solvent (saline), then compute weight percents from Eq. 3.6 and Eq. 3.7. If the wt% falls between -0.5 and 2% for D_T, or between 1 and 8% for D_R (extrapolating somewhat from the maximum measured value of 6.4 wt%), we consider it valid and exclude values that fall outside these ranges. In the case where we have valid wt% values from both D_T and D_R, we take the average. One limitation of this method is the potential variation in R_H values among different batches of gold nanorods. To help account for potential nanorod size variability in D_T measurements, we incorporated three GNR batches with distinct sizes when calculating the D_T trendlines. The GNR batch used in this experiment has a size of 70 × 22 nm with a corresponding R_H of 22 nm. The additional two batches of GNRs incorporated from our previous publication [59], sized 83 × 22 nm and 62 × 10 nm, had corresponding R_H of 24 nm and 19 nm.

3.7.2 ALI Culture Data Set Background

Calu-3 cells were cultured under air liquid interface (ALI) conditions [60, 61]. After ten days, when there was adequate lumenal mucus accumulation, cells were maintained at ~37ºC in HEPES-buffered HBSS based solution (basolateral solution) for imaging. A 10 μL isotonic saline and GNR mixture was pre-mixed to contain ~1% by volume batch 3 GNRs (80 × 22 nm) and deposited 6 hours before OCT imaging. After initial images, a 10 μL hypertonic saline and batch 3 GNR mixture, ~1% by volume, was deposited on top of the cell culture. Cell cultures were imaged near the well wall at a 10-to-20-degree angle to avoid imaging the meniscus. The image collected of this data set was performed by previous lab member Richard Blackmon. 99 total M-mode images comprised of 4,000 A-lines were collected at a line rate of 25 kHz all at the same transverse location in the sample. The dynamic (*t*-*z*) M-mode images were collected every 3.3 seconds for 4.5 minutes, and then every 13.3 seconds for an additional 4 minutes.

3.7.3 Results and Discussion

To mimic the airway epithelium physiology, Calu-3 cells were cultured under ALI conditions. The cell cultures were imaged with PS-OCT immediately before and over the course of 8.5 minutes after treatment with hypertonic saline (HTS). The mucus layer, which already contained GNRs introduced 6 hours prior, was ~400 μm thick before saline introduction. After topically introducing HTS with additional GNRs, the layer was ~600 μm thick. In Figure 3.7(A), we observe D_T of GNRs in the mucus layer of the ALI culture over depth and time. We define a depth of zero as the top of the epithelium where mucus is secreted from mucus goblets. Initially D_T is rapid, with rates much higher than 7 $\mu m^2/s$ during HTS introduction. After 1 minute, D_T is measurable in ROIs close to the air-liquid interface but exhibits an increasing number of invalid ROIs in regions below, closer to the epithelium, likely due to high wt% that is outside the measurement range for D_T. Interestingly, at depths closer to the epithelium, D_T starts to increase after 3 minutes, while it decreases near the top surface, resulting in a more homogenized value of D_T over depth at 8.5 minutes.

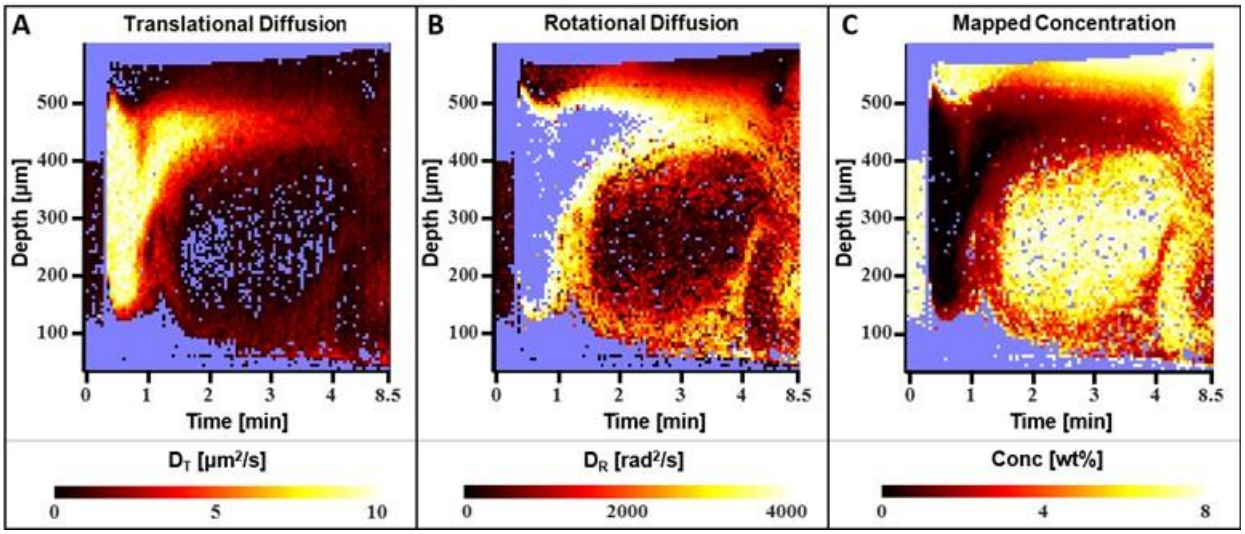

Figure 3.7: D_T and D_R in ALI cultures with HTS introduced are color mapped in panels A and B. In panel C, the diffusion coefficients are mapped to mucus concentration using trendlines produced from stationary mucus experiments. If an ROI had a valid measurement of both D_T and D_R, the calculated concentrations were averaged for a final reported value.

Figure 3.7(B) reveals the corresponding D_R of GNRs in the mucus layer of the ALI culture. Over the first minute D_R is largely undefined in between the air-liquid interface and the epithelium. The regions of interest that are quantified have high D_R, greater than 3500 rad^2/s. Beyond 2 minutes, D_R in ROIs close to the surface remain consistently high. Underneath this area, a tall mass of high concentration mucus is revealed by D_R measurements in which the diffusion is hindered more than those at the air-liquid interface. Comparing Figures 3.7(A) and 3.7(B), we see the complimentary nature of D_T and D_R, with D_T having fewer invalid ROIs in regions of lower wt% and D_R accessing higher wt% regions; while at the same time, the overlapping ROIs of the two appear to follow the same depth- and time-resolved trends.

Using the trendlines defined in Eq. 3.6 and Eq. 3.7 for relating D_T and D_R measurements to mucus concentration, in Figure 3.7(C) we mapped the concentration of the mucus within the ALI cell culture in depth and time. By employing the new calibration method which exploits the complimentary nature of the two diffusion coefficients, we produce a more spatially and temporally contiguous plot. Before HTS is introduced (at time periods <~20 s), mucus appears hard-packed within a 400 μm layer. Immediately after HTS is introduced, we observe a ~500 μm layer of liquid that appears to be mostly solvent, then a thin, highly concentrated layer of mucus near the air-liquid interface. Over time, high wt% mucus also appears

lower down near the epithelium, while the depth-dependent wt% is generally heterogeneous. Between 4 and 8.5 minutes the mucus appears to continue to mix and homogenize, likely as a result of ciliary activity on the epithelium, which we have found is more active in response to HTS than to isotonic saline [67]. Bearing in mind that "healthy" mucus is considered to be ~2 wt%, we see that the mucus layer is nearing, but has not quite reached, this value by the end of the experiment. In previous publication [67], Blackmon et al. observed the re-initiation of the MCC in time-lapse OCT images during HTS treatment on hBEC. These results suggest the promising advantages of incorporating a combination of our advanced DS-OCT-based assay with regular OCT imaging for a comprehensive evaluation of the HTS treatment process in future applications.

3.8 Conclusions

The mucociliary clearance system is the respiratory system's main defense mechanism to inhaled pathogens. Pulmonary diseases, such as CF and COPD, cause mucus to become severely dehydrated and leaves individuals prone to infection. Hypertonic saline is commonly used to hydrate the mucus to promote better function of the MCC. In this article we present, for the first time, a method of using translational and rotational diffusion rates of GNRs introduced into the HTS to develop an *in situ* assay of mucus hydration levels. Because mucus is a limited resource, we first quantified diffusion rates in polyethylene oxide solutions. The rotational diffusion was less hindered than translational diffusion in strongly confining PEO concentrations. A similar effect was observed in stationary hBE mucus samples. From the measurements in stationary mucus samples, we were able to fit a model to calculate precent weight concentration given D_T and D_R. Applying this model to an hBEC cell culture treated with HTS, we demonstrated that rotational diffusion could provide information of mucus hydration levels up to 6.4 wt% and may estimate even more highly concentrated mucus as evidenced by extrapolating the regression line out to 8.0 wt%.

It is noteworthy that GNRs can be biocompatible [96]. GNRs have the potential to be nebulized and administered to the lungs via inhalation. Upon delivery, we would expect them to disperse throughout a highly concentrated mucus layer within minutes. Importantly, GNRs are not expected to penetrate the lung

epithelium based upon their size and the exclusion properties of the airway barrier [3], and should eventually cleared by the MCC. Future applications of measuring both translational and rotational diffusion of gold nanorods can lie in vast biomedical research areas as biopolymeric meshes are ubiquitous. Overall changes in nanopore size or anisotropy are related to a host of medically relevant processes and diseases. In particular, anisotropic nanostructure may arise from cilia inducing shear on the macromolecular meshwork of mucus, or from ECM-altering cells during ECM remodeling processes. For this purpose, Marks et al. has previously curated a new technique called diffusion tensor OCT (DT-OCT) to determine the anisotropy of a macromolecular pore size using our DS-OCT methods [97]. The initial steps for implementing this technique's will be discussed in chapter 4.

In summary, quantifying the rotational diffusion of GNRs in conjunction with translational diffusion can provide reasonable estimates of mucus hydration levels, applicable to therapeutic treatment monitoring. By incorporating rotational diffusion measurements, the dynamic range of sample concentration expands to include dehydrated mucus concentrations. This enhanced sensitivity allowed for the development of a real-time assay to study mucus hydration *in situ*.

CHAPTER FOUR

EXPLORING DIRECTIONAL DIFFUSIVITY OF GOLD NANORODS IN BIOMATERIALS USING DIFFUSION TENSOR OCT

4.1 Motivation for Sensing Sample Anisotropy

We put forward the hypothesis that mechanical strain exerted by cilia on mucus in the bronchial epithelium leads to alterations in the nanopore shape of the mucin meshwork. However, as highlighted in section 3.1, conventional imaging techniques such as SEM and TEM have inherent limitations in assessing nanostructures. These methods often involve destructive sample preparation [30 – 34]. To address the need for improved imaging techniques for evaluating the structural anisotropy of biomaterials, we can leverage the techniques discussed earlier in this dissertation. In Chapter 3, we demonstrated the usefulness of OCT for quantifying the translational and rotational diffusion of gold nanorods and showed the relation between diffusion rates to sample concentration. With this in mind, we extend our hypothesis to suggest that the applied strain by the MCC on the macromolecular meshwork will result in elongated pores along the axis of strain while constricting the pores along the perpendicular axis. We expect to observe faster diffusion along the elongated side of the nanopores and slower diffusion perpendicular to the axis of strain. Therefore, by measuring the diffusion of gold nanorods under the induced strain we may be able to quantify the extent of changes in the nanostructure. Currently, our DS-OCT technique has limitations as it does not enable the assessment of diffusion directionality other than along the axis of the beam. To address this limitation, we propose an advancement of the DS-OCT imaging technique known as Diffusion Tensor OCT (DT-OCT) [97]; one proposed implementation of DT-OCT involves measuring GNR diffusion along six unique illumination directions to quantify the six independent components of the diffusion tensor. In this chapter, we develop the necessary hardware to facilitate these measurements.

4.2 Diffusion Tensor OCT Theory

The investigation of anisotropy in tissue or biopolymers at a cellular scale can be achieved through the application of the Diffusion Tensor OCT (DT-OCT) technique. A description of the DT-OCT methods can be found in a publication by Marks et al. ([97]). In this overview, we present the key principles of DT-OCT, drawing inspiration from Diffusion Tensor Magnetic Resonance Imaging (DT-MRI).

DT-MRI is a closely related technology that leverages the Brownian motion of water molecules to evaluate the organization of axons in the brain [75 – 79]. The anisotropic diffusion of water is observed, such that faster rates along the long axis of the axonal fascicle and slower rates along the short axis. By measuring anisotropic diffusion, the orientation and connectivity of axonal fibers can be assessed. Unlike DT-MRI, our proposed DT-OCT method is limited to measuring diffusion of particles with sufficient light scattering for detection by OCT. However, our OCT method has the advantage of potentially cellular-level resolution.

Diffusion Tensor Optical Coherence Tomography is a technique used to study the diffusion of particles within an arbitrary sample using an arbitrary coordinate system. The diffusion process is characterized by the diffusion tensor, which is Hermitian and comprises 6 unique elements (Figure 4.1(A)). Diffusion is assessed along at least 6 unique directions, coinciding with the directions of the light beam as it enters the sample. While a minimum of 6 measurements are necessary, more measurement directions are preferred for enhanced accuracy. To collect these measurements, a periscope is employed to redirect the beam to the outer edge of a lens such that it enters the sample from an oblique angle of light incidence, θ_S, for angular diversity.

The recorded diffusion tensor elements are expressed in the laboratory's coordinate system. The 6 unique diffusion tensor elements are estimated solving a linear system of equations and subsequently diagonalizing the tensor. The rotation operations that diagonalize the tensor represent the angle of the sample's coordinate system (its principal axes) relative to the measurement coordinate system. The 3 unique elements along the diagonal represent the diffusion values (D_{xx}, D_{yy}, D_{zz}) along the principal axes. In cases

where the diffusion exhibits certain types of symmetry, such as axisymmetry, the number of unique elements can be further reduced, for instance, by setting D_{yy} equal to D_{zz} and defining anisotropy $R = \frac{D_{xx}}{D_{zz}}$.

In this Chapter, we propose utilizing GNRs translational diffusion measurements, leveraging the prior data obtained in Chapter 3. We hypothesize that GNRs will diffuse faster along the direction of stretch and diffuse slower perpendicular to it, due to the alignment of fibers in the stretched system. A periscope will be used to direct the light beam with an incidence angle, θ_S, and a rotation angle of $\theta_R = 30°$. We will collect 12 measurements while simultaneously stretching the sample within the plane transverse to the central axis of the lens, as depicted in Figure 4.1(D). The 12 measurements will be collected by rotating the periscope between 0 to 360 degrees at θ_R increments. These measurements will later be used to compute the diffusion tensor. However, the first crucial step is to validate that the measurements collected with this DT-OCT hardware will remain constant over periscope scanning in an isotropic sample to ensure accurate and reliable results.

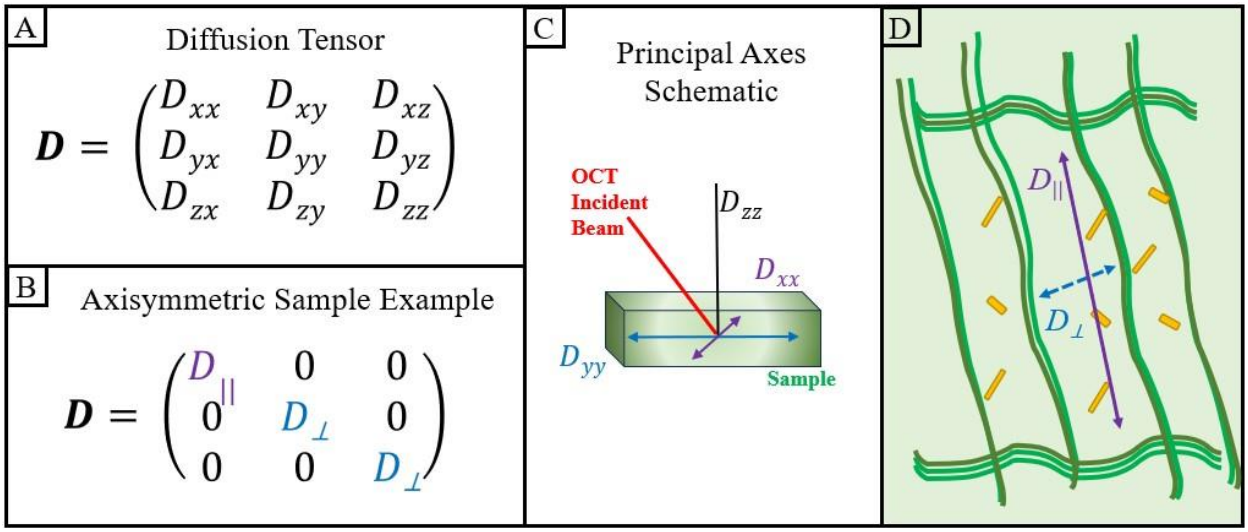

Figure 4.1: Panel A displays the diffusion tensor. Panel B is the diffusion tensor example for an isotropic sample. In the axisymmetric case, the off-diagonal components become zero, and only two unique measurements, $D_{||}$ and $D_{\perp}$, are required to characterize the tensor. Panel C is a schematic to clarify how we define our principal axes. With our original DS-OCT method, the incident OCT beam is co-aligned with D_{zz}. Here we instead show the incident beam at an angle, which is desired for DT-OCT. Panel D depicts an illustrative example of an elongated pore containing gold nanorods immersed in the sample, demonstrating the experimental setup and our definitions of $D_{||}$ and $D_{\perp}$ for the known-strain example given in this section.

4.3 Design of DT-OCT Hardware

4.3.1 Hardware Design Constraints and Parameters

We can accomplish DT-OCT measurements by introducing the beam into a sample from different directional positions while maintaining a fixed focal spot. A simple approach for achieving this positional beam redirection is to utilize the combination of a periscope and an aspherical focal lens. A periscope can be added into the sample arm's beam path such that when the periscope rotates it will be redirecting the beam to equally spaced locations along the outer edge of the focal lens. By introducing the beam along the outer edge of the lens, the outcoming beam will have both a fixed focal spot and fixed incident angle into the sample, as shown in Figure 4.2(B).

When choosing a focal lens, the outgoing angle should be carefully considered to ensure our measurements in an anisotropic sample ($R > 1$) can be distinguished from measurement in an isotropic sample ($R = 1$). To avoid indistinguishable measurements, we can calculate the minimum angle of incidence (θ_S) required based on a maximum tolerated anisotropy measurement standard error (σ_R) according to:

$$\theta_S \geq \tan^{-1}\left(\frac{1}{\sqrt{\left(\left(\frac{\sigma_R}{\sqrt{2}f}\right)-R\right)}}\right), \tag{3.8}$$

where f is the expected fractional error of the diffusion measurements. For this calculation we can base the fractional error on the average standard error in our prior DS-OCT measurements, which gives $f = 0.6$. If our goal is to sense even a small change in anisotropy, such as $R = 2 \pm 0.5$ or $R = 3 \pm 1.5$, this would correspond to a minimum θ_S ranging from 14.5° – 26.9°.

There are two parameters to consider when designing the periscope: timing and distance. First, the periscope needs to be motorized for fast image acquisition across a minimum of twelve M-Mode images. A quick data collection time, on the scale of seconds, is typically targeted to account for fluid relaxation or to prevent sample dehydration. The second consideration is the available path length in the sample arm.

While our OCT system is custom built, we must consider that there is a limit to which the reference arm path length can be extended. This limits us to ~80 mm of path length in the sample arm, which limits the gap size between the periscope mirrors.

Finally, to facilitate precise alignment the hardware design should provide multiple degrees of freedom. For optimal alignment the hardware design should accommodate three degrees of freedom for lateral translation and an additional two degrees of freedom for tilt adjustment. We additionally aimed to incorporate a design that allows the OCT system to return to its normal configuration by rotating the periscope away about the sample arm, which introduces an additional rotational degree of freedom. In total, a desirable design would provide a total of six degrees of freedom to enable adjustable alignment.

4.3.2 Hardware Set-Up and Control Configurations

A custom compact periscope was designed to be introduced into the sample arm of the DT-OCT setup. The design is illustrated in Figure 4.2 and comprises five main components: two galvanometer mirrors, a motorized rotational stage (ThorLabs, Inc.), a custom compact periscope, a quarter waveplate, and an aspherical focal lens. The galvo mirrors serve as folding mirrors and direct the beam downward. The remaining components are all connected within a single cage system, as shown in Figure 4.2(C). The periscope is mounted onto the underside of the rotational stage. Beneath the periscope, there is a quarter waveplate held in a manual rotational mount which allows us to set the waveplate to a desired fixed position. The quarter waveplate compensates for any polarization changes induced by the periscope's mirrors before reaching the edge of the focal lens. This will be discussed in more detail in section 4.3.4

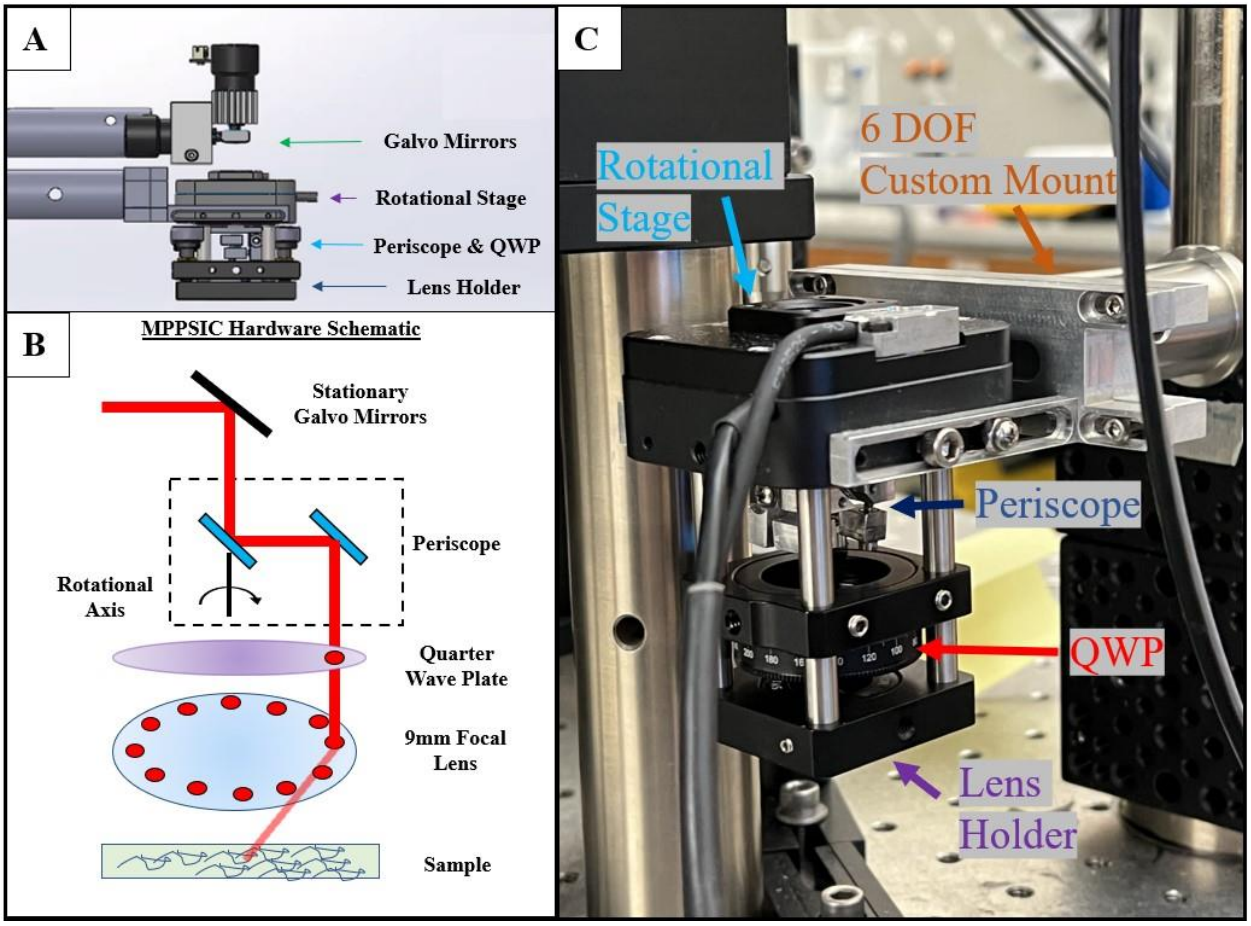

Figure 4.2: DT-OCT Hardware Design. Panel A displays a SolidWorks CAD model of the design. A schematic of the design and principle are shown in panel B. Panel C shows a photograph of the DT-OCT cage system rotated out of the PS-OCT sample arm.

A suitable focal lens that allows us to achieve the desired targeted angle (θ_S) can be found by considering a lens's numerical aperture (NA), effective focal length (EFL), periscope gap distance (D_p), and clear aperture (CA) diameter, following the equation:

$$\theta_S = \tan^{-1}\left(\frac{CA - D_p}{EFL}\right). \tag{3.9}$$

For D_p = 4 mm, we chose an aspherical focal lens (Edmunds Optics) with a clear aperture of 12.7 mm, an EFL of 9 mm such that the beam exits the lens at an angle of approximately 27.6° degrees with a working distance of ~5 mm. The control protocol for DT-OCT is described in Appendix C, while the alignment procedure is outlined in Appendix D.

4.3.3 Custom Compact Periscope Design

To accommodate the short working distance and compact size requirements of the DT-OCT hardware design, a highly compact periscope was essential. The periscope mirrors are positioned approximately 4 mm apart to redirect the beam along the outer edge of the lens. For alignment purposes, each periscope mirror required two degrees of freedom, specifically left-right tilt and up-down tilt. A custom periscope and mirror holders were designed to work within the path length space constraints. Using SolidWorks, we developed a design to fabricate mirror holders using aluminum, as shown in Figure 4.3. The mirror holders were designed with two rotational degrees of freedom. Two 5 mm diameter silver mirrors (Edmund Optics) were securely fixed into the mirror holders.

Moreover, the periscope design was machined to be compatible with a commercially available motorized rotational stage. We specifically chose the DDR25 rotational stage (Thorlabs, Inc.) due to its speed, ability to be aligned as an optical alignment cage system with a lens holder, and the presence of a hole in the center of the stage allowing the beam to pass through to the first periscope mirror. The rotational stage is controlled through the OCT system's LabVIEW software, enabling the user input to control the velocity and angular step size prior to image acquisition. A custom plate was machined to connect the mirror holders to a rotational stage.

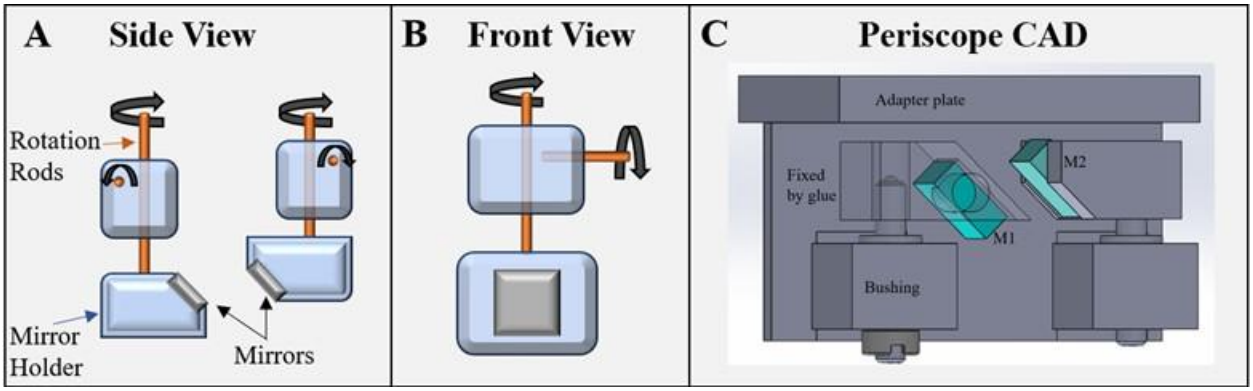

Figure 4.3: Compact periscope design. Panels A and B illustrate a side and front view schematic of the periscope design, showcasing the aluminum mirror holder with a padded screw securing the mirror at approximately a 45º angle. A rod is attached to the mirror holder, extending vertically and connected to another aluminum block. The aluminum block features a horizontally protruding rod. Both rods are mounted in bushings, allowing for rotational freedom of the mirror holder. Panel C displays a SolidWorks computer-aided design (CAD) image, featuring the labeled adapter plate for attachment to the rotational stage.

4.3.4 Mitigating Mirror Rotation Polarization Effects

As discussed in section 4.3.2, the inclusion of a quarter waveplate between the periscope and focal lens was necessary. Prior to the introduction of the periscope, the sample arm had a linearly and horizontally polarized beam for incidence on the sample (Figure 4.4, 'Before Galvo' and 'After Galvo'). However, the presence of the silver mirrors in the periscope altered the polarization, resulting in an elliptical polarization state. The degree of ellipticity was dependent on the directional position of the periscope but given the significant reliance of our measurements on polarization, it was crucial to achieve a polarization state as close to linear as possible for incidence on the sample. A simulation was performed to determine the optimal position for the quarter waveplate and aimed to minimize the impact of the ellipticity. We considered 0° to be the position of the pole on the optics table holding the galvos and cage system mounting clamps. The optimal position for the quarter waveplate was 13° counterclockwise from that position. In Figure 4.4, we assess the percentage ellipticity in the sample arm at 12 periscope positions. Without the quarter waveplate, multiple periscope positions had ellipticity higher than 20%. The addition of the quarter waveplate greatly mitigates the ellipticity introduced by the pericope mirrors, lowering the percentage to below 10% across all twelve periscope positions.

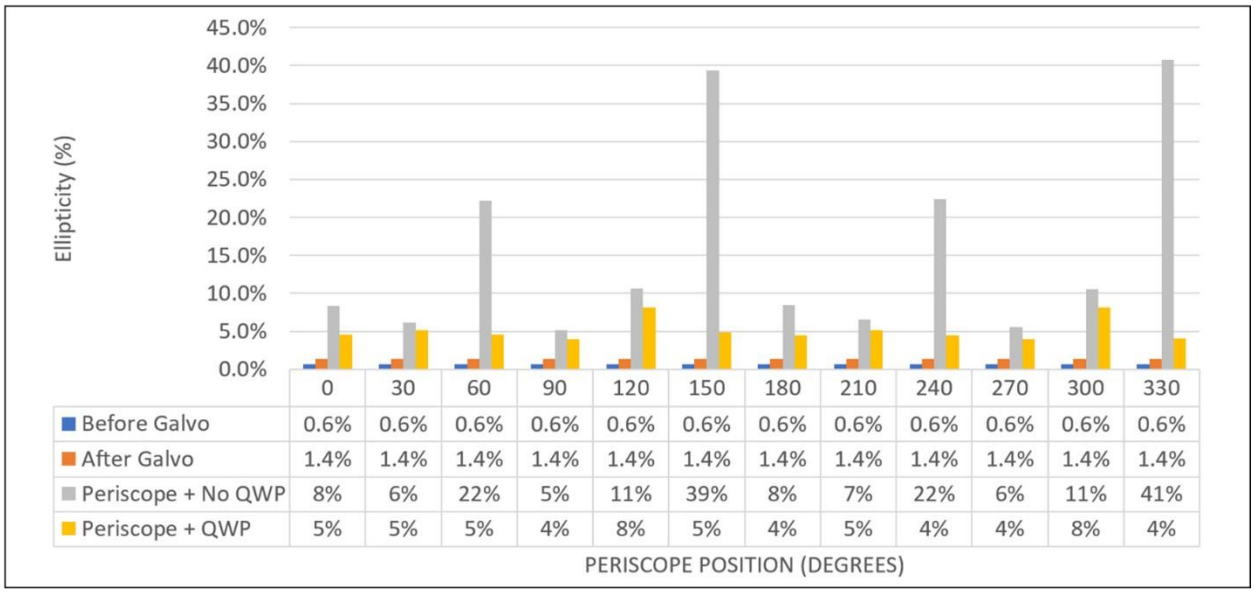

	0	30	60	90	120	150	180	210	240	270	300	330
Before Galvo	0.6%	0.6%	0.6%	0.6%	0.6%	0.6%	0.6%	0.6%	0.6%	0.6%	0.6%	0.6%
After Galvo	1.4%	1.4%	1.4%	1.4%	1.4%	1.4%	1.4%	1.4%	1.4%	1.4%	1.4%	1.4%
Periscope + No QWP	8%	6%	22%	5%	11%	39%	8%	7%	22%	6%	11%	41%
Periscope + QWP	5%	5%	5%	4%	8%	5%	4%	5%	4%	4%	8%	4%

Figure 4.4: Sample arm incident beam ellipticity at different periscope directional positions 30º apart from 0-360 degrees. The beam is initially linear before and after the galvanometer mirrors. Without a quarter waveplate added after the periscope, a significant variation in ellipticity is observed across periscope

positions, ranging from 5% to 40%. However, upon the addition of the quarter waveplate, the ellipticity is minimized, consistently remaining below 10%.

4.4 Validation of Diffusion Coefficients Dependence on Concentration

4.4.1 Sample Preparation and Experimental Procedure

Agarose gels were created from low gelling temperature agarose powder (Sigma Aldrich). A 3 wt% stock solution was created by diluting agarose with distilled water according to the protocol provided. From the stock solution, 400 μL samples were created at concentrations ranging from 0.5 wt% - 2.75 wt% by warming up agarose in an 80°C water bath for 15 minutes, diluting with distilled water, and mixing in GNRs (70 × 22 nm) for a number density of 6.8×10^7 GNRs/μL. Agarose gels were cooled to room temperature over the course of 30 minutes before imaging commenced.

Collagen samples were prepared using 4 mg/mL rat tail collagen I (Corning, Tewksbury, MA). Two stock solutions were created at concentrations 1 mg/mL and 2 mg/mL. Collagen was neutralized by adding 0.02 mL 1N NaOH for each mL of collagen used in the stock. Diluted phosphate buffered saline was added to be 10% of the stock volume, and ice-cold deionized water was added to dilute the sample to a volume of 1 mL. A volume of 400 μL of each sample was mixed with GNRs (70 × 22 nm), for a number density of 6.8×10^7 GNRs/μL and pipetted onto individual petri dishes. The samples were incubated at 37°C in a high-humidity atmosphere containing 5% CO_2 for two hours. After incubation, samples were allowed to warm to room temperature over the course of 30 minutes before imaging commenced.

For each agarose gel and collagen gel sample, 12 M-Mode images comprised of 10,000 A-lines each were collected sequentially at a line rate of 62.5 kHz. Each M-Mode was collected from a unique periscope position, with all 12 positions being 30° apart. Samples were imaged in two locations to have spatially averaged results.

4.4.2 System Calibration

Although the polarization effects of the silver mirrors were greatly mitigated by the introduction of a quarter wave plate, there were still some effects observed in our results. For an isotropic sample, we expect the diffusion coefficients to be the same across all periscope directional positions. However, the

results did not match this expectation when assessing samples comprised of water, agarose gel, or collagen gel. In the translational diffusion coefficients, we noticed a repeatable trend in the diffusion versus periscope directional position over all experiments. Diffusion is calculated to be fastest at positions 0° and 180° and slowest at positions 90° and 270°. We attribute this trend to the small amount of elliptical polarization that we could not correct for. Given that this trend is apparent and consistent across all sample types, we can establish calibration factors for correcting the result at each position.

We typically collect data from 3 transverse spatially separate locations to calculate our calibration factors. We average the translational diffusion across all periscope positions for each location and then divide each periscope position's diffusion by the average diffusion. The fractional values are averaged across all locations to define a final calibration value for each periscope directional position. This process was completed in four separate experiments on three separate days and the calibration values remain the same with a small standard error (Fig 4.6).

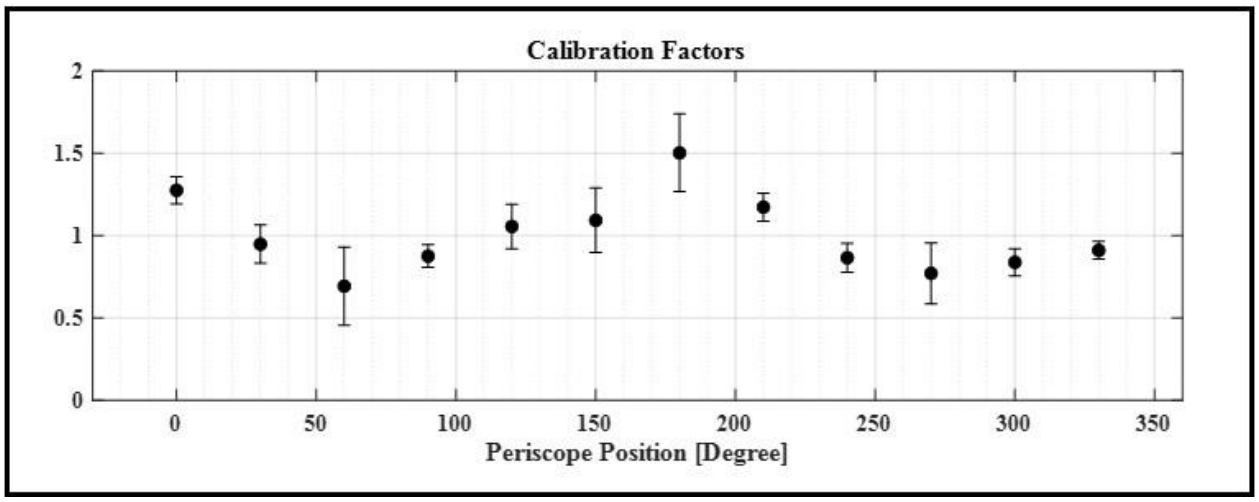

Figure 4.5: Average calibration factors for each periscope position. A calibration factor is the ratio of the periscope angular position's DT value divided by the average DT value of all periscope angular positions. To calculate the average calibration factor (y-axis), we average calibration factors from multiple samples and multiple locations within each sample

4.4.3 Results and Discussion

The objective of this validation experiment was to investigate the performance of our diffusion tensor hardware in measuring translational diffusion in isotropic samples. To be deemed validated, the experimental results should first show that measurements in a single sample are independent of periscope

position. Second, the measurements of multiple samples, of varying concentrations, should result in a diffusion rate with dependence on concentration, just as we observed in our Chapter 3 DS-OCT results. For these experiments, the final translational diffusion values were obtained by averaging measurements from all periscope positions. Figure 4.6A displays the results of translational diffusion in agarose gels, comparing them with the values reported in section 3.4 of this dissertation. Our DT-OCT measurements exhibit a small standard error (SE < 1 μm/s), indicating low variability across periscope positions, and demonstrate good agreement with the quantified values obtained from DS-OCT. In the collagen experiments (Figure 4.6B), the DT-OCT results are displayed alongside previously published collagen gel DS-OCT results [59]. The obtained results show a concentration dependent trend consistent with the previous findings. The standard error of the DT measurements in collagen is also small (SE < 0.3 μm/s), further indicating the reliability and precision of our diffusion tensor hardware.

Based on these results, our diffusion tensor hardware effectively measures D_T in isotropic samples. The measurements, after correction by a calibration factor, are found to be independent of periscope position and exhibit a clear dependence on sample concentration. The consistency of DT-OCT measurements across different periscope positions demonstrates the robustness of our hardware setup. Overall, these findings validate the accuracy and reliability of our diffusion tensor hardware for measuring translational diffusion in two different isotropic samples. These findings provide a promising perspective on the measurement of angle-dependent properties due to the low standard error of ≤ 0.2 in the measurements. This suggests that our measurement method holds the potential to detect even subtle instances of anisotropy, as small as $R = 2$.

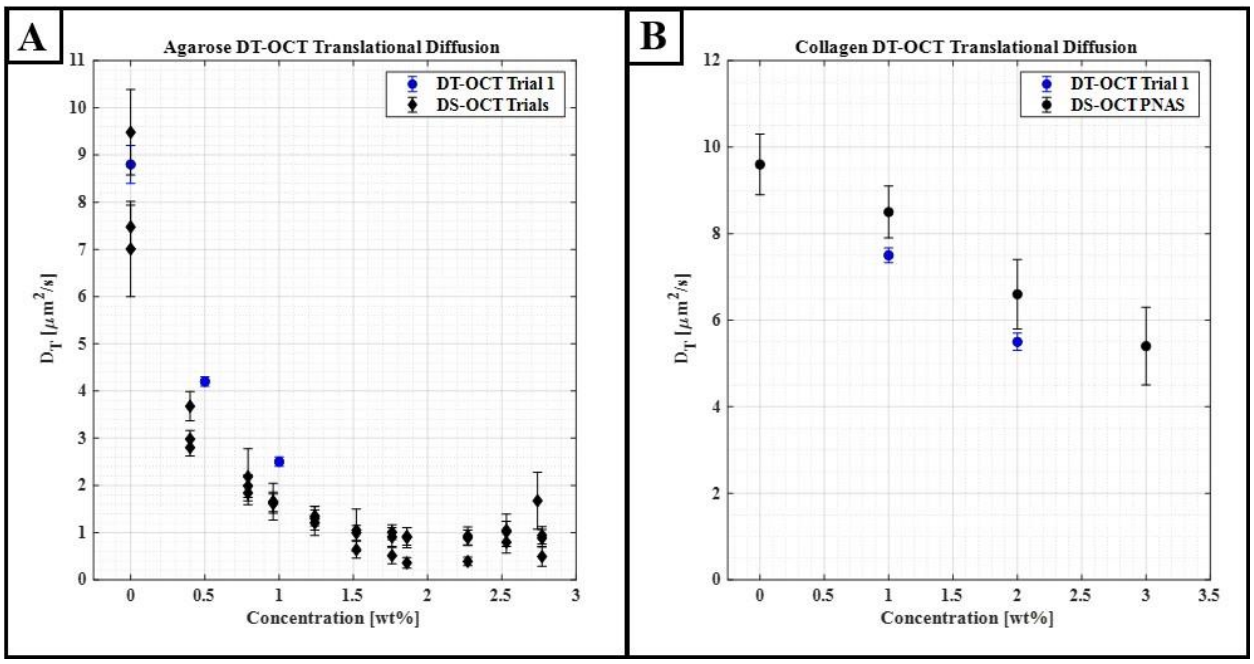

Figure 4.6: Gold nanorod translational diffusion in agarose and collagen gels. In panel A, D_T is plotted as a function of agarose solids concentration. Data collected with DT-OCT hardware is compared to our DS-OCT results presented in Chapter 3. In panel B, D_T is plotted as a function of collagen solids concentration. Data collected with DT-OCT hardware is compared to results published in [59]. Zero concentration represents GNR diffusion in solvent (distilled water). Error bars may not be visible due to small standard deviation size.

4.5 Conclusions

In conclusion, the anisotropy of the meshwork of tissue or biopolymers at a cellular scale has potential to be assessed through the application of the Diffusion Tensor OCT (DT-OCT) technique. This chapter provided a hardware design for the DT-OCT system and addressed design constraints and parameters, highlighting the need for a custom periscope. Although the periscope mirrors introduced polarization effects, we were able to mitigate them effectively with a quarter waveplate. Through experiments with agarose gels and collagen samples, we validated the hardware by showing translational diffusion measurements in isotropic samples are independent of the periscope position and dependent on sample concentration. Overall, the findings imply that DT-OCT hardware is promising for characterizing anisotropy in biopolymers, offering a foundation for non-destructive experiments investigating nanostructure. We additionally note that advanced imaging techniques for nanostructure assessment can be additionally valuable for a variety of biomaterials outside of pulmonary mucus. For instance, tissue

engineers are particularly interested in characterizing the nanostructure of biomimetic scaffolds, as it provides mechanical cues for cellular behavior and function [24]. Monitoring alterations in pore size, which occur when the nanostructure of the extracellular matrix (ECM) is remodeled during disease progression or regression [20, 21], can aid in tracking treatment efficacy [27]. Future studies should aim to create a suitable anisotropic control to validate the DT-OCT technique and confirm its applicability.

CHAPTER FIVE
CONCLUSIONS

5.1 Thesis Contributions Conclusions

In this dissertation, the use of optical coherence tomography (OCT) to develop assessment tools for studying the properties of pulmonary mucus at both bulk and nanoscopic levels is explored. In Chapter 2, the micro-parallel plate strain induction chamber (MPPSIC) is introduced as a valuable tool for conducting particle tracking experiments in Newtonian and non-Newtonian fluids with OCT. Sinusoidal shear experiments conducted using the MPPSIC in Newtonian fluid demonstrate its functionality and ability to provide depth-dependent velocity profiles consistent with theoretical expectations. When applied to mucus, the MPPSIC shows promise in assessing shear-dependent properties of biofluids, particularly at shear rates relevant to the lung epithelium. However, it is suggested that larger shear amplitudes may be needed to measure non-linear responses in mucus. The observations also reveal that under certain plate separation conditions, such as within the gap-loading limit, the velocity amplitude profiles of mucus resemble those of a Newtonian fluid, even though mucus is generally non-Newtonian.

In Chapter 3, a method utilizing translational and rotational diffusion rates of gold nanorods (GNRs) is introduced as an *in situ* assay for mucus hydration levels. The diffusion rates of GNRs are quantified in three mucus mimetic biopolymers polyethylene oxide solutions, agarose gels, and hyaluronic acid, showing that rotational diffusion is less hindered than translational diffusion in all four biopolymers at strongly confining concentrations. This effect is then observed in human bronchial epithelial (hBE) mucus samples, where rotational diffusion measurements expand the dynamic range of sample concentrations and enable the study of dehydrated mucus concentrations. By measuring diffusion rates in stationary mucus samples and fitting a model based on translational and rotational diffusion, we showed the percentage weight concentration of mucus can be estimated. The application of this model to an hBE

cell culture treated with HTS demonstrates that rotational diffusion can provide information on mucus hydration levels up to 6.4 wt%. This enhanced sensitivity enables the development of a real-time assay for in situ assessment of mucus hydration, with potential applications in therapeutic treatment monitoring and further biomedical research. The measurement of both translational and rotational diffusion of GNRs holds promise for various biomedical research areas and offers a means to estimate mucus hydration levels and monitor therapeutic treatments.

In Chapter 4, we proposed a new hardware design with potential for sensing nanopore size anisotropy, which is relevant to tracking disease progression or therapeutic treatments. Diffusion Tensor OCT (DT-OCT) holds potential for assessing anisotropy in tissue or biopolymers with cellular level resolution. This chapter presented a hardware design for the DT-OCT system and experimentally validated the dependence of diffusion coefficients on concentration in collagen and agarose gels. The results confirmed the accuracy and reliability of the diffusion tensor hardware in measuring translational diffusion in isotropic samples, regardless of periscope position. Overall, DT-OCT hardware shows promise for the future application of characterizing anisotropy in biopolymers.

5.2 Future Directions

The MPPSIC and custom cross correlation analysis presented in Chapter 2 can be a valuable tool for conducting fluid flow studies on diverse biomaterials. Future research can focus on polymer modeling to help determine the optimal frequency, displacement amplitude, and plate separation distance required to obtain observable viscoelastic responses from biomaterials. Such experiment can begin to quantify the onset of shear thinning in pulmonary mucus and its correlation with beat frequency and concentration. Exploring these relationships, specifically the conditions under which shear thinning occurs in mucus samples, will aid in designing more efficient drug delivery systems and contribute to our knowledge of mucus biomechanics. There is also the possibility of combining GNR diffusion quantification experiments with fluid flow experiments in the MPPSIC, utilizing the same sample volume to perform multiple experiments sequentially. This integrated approach can further enrich our understanding of fluid flow and concentration dependencies.

We investigated the applicability of GNR translational and rotational diffusion measurements in five biomaterials as well as during an hBEC culture hydration study. Based on the 6.4 wt% data results, we successfully demonstrated that rotational diffusion quantification can expand the dynamic range of concentration dependence for GNR translational and rotational diffusion. To further enhance these findings, future studies can extend this concentration range to include more dehydrated levels well past 6.4 wt%. Furthermore, our investigations can be advanced by delving into the heterogeneity observed in high wt% samples. By refining the regions of interest in our analysis, we have the potential to assess the heterogenous nature of dehydrated pulmonary mucus samples more accurately. Additionally, our research highlights the potential of GNR diffusion as a hydration assay. Applying this assay to more HBEC culture experiments can offer valuable insights. By exploring different percentages of hypertonic and isotonic saline solutions, we can gain a deeper understanding of hydration dynamics and the persistence of mucus hydration at various depths.

Lastly, in order to evaluate the performance of the diffusion tensor hardware it is necessary to construct an anisotropic sample with an ideal fibrous structure. Generating such a sample presents a challenge, making it an intriguing prospect for future research focused on the detection of anisotropy in biomaterials. It should be noted that a challenge arises in finding a controlled phantom with a known structural anisotropy to validate the implementation of DT-OCT. Numerous techniques have been explored for creating structurally anisotropic hydrogels and scaffolds. These techniques include directional freeze-casting [103], magnetic fields [66, 67], electrospinning [68, 69], mechanical force [70 – 73], and 3D bioprinting [112]. However, all these methods require specialized instrumentation that may not be readily available. Moreover, freeze-casting and electrospinning impose limitations on the use of the biomaterial because the fabrication conditions can be too harsh. A recent promising approach creates alignment in collagen by applying strain [57]. The authors add collagen to a pre-strained polydimethylsiloxane (PDMS) mold prior to the complete collagen self-assembly to generate homogeneous alignment of the fibrils. As commercially available structurally anisotropic samples that accurately represent the nanostructure size of

pulmonary mucus are lacking, the recreation of this phantom could serve as a valuable control for validating the developed DT-OCT hardware.

Once the DT-OCT hardware is confirmed through validation with a controlled anisotropic sample, numerous potential studies open up through this method. One such avenue involves assessing the anisotropy of nanopores in the ECM during experiments investigating the impact of toxins or cancer treatment. By examining the anisotropic properties of these nanopores, it becomes possible to observe how cells respond and remodel during disease treatment. Furthermore, tissue engineers hold a keen interest in exploring the nanostructure of their engineered scaffolds using this technology. In the future, this technique can be utilized to evaluate a wide range of biomaterials and play a crucial role in informing drug delivery designs for various diseases, not limited to respiratory diseases.

APPENDIX A

MPPSIC USE PROTOCOL

1.) Turn on the three axis nanopositioner's power supply and the power supply above the 3-axis power supply. The top power supply changes the spacing between plates. Every 1 V = an additional 10 um. Set this to zero initially and make sure the output is on.

2.) Unscrew the four screws holding the bridge plate (the top microscope slide holder). Add your sample. Put the top plate back on.

3.) Put the MPPSIC underneath the focal lens and position using the large Z-axis translational stage.

4.) In OCT 1.5 (LabView), click the MPPR tab (top left panel of Figure A1).

5.) The 'MMOCT Mode' will change which waveform is output from the DAQ. 'Placeholder 3' will output a pulse function with amplitude 'Max Voltage' and frequency based on 'Images per Cycle'. The frequency will be calculated in the 'Frequency' bar based on your chosen imaging parameters. 'Placeholder 4' will output a sinusoidal function.

6.) Before image acquisition, ensure BNC cables from the brown power supply are connected to the "z" axis of the 3-axis nanopositioner power supply. If the DAQ is connected to the "x" axis position, the MPPSIC will strain the sample in the y imaging axis. The "y" axis will strain the sample in the x imaging axis.

7.) Acquire images.

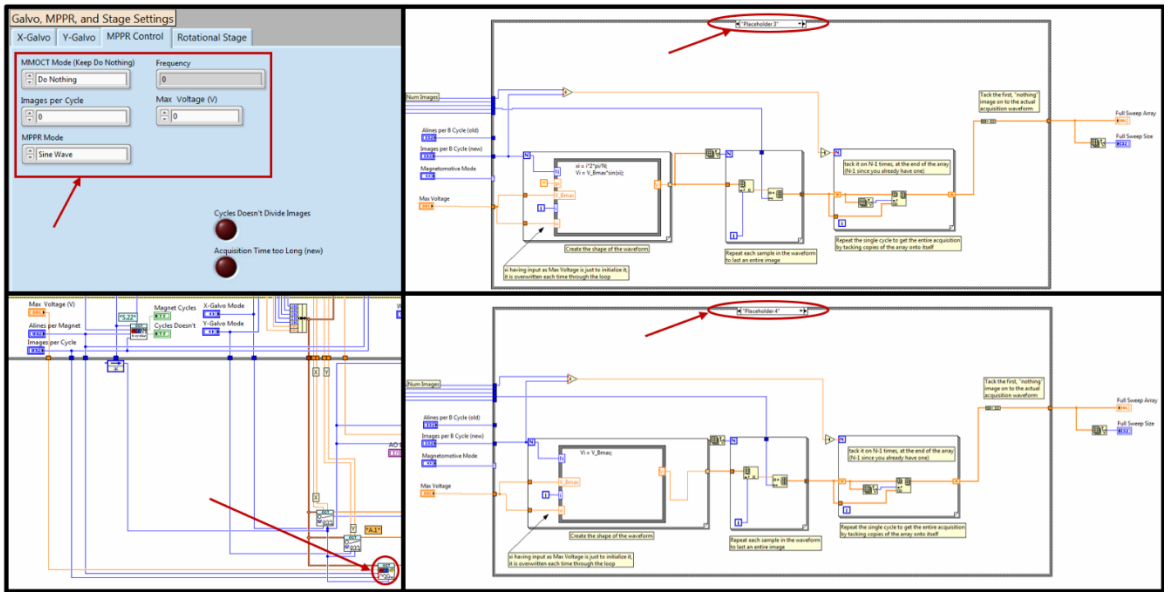

Figure A1: MPPSIC Control in LabView

APPENDIX B

MPPSIC CUSTOM PARTICLE TRACKING VELOCIMETRY CODE DECIMATION TECHNIQUE

In this appendix, we provide a more detailed explanation of the tilt adjustment method and decimation techniques used in the image analysis algorithm described in Chapter 2.

B.1 Tilt Adjustment Method

For the tilt adjustment method, the user initially marks approximate locations of the top and bottom surfaces of the fluid. For each surface, a line is extrapolated through the user-defined points, then a 10-pixel vertical window searched to locate pixels in each column with maximum intensity. Then, new lines are fit through the intensity maxima, which are used to define the top and bottom of the sample region as well as the angles of the top and bottom plates relative to horizontal. The tilt angle of each plate from a horizontal position is calculated. To check how parallel the plates are, we assess the difference of the two plate tilt angles. The separation distance H between the top and bottom surfaces is measured at the center of the image. Distortion, D_{axial} and $D_{\text{transverse,}}$ is accounted for in the height calculation. The surfaces are only segmented for one frame in each stack as there is negligible movement of the plates between frames.

B.2 Decimation Technique

Decimation is used to exaggerate motion in regions of low velocity, such as near the top plate, where displacements between successive frames can be less than a single pixel.

B.2.1 Constant Velocity

Frames corresponding to turn around points in velocity (velocity extrema) are identified by an initial sweep of x_{shift} (using Eqn. (2.5)) over successive frames of an ROI in the bottom row ($\text{ROI}_{N,j}$) and by subsequently plotting the cumulative displacement. The chosen number of 2 frames padding the extrema was based on the mechanical turn-around time of the nano-positioner.

Because we expect the velocity to decrease linearly between the bottom and top plates, we determine a row (i) dependent decimation value, Δk_i, based upon an initial estimate of the velocity within that row, v_{i} (in pixels / frame). Initial velocity is computed by linear regression of the depth and velocity of the bottom

$ROI_{N,j}$ and the top of the sample region, where we expect a velocity of zero. To target a displacement of at least 3 pixels, we define Δk_i as $\frac{3}{V_i}$ or 1, whichever is larger. In high velocity regions Δk_i will equal 1 (no decimation) and displacements will typically be much larger than 3 pixels. In very low velocity regions, if Δk_i is larger than F, the number of frames in one sweep, it is set to F-1 to enable at least one measurement per sweep.

B.2.2 Sinusoidal Velocity

We define frame decimation vector as:

$$\Delta k(k)_i = \frac{x_{ideal}}{x_{theo}(k)_i}, \quad \text{(S1)}$$

where $x_{\text{shift}}(k)_i$ is the theoretical pixel displacements over frames k in $ROI_{i,j}$. The maximum frame decimation number is capped at a user defined number based on a maximum phase angle of the waveform to search over: $\theta_{max} = \frac{2\pi}{10}$, so that the velocity is not changing significantly over the decimation range.

Note that the velocity of a time point must be calculated as the average velocity between two equally distant frames. We perform normalized cross correlations using the decimation frame pairs of each row and store the x_{shift} values in a master ($N \times M \times Q$) matrix. The velocity is calculated by dividing each x_{shift} by total number of frames between the two time points.

$$U(k)_{i,j} = \frac{x_{shift}(k)_{i,j}}{1 + 2 * \Delta k(k)_{i,j}}. \quad \text{(S2)}$$

The outcome velocities have units of pixels per frame. The results of the decimation technique are displayed in Figure S1.

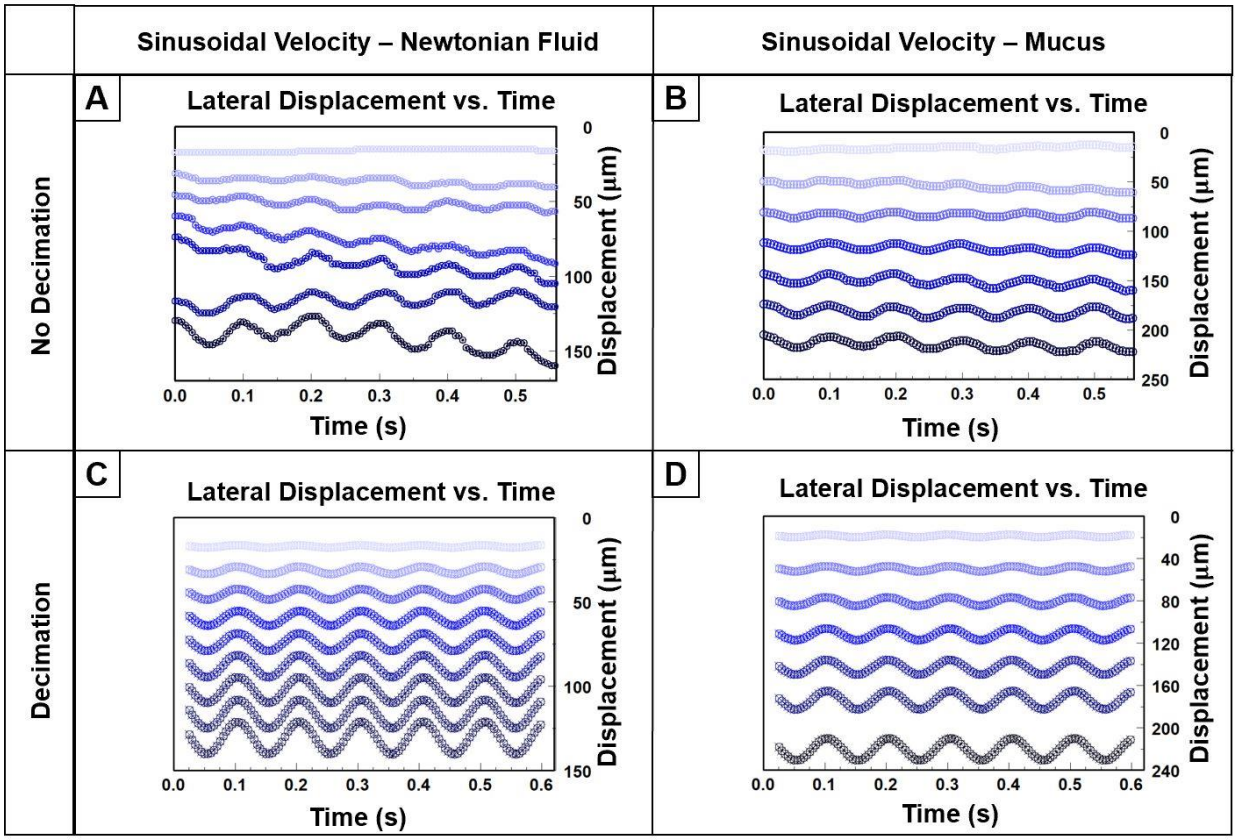

Figure B1: (a) Pre-decimation traces of lateral particle displacements in a Newtonian sample driven by a sinusoidal waveform. (b) Pre- decimation traces of lateral particle displacements in a mucus sample driven by a sinusoidal waveform. **:** (c) Post-decimation traces of lateral particle displacements in a Newtonian sample driven by a sinusoidal waveform. (d) Post-decimation traces of lateral particle displacements in a mucus sample driven by a sinusoidal waveform. Traces are shown at multiple depths in the sample, offset by their depth position for clarity (5 of 6 waveforms shown). For visual purposes, not all ROI depths were plotted.

APPENDIX C

DT-OCT ALIGNMENT PROTOCOL

To begin at this point, the DT-OCT should be set up but swung out of the way of the sample arm. If you need to start from scratch alignment, perform step 1-4 and then refer to second set of steps in this appendix.

1.) Remove the 30 mm focal lens from the sample arm.

2.) Ensure the galvos are reflecting straight down onto the optics table. Make an offset if need-be: X: 0.19 Y:0.04. Make sure both galvos scan 'within'.

3.) Note the position of the lens in the DT-OCT system lens holder. Take note that the Thor Labs label is face up, and how far it is screwed in. This will help you with adjusting the reference arm later.

4.) Move the reference arm to the end of the track. Leave a bit of room to be able to adjust both translational arms.

5.) Take the lens out of the DT-OCT system.

6.) Use LabView "DT-OCT 1.7", click acquisition set-up, click rotational stage (by galvo settings), and HOME the rotational stage.

7.) Swing the DT-OCT system into the beam path. The black clamp should line up with the galvo's black clamp.

8.) Before locking in the black clamp, look at the sticker on the optics table. Make sure the beam is not clipped. Remember the beam is bouncing through a periscope, so it will not hit the center mark. It should be roughly 4mm from the center mark. If the user is facing the interferometer from the bench side of the room, the beam will land on the mark closest to them. (In the X galvo direction, away from the interferometer). Lock the clamp into place.

9.) Block the reference beam. Set X galvo scan to 0.8mm. Check the power into HH and HV channels with the Lambertian phantom. They will not have equal power at all periscope positions but try to get a good amount in at least 6 unique angles. Please don't try looking at

the beaded phantom – the working distance is too short to reach the sample deep in the dish. Note: you can set relative step size to any degrees – such as type 30 degrees and then click set step size – and then manually click MOVE RELATIVE STEP SIZE ***not*** jog.

10.) Unblock the reference arm and block the sample arm. Adjust the retroreflector as needed.

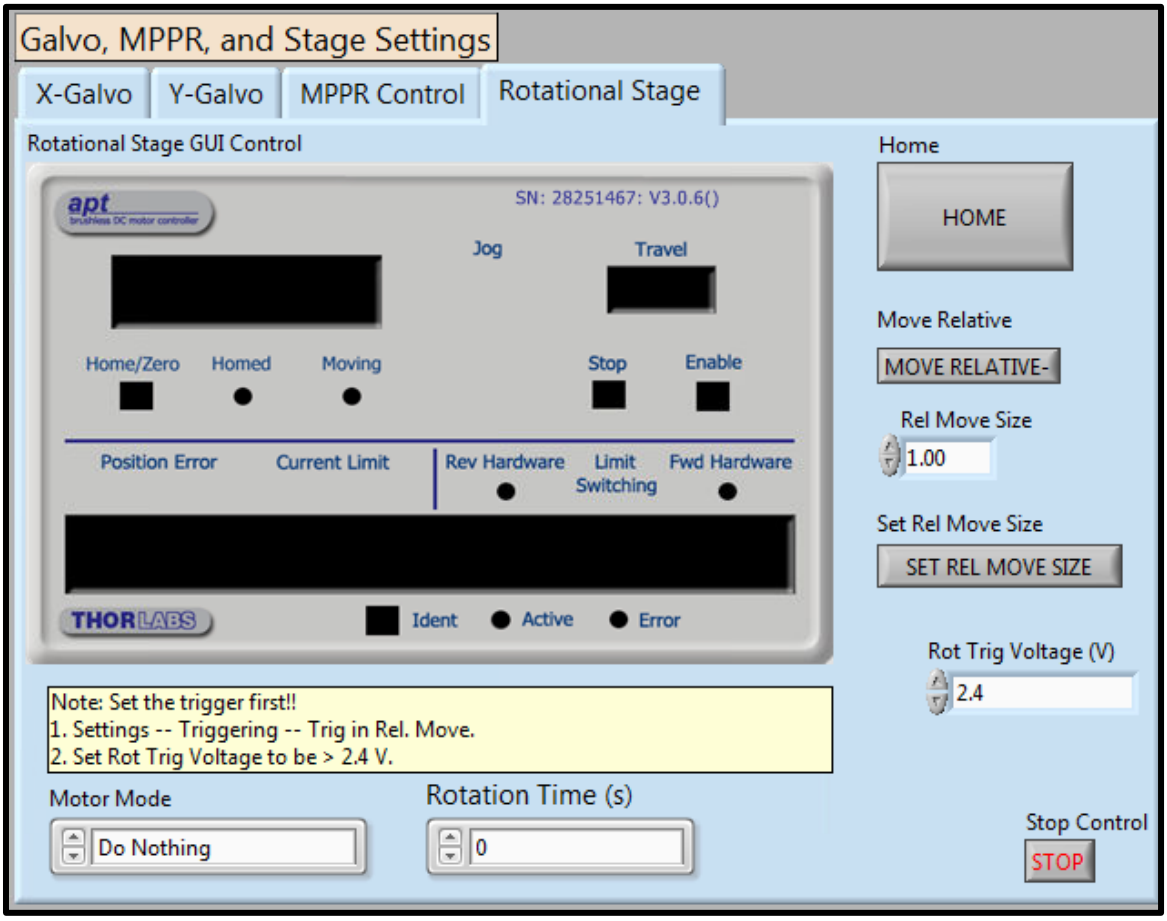

Figure C1: LabView motorized rotational stage GUI for DT-OCT hardware control.

To begin at this point, the set-up should have the rotational stage at the top of the cage system and the lens holder (NON-KINEMATIC) at the bottom of the four-rod cage system.

1. Ensure the galvos are reflecting straight down onto the optics table. Make an offset if need-be: X: 0.19 Y:0.04

2. Lower the system slightly away from the galvo mirrors (use the middle black clamp to the large pole holding the entire DT-OCT setup – do NOT touch the top black clamp that holds the galvos). Add an iris to the top of the rotational stage and an iris to the bottom of the lens holder.
3. Set up the beam profiler to adjust rotational stage position in x and y plane (use as a power meter and beam profiler).
4. Once the rotational stage iris (THE TOP IRIS) is aligned in x and y, adjust the tilt of the rotational stage in y. Then adjust for tilt in x. Do this by partially closing the top iris and then closing and opening the bottom iris to correct for tilt.
5. Now we need to move the system up toward the galvos - take out the top iris to do that. Use the bottom iris (partially closed) to realign the swing of the cage system while moving DT-OCT's clamp up the pole to be flush with the galvo clamp.
6. Put in the quarter wave plate and take out the bottom iris.
7. Put in the periscope. You will need to align the periscope such that the circling beam does not converge or diverge. Go to the rotational stage GUI in LabView. Click settings, and set to continuous motion (press-release). Click the jog button. This should make the rotational stage circle continuously, giving an easier visual assessment. The circle should be centered around the beam's original path (where the beam hits when the periscope is not in the system's alignment redirecting it). The periscope mirrors have a gap of 4 mm apart. Check that the circle maintains an 8mm diameter all the way down to the optics table.
8. Put in lens (Thorlabs label facing up).
9. Use the Lambertian phantom to set the reference arm position (may need to move the retroreflector back on its track).
10. Align HH and HV Channels to equalize signal at all periscope positions as much as possible.
11. Swap out the Lambertian for a sample.

APPENDIX D

DT-OCT USE PROTOCOL

The version of LabView that runs DT-OCT is 1.7. The rotational stage control is currently set up to the DAQ's channel 4 output. The rotational stage is on top of the main OCT system to the left of the GALVO power supply. Make sure it is turned on.

DT-OCT is very similar to running DS-OCT. However, we do not scan in any direction – purely M-Modes are taken.

1.) Set line rate to 25 kHz and ALines to 1000. Set X scan to 0.8mm. This is the easiest setting to set up your sample.
2.) Set up line rate to 62.5kHz and keep A-Lines at 1000. Adjust reference power as needed.
3.) If your sample is in a good position, let's return to M-mode settings. Set A-Lines to 10000. Set X scan to 0 mm. Take 1 reference image.
4.) Go to acquisition settings and click rotational stage. Home the stage. Set Trigger mode on. Set the number of images to 12.
5.) Acquire data – the first round takes a minute to load up, so don't let the lag worry you.
6.) Please check the rotational stage GUI for the periscope position. It should always end on 30 degrees. Sometimes it does not. You should HOME the stage and then retake the data.
7.) Use step 2 to move to a new location if you want to take data in a new spot of the sample and then 3-6. Always remember to HOME the stage before taking new image sets.

Troubleshooting:

1.) The rotational stage will bug out on LabView occasionally. Turn off and click out of LabView completely. Power down the rotational stage. Wait 1 minute. Turn it back on. Restart LabView. Do not touch any rotational stage buttons until the GUI lights up with the periscope position.

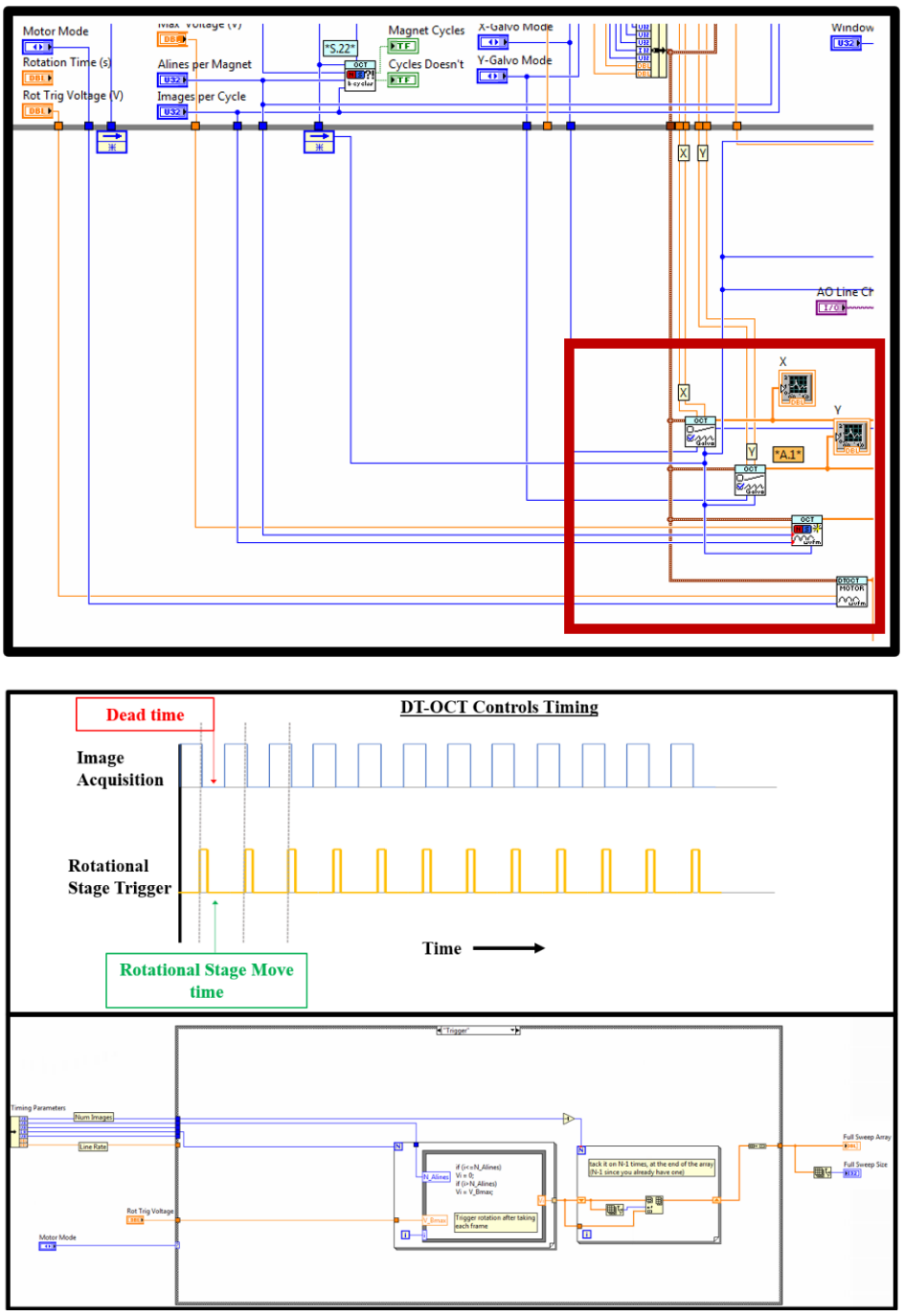

Figure D1: The image acquisition and rotational stage trigger timing. The LabView node controls the output similar to how MMOCT is triggered in the original LabView OCT version.

REFERENCES

[1] R. C. Boucher, “Muco-Obstructive Lung Diseases,” *N. Engl. J. Med.*, vol. 380, no. 20, pp. 1941–1953, May 2019, doi: 10.1056/NEJMra1813799.

[2] X. M. Bustamante-Marin and L. E. Ostrowski, “Cilia and Mucociliary Clearance,” *Cold Spring Harb. Perspect. Biol.*, vol. 9, no. 4, p. a028241, Apr. 2017, doi: 10.1101/cshperspect.a028241.

[3] B. Button *et al.*, “A periciliary brush promotes the lung health by separating the mucus layer from airway epithelia,” *Science*, vol. 337, no. 6097, pp. 937–941, Aug. 2012, doi: 10.1126/science.1223012.

[4] D. B. Hill, B. Button, Michael Rubinstein, and R. C. Boucher, “Physiology and Pathophysiology of Human Airway Mucus,” *Physiol. Rev.*, Jan. 2022, doi: 10.1152/physrev.00004.2021.

[5] B. Button, W. H. Anderson, and R. C. Boucher, “Mucus Hyperconcentration as a Unifying Aspect of the Chronic Bronchitic Phenotype,” vol. 13, 2016.

[6] A. S. Verkman, Y. Song, and J. R. Thiagarajah, “invited review Role of airway surface liquid and submucosal glands in cystic fibrosis lung disease,” 2003, doi: 10.1152/ajpcell.00417.

[7] M. E. Shapiro, T. E. Corcoran, C. A. Bertrand, F. Serrano Castillo, and R. S. Parker, “Physiologically-Based Model of Fluid Absorption and Mucociliary Clearance in Cystic Fibrosis,” Elsevier B.V., Jan. 2018, pp. 102–103. doi: 10.1016/j.ifacol.2018.09.023.

[8] S. Girod, J.-M. Zahm, C. Plotkowski, G. Beck, and E. Puchelle, “Role of the physicochemical properties of mucus in the protection of the respiratory epithelium,” *Eur Respir J*, vol. 5, pp. 477–487, 1992.

[9] D. J. Thornton, K. Rousseau, and M. A. McGuckin, “Structure and function of the polymeric mucins in airways mucus,” *Annu. Rev. Physiol.*, vol. 70, pp. 459–486, 2008, doi: 10.1146/annurev.physiol.70.113006.100702.

[10] S. H. Randell and R. C. Boucher, “Effective mucus clearance is essential for respiratory health,” *Am. J. Respir. Cell Mol. Biol.*, vol. 35, no. 1, pp. 20–28, Jul. 2006, doi: 10.1165/rcmb.2006-0082SF.

[11] A. E. Tilley, M. S. Walters, R. Shaykhiev, and R. G. Crystal, “Cilia dysfunction in lung disease,” *Annu. Rev. Physiol.*, vol. 77, pp. 379–406, Feb. 2015, doi: 10.1146/annurev-physiol-021014-071931.

[12] W. H. Anderson *et al.*, “The relationship of mucus concentration (hydration) to mucus osmotic pressure and transport in chronic bronchitis,” *Am. J. Respir. Crit. Care Med.*, vol. 192, no. 2, pp. 182–190, Jul. 2015, doi: 10.1164/rccm.201412-2230OC.

[13] “About Cystic Fibrosis | Cystic Fibrosis Foundation.” https://www.cff.org/intro-cf/about-cystic-fibrosis (accessed Jul. 04, 2023).

[14] R. C. Stern, “The Diagnosis of Cystic Fibrosis,” *N. Engl. J. Med.*, 1997.

[15] J. Q. Xu, S. L. Murphy, K. D. Kochanek, and E. Arias, “Mortality in the United States, 2018. NCHS data brief, no 355,” *Natl. Cent. Health Stat. Hyattsville MD*, 2020.

[16] B. A. Forey, A. J. Thornton, and P. N. Lee, “Systematic review with meta-analysis of the epidemiological evidence relating smoking to COPD, chronic bronchitis and emphysema,” *BMC Pulm. Med.*, vol. 11, no. 1, p. 36, Dec. 2011, doi: 10.1186/1471-2466-11-36.

[17] C. Barros, B. Argüello, A. Jedlicki, P. Vigil, and E. Herrera, “Scanning electron microscope study of human cervical mucus,” *Gamete Res.*, vol. 12, no. 1, pp. 85–89, 1985.

[18] R. S. Crowther, D. R. Hughes, and C. Marriott, “Mucus glycoprotein gels: a scanning electron microscopy study of the effect of cations,” *Micron Microsc. Acta*, vol. 15, no. 1, pp. 37–45, 1984.

[19] M. Menárguez, L. M. Pastor, and E. Odeblad, “Morphological characterization of different human cervical mucus types using light and scanning electron microscopy,” *Hum. Reprod.*, vol. 18, no. 9, pp. 1782–1789, 2003.

[20] E. Meziu, M. Koch, J. Fleddermann, K. Schwarzkopf, M. Schneider, and A. Kraegeloh, “Visualization of the structure of native human pulmonary mucus,” *Int. J. Pharm.*, vol. 597, p. 120238, Mar. 2021, doi: 10.1016/j.ijpharm.2021.120238.

[21] A. G. Ford *et al.*, “Molecular dynamics simulations to explore the structure and rheological properties of normal and hyperconcentrated airway mucus,” *Stud. Appl. Math.*, vol. 147, no. 4, pp. 1369–1387, Nov. 2021, doi: 10.1111/sapm.12433.

[22] B. Vukosavljevic, X. Murgia, K. Schwarzkopf, U. F. Schaefer, C.-M. Lehr, and M. Windbergs, “Tracing molecular and structural changes upon mucolysis with N-acetyl cysteine in human airway mucus,” *Int. J. Pharm.*, vol. 533, no. 2, pp. 373–376, Nov. 2017, doi: 10.1016/j.ijpharm.2017.07.022.

[23] B. H. Bajka, N. M. Rigby, K. L. Cross, A. Macierzanka, and A. R. Mackie, “The influence of small intestinal mucus structure on particle transport ex vivo,” *Colloids Surf. B Biointerfaces*, vol. 135, pp. 73–80, Nov. 2015, doi: 10.1016/j.colsurfb.2015.07.038.

[24] A. L. Oldenburg, R. K. Chhetri, D. B. Hill, and B. Button, “Monitoring airway mucus flow and ciliary activity with optical coherence tomography,” *Biomed. Opt. Express*, vol. 3, no. 9, pp. 1978–1992, 2012.

[25] L. Liu *et al.*, “Method for Quantitative Study of Airway Functional Microanatomy Using Micro-Optical Coherence Tomography,” *PLoS ONE*, vol. 8, no. 1, Jan. 2013, doi: 10.1371/journal.pone.0054473.

[26] S. E. Birket *et al.*, “A Functional Anatomic Defect of the Cystic Fibrosis Airway,” *Am. J. Respir. Crit. Care Med.*, vol. 190, no. 4, pp. 421–432, Aug. 2014, doi: 10.1164/rccm.201404-0670OC.

[27] K. K. Chu *et al.*, “In vivo imaging of airway cilia and mucus clearance with micro-optical coherence tomography,” *Biomed. Opt. Express*, vol. 7, no. 7, p. 2494, Jul. 2016, doi: 10.1364/BOE.7.002494.

[28] A. Buchsbaum *et al.*, “Optical coherence tomography based particle image velocimetry (OCT-PIV) of polymer flows,” *Opt. Lasers Eng.*, vol. 69, pp. 40–48, 2015, doi: 10.1016/j.optlaseng.2015.02.003.

[29] W. Poon, B. R. Kingston, B. Ouyang, W. Ngo, and W. C. W. Chan, “A framework for designing delivery systems,” *Nat. Nanotechnol.*, vol. 15, no. 10, pp. 819–829, Oct. 2020, doi: 10.1038/s41565-020-0759-5.

[30] R. A. Cone, “Barrier properties of mucus,” *Adv. Drug Deliv. Rev.*, vol. 61, no. 2, pp. 75–85, Feb. 2009, doi: 10.1016/j.addr.2008.09.008.

[31] B. E. Tildy and D. F. Rogers, “Therapeutic options for hydrating airway mucus in cystic fibrosis,” *Pharmacology*, vol. 95, no. 3–4, pp. 117–132, May 2015, doi: 10.1159/000377638.

[32] D. H. Scott, B. D. William, Z. L. Kirby, K. R. Michael, T. Robert, and B. C. Richard, “Mucus Clearance and Lung Function in Cystic Fibrosis with Hypertonic Saline,” *N Engl J Med*, vol. 354, pp. 241–250, 2006.

[33] E. P. Reeves *et al.*, “Inhaled hypertonic saline for cystic fibrosis: Reviewing the potential evidence for modulation of neutrophil signalling and function,” *World J. Crit. Care Med.*, vol. 4, no. 3, p. 179, 2015, doi: 10.5492/wjccm.v4.i3.179.

[34] M. A. Mall, “Unplugging mucus in cystic fibrosis and chronic obstructive pulmonary disease,” in *Annals of the American Thoracic Society*, American Thoracic Society, Apr. 2016, pp. S177–S185. doi: 10.1513/AnnalsATS.201509-641KV.

[35] V. L. Yap and M. L. Metersky, “New therapeutic options for noncystic fibrosis bronchiectasis,” *Curr. Opin. Infect. Dis.*, vol. 28, no. 2, pp. 171–176, Apr. 2015, doi: 10.1097/QCO.0000000000000147.

[36] W. Drexler and J. G. Fujimoto, Eds., *Optical Coherence Tomography: Technology and Applications*. Cham: Springer International Publishing, 2015. doi: 10.1007/978-3-319-06419-2.

[37] A. F. Fercher, W. Drexler, C. K. Hitzenberger, and T. Lasser, “Optical coherence tomography—principles and applications”.

[38] T. C. Papanastasiou, G. C. Georgiou, A. N. Alexandrou, B. Raton, L. New, and Y. Washington, “VISCOUS FLUID FLOW,” 2000.

[39] C. M. Liu, “Complete solutions to extended Stokes’ problems,” *Math. Probl. Eng.*, vol. 2008, 2008, doi: 10.1155/2008/754262.

[40] B. S. Lindley, “Linear and Nonlinear Shear Wave Propagation in Viscoelastic Media,” The University of North Carolina at Chapel Hill, United States -- North Carolina, 2008.

[41] P. A. Vasquez, Y. Jin, K. Vuong, D. B. Hill, and M. G. Forest, “A New Twist on Stokes’ Second Problem: Partial Penetration of Nonlinearity in Sheared Viscoelastic Layers.”

[42] N.-S. Cheng, “Formula for the Viscosity of a Glycerol−Water Mixture,” *Ind. Eng. Chem. Res.*, vol. 47, no. 9, pp. 3285–3288, May 2008, doi: 10.1021/ie071349z.

[43] W. Heller, “Remarks on Refractive Index Mixture Rules,” *J. Phys. Chem.*, vol. 69, no. 4, pp. 1123–1129, Apr. 1965, doi: 10.1021/j100888a006.

[44] J. Rheims, J. Köser, and T. Wriedt, “Refractive-index measurements in the near-IR using an Abbe refractometer,” *Meas. Sci. Technol.*, vol. 8, no. 6, pp. 601–605, Jun. 1997, doi: 10.1088/0957-0233/8/6/003.

[45] D. B. Hill and B. Button, “Establishment of respiratory air-liquid interface cultures and their use in studying mucin production, secretion, and function.,” *Methods Mol. Biol.*, vol. 842, pp. 245–258, Jan. 2012, doi: 10.1007/978-1-61779-513-8_15.

[46] J. Barrick, A. Doblas, M. R. Gardner, P. R. Sears, L. E. Ostrowski, and A. L. Oldenburg, “High-speed and high-sensitivity parallel spectral-domain optical coherence tomography using a supercontinuum light source,” *Opt. Lett.*, vol. 41, no. 24, p. 5620, Dec. 2016, doi: 10.1364/ol.41.005620.

[47] V. P. Pandiyan, X. Jiang, A. Maloney-Bertelli, J. A. Kuchenbecker, U. Sharma, and R. Sabesan, “High-speed adaptive optics line-scan OCT for cellular-resolution optoretinography,” *Biomed. Opt. Express*, vol. 11, no. 9, p. 5274, Sep. 2020, doi: 10.1364/BOE.399034.

[48] Y. Chen, S.-W. Huang, A. D. Aguirre, and J. G. Fujimoto, “High-resolution line-scanning optical coherence microscopy,” *Opt. Lett.*, vol. 32, no. 14, p. 1971, Jul. 2007, doi: 10.1364/OL.32.001971.

[49] S. M. Mitran, M. G. Forest, L. Yao, B. Lindley, and D. B. Hill, “Extensions of the Ferry shear wave model for active linear and nonlinear microrheology,” *J. Non-Newton. Fluid Mech.*, vol. 154, no. 2–3, pp. 120–135, Oct. 2008, doi: 10.1016/j.jnnfm.2008.04.002.

[50] V. R. Kohout, C. L. Wardzala, and J. R. Kramer, “Synthesis and biomedical applications of mucin mimic materials,” *Adv. Drug Deliv. Rev.*, vol. 191, p. 114540, Dec. 2022, doi: 10.1016/j.addr.2022.114540.

[51] M. J. Yaszemski, D. J. Trantolo, K.-U. Lewandrowski, V. Hasirci, D. E. Altobelli, and D. L. Wise, *Tissue Engineering And Novel Delivery Systems*. CRC Press, 2003.

[52] G. Kogan, L. Šoltés, R. Stern, and P. Gemeiner, “Hyaluronic acid: a natural biopolymer with a broad range of biomedical and industrial applications,” *Biotechnol. Lett.*, vol. 29, no. 1, pp. 17–25, Dec. 2006, doi: 10.1007/s10529-006-9219-z.

[53] B. F. Rankin, “Method of providing asynthetic mucus in vivo,” Oct. 1973.

[54] B. S. Schuster, J. S. Suk, G. F. Woodworth, and J. Hanes, “Nanoparticle diffusion in respiratory mucus from humans without lung disease,” *Biomaterials*, vol. 34, no. 13, pp. 3439–3446, Apr. 2013, doi: 10.1016/j.biomaterials.2013.01.064.

[55] F. Y. Zhu, Q. Q. Wang, X. S. Zhang, W. Hu, X. Zhao, and H. X. Zhang, “3D nanostructure reconstruction based on the SEM imaging principle, and applications,” *Nanotechnology*, vol. 25, no. 18, May 2014, doi: 10.1088/0957-4484/25/18/185705.

[56] R. Ziel, A. Haus, and A. Tulke, “Quantification of the pore size distribution (porosity profiles) in microfiltration membranes by SEM, TEM and computer image analysis,” *J. Membr. Sci.*, vol. 323, no. 2, pp. 241–246, Oct. 2008, doi: 10.1016/j.memsci.2008.05.057.

[57] S. H. Kim *et al.*, “Anisotropically organized three-dimensional culture platform for reconstruction of a hippocampal neural network,” *Nat. Commun.*, vol. 8, Feb. 2017, doi: 10.1038/ncomms14346.

[58] K. H. Kim, H. Xing, J. M. Zuo, P. Zhang, and H. Wang, “TEM based high resolution and low-dose scanning electron nanodiffraction technique for nanostructure imaging and analysis,” *Micron*, vol. 71, pp. 39–45, Apr. 2015, doi: 10.1016/j.micron.2015.01.002.

[59] R. K. Chhetri *et al.*, “Probing biological nanotopology via diffusion of weakly constrained plasmonic nanorods with optical coherence tomography,” *Proc. Natl. Acad. Sci. U. S. A.*, vol. 111, no. 41, pp. E4289–E4297, Oct. 2014, doi: 10.1073/pnas.1409321111.

[60] F. E. Berger Bioucas *et al.*, “Translational and Rotational Diffusion Coefficients of Gold Nanorods Dispersed in Mixtures of Water and Glycerol by Polarized Dynamic Light Scattering,” *J. Phys. Chem. B*, vol. 123, no. 44, pp. 9491–9502, Nov. 2019, doi: 10.1021/acs.jpcb.9b08274.

[61] R. Nixon-Luke and G. Bryant, “Differential dynamic microscopy to measure the translational diffusion coefficient of nanorods,” *J. Phys. Condens. Matter*, vol. 32, no. 11, 2020, doi: 10.1088/1361-648X/ab5a9c.

[62] M. Molaei, E. Atefi, and J. C. Crocker, “Nanoscale Rheology and Anisotropic Diffusion Using Single Gold Nanorod Probes,” *Phys. Rev. Lett.*, vol. 120, no. 11, Mar. 2018, doi: 10.1103/PhysRevLett.120.118002.

[63] S. Martín-Martín, M. del M. Ramos-Tejada, A. Rubio-Andrés, A. B. Bonhome-Espinosa, Á. V. Delgado, and M. L. Jiménez, “Electro-optical Study of the Anomalous Rotational Diffusion in Polymer Solutions,” *Macromolecules*, 2022, doi: 10.1021/acs.macromol.2c01461.

[64] G. Popescu, A. Dogariu, and R. Rajagopalan, “Spatially resolved microrheology using localized coherence volumes,” *Phys. Rev. E - Stat. Phys. Plasmas Fluids Relat. Interdiscip. Top.*, vol. 65, no. 4, p. 8, 2002, doi: 10.1103/PhysRevE.65.041504.

[65] A. Wax, C. Yang, R. R. Dasari, and M. S. Feld, “Path-length-resolved dynamic light scattering: modeling the transition from single to diffusive scattering,” 2001.

[66] R. K. Chhetri, K. A. Kozek, A. C. Johnston-Peck, J. B. Tracy, and A. L. Oldenburg, “Imaging three-dimensional rotational diffusion of plasmon resonant gold nanorods using polarization-sensitive optical coherence tomography,” *Phys. Rev. E - Stat. Nonlinear Soft Matter Phys.*, vol. 83, no. 4, Apr. 2011, doi: 10.1103/PhysRevE.83.040903.

[67] R. L. Blackmon *et al.*, “Direct monitoring of pulmonary disease treatment biomarkers using plasmonic gold nanorods with diffusion-sensitive OCT,” *Nanoscale*, vol. 9, no. 15, pp. 4907–4917, Apr. 2017, doi: 10.1039/c7nr00376e.

[68] R. L. Blackmon *et al.*, “Imaging Extracellular Matrix Remodeling in Vitro by Diffusion-Sensitive Optical Coherence Tomography,” *Biophys. J.*, vol. 110, no. 8, pp. 1858–1868, Apr. 2016, doi: 10.1016/j.bpj.2016.03.014.

[69] N. Jiang, X. Zhuo, and J. Wang, “Active Plasmonics: Principles, Structures, and Applications,” *Chem. Rev.*, vol. 118, no. 6, pp. 3054–3099, Mar. 2018, doi: 10.1021/acs.chemrev.7b00252.

[70] P. K. Jain, X. Huang, I. H. El-Sayed, and M. A. El-Sayed, “Noble Metals on the Nanoscale: Optical and Photothermal Properties and Some Applications in Imaging, Sensing, Biology, and Medicine,” *Acc. Chem. Res.*, vol. 41, no. 12, pp. 1578–1586, Dec. 2008, doi: 10.1021/ar7002804.

[71] F. J. García De Abajo, “Nonlocal Effects in the Plasmons of Strongly Interacting Nanoparticles, Dimers, and Waveguides,” *J. Phys. Chem. C*, vol. 112, no. 46, pp. 17983–17987, Nov. 2008, doi: 10.1021/jp807345h.

[72] C. J. Murphy *et al.*, “Gold Nanoparticles in Biology: Beyond Toxicity to Cellular Imaging,” *Acc. Chem. Res.*, vol. 41, no. 12, pp. 1721–1730, Dec. 2008, doi: 10.1021/ar800035u.

[73] K.-S. Lee and M. A. El-Sayed, “Gold and Silver Nanoparticles in Sensing and Imaging: Sensitivity of Plasmon Response to Size, Shape, and Metal Composition,” *J. Phys. Chem. B*, vol. 110, no. 39, pp. 19220–19225, Oct. 2006, doi: 10.1021/jp062536y.

[74] M.-C. Daniel and D. Astruc, “Gold Nanoparticles: Assembly, Supramolecular Chemistry, Quantum-Size-Related Properties, and Applications toward Biology, Catalysis, and Nanotechnology,” *Chem. Rev.*, vol. 104, no. 1, pp. 293–346, Jan. 2004, doi: 10.1021/cr030698+.

[75] S. Link and M. A. El-Sayed, “Size and temperature dependence of the plasmon absorption of colloidal gold nanoparticles,” *J. Phys. Chem. B*, vol. 103, no. 21, pp. 4212–4217, May 1999, doi: 10.1021/jp984796o.

[76] R. R. Anderson and J. A. Parrish, “The Optics of Human Skin,” *J. Invest. Dermatol.*, vol. 77, no. 1, pp. 13–19, Jul. 1981, doi: 10.1111/1523-1747.ep12479191.

[77] R. Weissleder, “A clearer vision for in vivo imaging,” *Nat. Biotechnol.*, vol. 19, no. 4, pp. 316–317, Apr. 2001, doi: 10.1038/86684.

[78] K.-S. Lee and M. A. El-Sayed, “Dependence of the Enhanced Optical Scattering Efficiency Relative to That of Absorption for Gold Metal Nanorods on Aspect Ratio, Size, End-Cap Shape, and Medium Refractive Index,” *J. Phys. Chem. B*, vol. 109, no. 43, pp. 20331–20338, Nov. 2005, doi: 10.1021/jp054385p.

[79] C. Sönnichsen *et al.*, “Drastic Reduction of Plasmon Damping in Gold Nanorods,” *Phys. Rev. Lett.*, vol. 88, no. 7, p. 077402, Jan. 2002, doi: 10.1103/PhysRevLett.88.077402.

[80] A. L. Oldenburg, M. N. Hansen, D. A. Zweifel, A. Wei, and S. A. Boppart, “Plasmon-resonant gold nanorods as low backscattering albedo contrast agents,” *Opt. Express*, vol. 14, no. 15, pp. 6724–6738, 2006.

[81] M. G. Sandrian *et al.*, “Inflammatory response to intravitreal injection of gold nanorods,” *Br. J. Ophthalmol.*, vol. 96, no. 12, pp. 1522–1529, 2012.

[82] T. S. Troutman, J. K. Barton, and M. Romanowski, “Optical coherence tomography with plasmon resonant nanorods of gold,” *Opt. Lett.*, vol. 32, no. 11, pp. 1438–1440, 2007.

[83] V.-P. Nguyen, Y. Li, J. Henry, W. Zhang, X. Wang, and Y. M. Paulus, “Gold nanorod enhanced photoacoustic microscopy and optical coherence tomography of choroidal neovascularization,” *ACS Appl. Mater. Interfaces*, vol. 13, no. 34, pp. 40214–40228, 2021.

[84] Y. P. De León, J. L. Pichardo-Molina, N. A. Ochoa, and D. Luna-Moreno, “Contrast enhancement of optical coherence tomography images using branched gold nanoparticles,” *J. Nanomater.*, vol. 2012, pp. 128–128, 2012.

[85] C. S. Kim, D. Ingato, P. Wilder-Smith, Z. Chen, and Y. J. Kwon, “Stimuli-disassembling gold nanoclusters for diagnosis of early stage oral cancer by optical coherence tomography,” *Nano Converg.*, vol. 5, no. 1, pp. 1–11, 2018.

[86] E. V. Zagaynova *et al.*, “Contrasting properties of gold nanoparticles for optical coherence tomography: phantom, in vivo studies and Monte Carlo simulation,” *Phys. Med. Biol.*, vol. 53, no. 18, p. 4995, 2008.

[87] J. Chen *et al.*, “Gold nanocages: bioconjugation and their potential use as optical imaging contrast agents,” *Nano Lett.*, vol. 5, no. 3, pp. 473–477, 2005.

[88] P. Keahey *et al.*, “Spectral-and polarization-dependent scattering of gold nanobipyramids for exogenous contrast in optical coherence tomography,” *Nano Lett.*, vol. 21, no. 20, pp. 8595–8601, 2021.

[89] B. C. Rostro-Kohanloo *et al.*, "The stabilization and targeting of surfactant-synthesized gold nanorods," *Nanotechnology*, vol. 20, no. 43, p. 434005, Oct. 2009, doi: 10.1088/0957-4484/20/43/434005.

[90] K. A. Kozek, K. M. Kozek, W. C. Wu, S. R. Mishra, and J. B. Tracy, "Large-scale synthesis of gold nanorods through continuous secondary growth," *Chem. Mater.*, vol. 25, no. 22, pp. 4537–4544, Nov. 2013, doi: 10.1021/cm402277y.

[91] H. Matsui *et al.*, "A physical linkage between cystic fibrosis airway surface dehydration and Pseudomonas aeruginosa biofilms CELL BIOLOGY," 2006. [Online]. Available: www.pnas.orgcgidoi10.1073pnas.0606428103

[92] L. H. Cai, S. Panyukov, and M. Rubinstein, "Mobility of nonsticky nanoparticles in polymer liquids," *Macromolecules*, vol. 44, no. 19, pp. 7853–7863, Oct. 2011, doi: 10.1021/ma201583q.

[93] S. Alam and A. Mukhopadhyay, "Translational Anisotropy and Rotational Diffusion of Gold Nanorods in Colloidal Sphere Solutions," *Langmuir*, vol. 31, no. 32, pp. 8780–8785, Jul. 2015, doi: 10.1021/acs.langmuir.5b01682.

[94] S. M. Kreda *et al.*, "Coordinated release of nucleotides and mucin from human airway epithelial Calu-3 cells," *J. Physiol.*, vol. 584, no. 1, pp. 245–259, Oct. 2007, doi: 10.1113/jphysiol.2007.139840.

[95] S. M. Kreda *et al.*, "Characterization of Wild-Type and F508 Cystic Fibrosis Transmembrane Regulator in Human Respiratory Epithelia," *Mol. Biol. Cell*, vol. 16, pp. 2154–2167, 2005, doi: 10.1091/mbc.E04.

[96] B. C. Tang *et al.*, "Biodegradable polymer nanoparticles that rapidly penetrate the human mucus barrier," *Proc. Natl. Acad. Sci.*, vol. 106, no. 46, pp. 19268–19273, Nov. 2009, doi: 10.1073/pnas.0905998106.

[97] D. L. Marks, R. L. Blackmon, and A. L. Oldenburg, "Diffusion tensor optical coherence tomography," *Phys. Med. Biol.*, vol. 63, no. 2, Jan. 2018, doi: 10.1088/1361-6560/aa9cfe.

[98] P. J. Basser, J. Mattiello, and D. LeBihan, "MR diffusion tensor spectroscopy and imaging," *Biophys. J.*, vol. 66, no. 1, pp. 259–267, Jan. 1994, doi: 10.1016/S0006-3495(94)80775-1.

[99] D. Le Bihan *et al.*, "Diffusion tensor imaging: Concepts and applications," *J. Magn. Reson. Imaging*, vol. 13, no. 4, pp. 534–546, Apr. 2001, doi: 10.1002/jmri.1076.

[100] E. R. Melhem, S. Mori, G. Mukundan, M. A. Kraut, M. G. Pomper, and P. C. M. Van Zijl, “Diffusion Tensor MR Imaging of the Brain and White Matter Tractography,” *Am. J. Roentgenol.*, vol. 178, no. 1, pp. 3–16, Jan. 2002, doi: 10.2214/ajr.178.1.1780003.

[101] P. Mukherjee, J. I. Berman, S. W. Chung, C. P. Hess, and R. G. Henry, “Diffusion Tensor MR Imaging and Fiber Tractography: Theoretic Underpinnings,” *Am. J. Neuroradiol.*, vol. 29, no. 4, pp. 632–641, Apr. 2008, doi: 10.3174/ajnr.A1051.

[102] S. Mori and J. Zhang, “Principles of Diffusion Tensor Imaging and Its Applications to Basic Neuroscience Research,” *Neuron*, vol. 51, no. 5, pp. 527–539, Sep. 2006, doi: 10.1016/j.neuron.2006.08.012.

[103] C. Rieu *et al.*, “Topotactic Fibrillogenesis of Freeze-Cast Microridged Collagen Scaffolds for 3D Cell Culture,” *ACS Appl. Mater. Interfaces*, vol. 11, no. 16, pp. 14672–14683, Apr. 2019, doi: 10.1021/acsami.9b03219.

[104] M. Antman-Passig and O. Shefi, “Remote Magnetic Orientation of 3D Collagen Hydrogels for Directed Neuronal Regeneration,” *Nano Lett.*, vol. 16, no. 4, pp. 2567–2573, Apr. 2016, doi: 10.1021/acs.nanolett.6b00131.

[105] C. Guo and L. J. Kaufman, “Flow and magnetic field induced collagen alignment,” *Biomaterials*, vol. 28, no. 6, pp. 1105–1114, Feb. 2007, doi: 10.1016/j.biomaterials.2006.10.010.

[106] S. Eom *et al.*, “Hydrogel-Assisted Electrospinning for Fabrication of a 3D Complex Tailored Nanofiber Macrostructure,” *ACS Appl. Mater. Interfaces*, vol. 12, no. 46, pp. 51212–51224, Nov. 2020, doi: 10.1021/acsami.0c14438.

[107] A. Rezaei, A. Nasirpour, and M. Fathi, “Application of Cellulosic Nanofibers in Food Science Using Electrospinning and Its Potential Risk: Application of cellulosic nanofibers…,” *Compr. Rev. Food Sci. Food Saf.*, vol. 14, no. 3, pp. 269–284, May 2015, doi: 10.1111/1541-4337.12128.

[108] P. Lee, R. Lin, J. Moon, and L. P. Lee, “Microfluidic alignment of collagen fibers for in vitro cell culture,” *Biomed. Microdevices*, vol. 8, no. 1, pp. 35–41, Mar. 2006, doi: 10.1007/s10544-006-6380-z.

[109] D. Vader, A. Kabla, D. Weitz, and L. Mahadevan, “Strain-Induced Alignment in Collagen Gels,” *PLoS ONE*, vol. 4, no. 6, p. e5902, Jun. 2009, doi: 10.1371/journal.pone.0005902.

[110] E. East, D. B. De Oliveira, J. P. Golding, and J. B. Phillips, “Alignment of Astrocytes Increases Neuronal Growth in Three-Dimensional Collagen Gels and Is Maintained Following Plastic

Compression to Form a Spinal Cord Repair Conduit," *Tissue Eng. Part A*, vol. 16, no. 10, pp. 3173–3184, Oct. 2010, doi: 10.1089/ten.tea.2010.0017.

[111] C. P. Ng, B. Hinz, and M. A. Swartz, "Interstitial fluid flow induces myofibroblast differentiation and collagen alignment in vitro," *J. Cell Sci.*, vol. 118, no. 20, pp. 4731–4739, Oct. 2005, doi: 10.1242/jcs.02605.

[112] A. D. Nocera, R. Comín, N. A. Salvatierra, and M. P. Cid, "Development of 3D printed fibrillar collagen scaffold for tissue engineering," *Biomed. Microdevices*, vol. 20, no. 2, p. 26, Jun. 2018, doi: 10.1007/s10544-018-0270-z.